CHRISTIAN-ALBRECHTS UNIVERSITY OF KIEL

DOCTORAL DISSERTATION

Hierarchical Multiscale Evaluation of Bone Adaptation around Magnesium-based Implants

Author:

Sandra SEFA

from

Accra-Ghana

Submitted in Kiel on October 26, 2023.

A thesis submitted in fulfilment of the requirements for the degree of Doktor-Ingenieur

(Dr.-Ing.)

at the

Christian-Albrechts University of Kiel, Faculty of Engineering

(Institute of Metallic Biomaterials, Helmholtz-Zentrum Hereon)

Supervisor:

Prof.Dr. Regine Willumeit-Römer

Reviewer:

Prof. Dr. Jan-Bernd HÖVENER

Date of oral examination:

March 22, 2024.

Acknowledgements

I am most grateful to God Almighty for his abundant grace, immeasurable love and favour. I would like to express my sincere gratitude and appreciation to my revered supervisor Prof. Dr. Regine Willumeit-Römer who provided the platform, technical knowledge and support. This endeavor would not have been made possible without the opportunity and her expertise.

Next, I am extremely grateful to my co-supevisors; Dr. Berit Zeller-Plumhoff and Dr. Florian Wieland for their support, guidance, invaluable patience and feedback. They have been key players every step of the way. I am grateful to the entire MBS team for the harmonous team spirit and support. I am also thankful to Dr. Berengere Luthringer-Feyerabend for her support and guidance. I extend my deepest gratitude to Dr. Oluyemi Toyinbo for his unending encouragement, constructive criticisms and his constant support in shaping my research skills.

I am grateful to my family and friends for their invaluable motivation throughout this journey especially: Mr. and Mrs. Woode, Mr. Christian Amoako, Dr. Aliu Mahama, Dr. Joseph Amoako, Mr. Wilson Okyere, Dr. Prince Bawuah, Dr. Prosper Evadzi, Miss Bavya Chathoth, Mr. Godwin Krampa and Miss Adeline Shamo.

Abstract

Despite the presence of biodegradable Magnesium (Mg) implants in clinical settings, their widespread utilization remains limited. There are some persisting unresolved inquiries regarding their biological interactions. To comprehend the effects of Mg-based implants degradation on various organizational levels of bone structure, a scale bridging analysis was conducted in this thesis. The investigation provides the first comprehensive understanding of how degrading Mg-based materials impact the bone structure, ranging from the tissue level to the intricate lacuna-canaliculi network (LCN). This comprehensive approach was undertaken with the primary objective of quantifying the formed bone and characterizing its microarchitecture, thereby ensuring a thorough assessment of its quality. By doing so, the research aims to significantly deepen the understanding of the osseointegration process concerning Mg-based alloys. It is hypothesized that the long-term osseointegration of Mg-based implants impacts the bone macrostructure, leading to enhanced bone-implant integration. Additionally, the presence of Mg degradation products should influence the functional and structural adaptation in the bone microarchitecture which will impact bone remodeling and turnover.

In the initial phase of the study, crucial tissue level information was obtained by studying different biodegradable Mg-based screws (Mg-10Gd, Mg-4Y-3RE and Mg-2Ag) which were implanted into rabbit femur for 6 and 9 months. The bone implant contact, bone volume fraction and implant morphology were studied using high-resolution synchrotron radiation micro-computed tomography and histology. In addition, the elemental traces of the degradation products were characterized using micro X-ray fluorescence. Subsequently, at the microscale, the LCN architecture was studied in detail within the interfacial bone of Mg-10Gd implanted in rat tibia in comparison to Titanium (Ti) at 4, 8, 10, 12 and 20 weeks using synchrotron radiation-based transmission X-ray microscopy in conjunction with image-based finite element modelling. The ability to scrutinize the bone microstructure at this level of detail enables the discernment of the LCN adaptation in order to unlock valuable information about the healing process, bone remodeling, and material-tissue interactions specific to Mg-10Gd implant degradation.

According to the tissue level analysis, it was observed that mature bone formation occurred around all types of implants. Moreover, the elements Calcium (Ca) and Phosphorus (P), which are integral components of bone structure were distributed within the degradation layer of all implant types. The elemental analysis further showed that the implants containing Yttrium (Y) and Gadolinium (Gd) remained intact after 9 months, whereas those containing Silver (Ag) had severely disintegrated. In the micro-nanoscale domain, the degradation of Mg-10Gd did not significantly impact on the morphology of the LCN and its fluid flow dynamics. However, there was a significant decrease in lacunar density compared to Ti during the 4 to 12-week period. Through the combination of data from both macro and micro scales, it became evident that despite the distinct degradation dynamics of Mg-10Gd, Mg-4Y-3RE, and Mg-2Ag, they elicited comparable long-term bone healing responses. The presence of Gd and Y elements for an extended period did not disrupt bone formation, suggesting their non-harmful nature. Additionally, the degradation of Mg-10Gd had a greater influence on lacunar distribution rather than morphology, indicating potential variations in bone remodeling rate when compared to Ti.

Zusammenfassung

Obwohl biologisch abbaubare Magnesium (Mg)-Implantate in der Praxis eingesetzt werden, ist ihre breite Anwendung nach wie vor begrenzt, da es immer noch ungelöste Fragen zu den biologischen Wechselwirkungen gibt. Um die Auswirkungen des Abbaus von Mg-Implantaten auf die verschiedenen hierarchischen Ebenen der Knochenstruktur zu verstehen, wurde eine längenskalenübergreifende Analyse durchgeführt. Diese Untersuchung liefert das erste Verständnis darüber, wie sich der Abbau von Mg-basierten Materialien auf die Knochenstruktur auswirkt, angefangen von der Gewebeebene bis hin zu dem komplizierten Lakuna-Kanalikuli-Netzwerk (LCN). Dieser Ansatz wurde mit dem Ziel verfolgt, den gebildeten Knochen zu quantifizieren und seine Mikroarchitektur zu charakterisieren, um so eine Einschätzung seiner Qualität machen zu können. So kann das Verständnis des Osseointegrationsprozesses bei Mg-Legierungen vertieft werden. Es wird angenommen, dass die langfristige Osseointegration von Mg-basierten Implantaten die Makrostruktur des Knochens beeinflusst, was zu einer verbesserten Knochen-Implantat-Integration führt. Darüber hinaus kann das Vorhandensein von Mg-Abbauprodukten die funktionelle und strukturelle Anpassung der Knochenmikroarchitektur beeinflussen, was sich auf den Knochenumbau auswirken könnte.

Im ersten Teil der Studie wurden Informationen auf der Gewebeebene durch die Untersuchung verschiedener biologisch abbaubarer Schrauben auf Mg-Basis (Mg-10Gd, Mg-4Y-3RE und Mg-2Ag) gewonnen, die 6 und 9 Monate lang in Kaninchenoberschenkelknochen implantiert waren. Der Knochenimplantatkontakt, der Knochenvolumenanteil und die Implantatmorphologie wurden mittels hochauflösender Synchrotronstrahlungs-Mikro-Computertomographie und Histologie untersucht. Die Elementzusammensetzung der Abbauprodukte wurde mittels Mikro-Röntgenfluoreszenz charakterisiert. Im zweiten Teil der Arbeit wurde die LCN-Architektur in Knochenbereichen nahe der Implantatgrenzfläche mittels Synchrotronstrahlungs-Transmissions-Röntgenmikroskopie in Verbindung mit bildbasierter Finite-Elemente-Modellierung untersucht. Es wurden Knochenproben aus der Tibia von Ratten in die Implantate aus Mg-10Gd und Titan eingesetzt waren, verwendet. Die hierbei untersuchten Heilungszeiträume waren 4, 8, 10, 12 und 20 Wochen. Die Mikrostruktur des Knochens auf hoher Detailstufe zu untersuchen, ermöglicht die Einsicht in die LCN-Anpassung und erlaubt wertvolle Informationen über den Heilungsprozess, den Knochenumbau und die Material-Gewebe-Wechselwirkungen abzuleiten, die für die Degradation von Mg-10Gd-Implantaten spezifisch sind.

Die Analyse auf Gewebeebene ergab, dass um alle Implantattypen eine reife Knochenstruktur zu beobachten war. Die Elemente Calcium (Ca) und Phosphor, die Bestandteile der Knochenstruktur sind, waren innerhalb der Degradationsschichten aller Implantanttypen verteilt. Die Elementanalyse zeigte, dass die Implantate, die Yttrium (Y) und Gadolinium (Gd) enthielten, nach 9 Monaten noch intakt waren, während die Magnesiumlegierungen mit Silber (Ag) stark abgebaut war. Im mikro-nanoskaligen Bereich hatte der Abbau von Mg-10Gd keinen signifikanten Einfluss auf die Morphologie des LCN und die Dynamik der Flüssigkeitsströmung. Allerdings kam es zu einer signifikanten Abnahme der Lakunendichte im Vergleich zu Ti während des Zeitraums von 4 bis 12 Wochen. Durch die Kombination von Daten aus dem Makro- und Mikrobereich wurde deutlich, dass trotz der unterschiedlichen Degradationsdynamik von Mg-10Gd, Mg-4Y-3RE und Mg-2Ag vergleichbare langfristige Knochenheilungsreaktionen stattgefunden haben. Die Anwesenheit der Elemente Gd- und Y über einen längeren Zeitraum störte die Knochenbildung nicht, was darauf hindeutet, dass sie nicht schädlich sind. Darüber hinaus hatte der Abbau von Mg-10Gd einen größeren Einfluss auf die Verteilung der Lacunae als auf die Morphologie, was auf potenzielle Unterschiede in der Knochenumbaugeschwindigkeit im Vergleich zu Ti hinweist.

“An intelligent heart acquires knowledge, and the ear of the wise seeks knowledge”

Proverbs 18:15

Contents

List of Abbreviations

BIC	Bone Implant Contact
BA	Bone Area
BV	Bone Volume
BV/TV	Bone Volume to Total Volume
Ca	Canalicular
Ca.Nodes/BV	Canaliculi Junction Density
Ca.SA	Canaliculi Surface Area
Ca.V	Canaliculi Volume
CCD	Charged Couple Device
ECM	Extra Cellular Matrix
FIB	Focused Ion Beam
Gd	Gadolinium
HAP	Hydroxyapatite
Lc	Lacunar
N.Ca/LV.SA	Canaliculi Areal Density
N.Lc/BV	Lacunar Number Density
N.Vs/BA	Vascular Number Density
V.Vs/BV	Vascular Volume Density
LCN	Lacuno-canaliculi Network
LCN/BV	LCN porosity
L.SA	Lacunar Surface Area
Lc.V	Lacunar Volume
Mg	Magnesium
PMMA	PolyMethylMethAcrylat
RE	Rare earth
ROI	Region of Interest
SEM	Scanning Electron Microscope
SRµCT	Synchrotron Radiation micro-computed Tomography
SRnCT	Synchrotron Radiation nano-computed Tomography
TXM	Transmission X-ray Microscopy
VOI	Volume of Interest

Chapter 1

Motivation, objectives and aims

With an ageing society, the prevalence of orthopaedic diseases which require the use of biodegradable implants to support bone healing is increasingly likely. In certain temporary orthopaedic interventions, such as fracture repair, the use of biodegradable implants is more advantageous because patients would need no implant removal once the bone is healed. Biodegradable implants are supposed to possess the following essential requirements prior to clinical application: 1) controlled and adequate degradation profile, 2) temporal and spatial stability, 3) degradation products should be biocompatible, 4) stimulates bone regeneration, bone healing and support and assist anti-inflammatory mechanisms, and 5) complete replacement by the host tissue after degradation[1]. In this regard, Mg-based implants have been shown to be good candidates[2–4] because they are biocompatible, meaning that they are not toxic or carcinogenic. Furthermore, Mg has a elastic modulus (~ 45 GPa)[5] closer to bone (3-20 GPa)[6] than currently used standard implants such as Ti (120 GPa)[7] and steel (180-200 GPa)[8]. This implies that Mg-based implants are suitable to avoid stress shielding (adaptive changes bone strength and stiffness around metallic implants) which could lead to reduced bone density[6,9,10]. Also, Mg-based implants are biodegradable due to the dissolution of Mg with subsequent replacement of the host tissue thereby sparing patients additional costs and pain by averting secondary surgeries[5]. Another attractive property of Mg is it's lightweight. Mg is approximately 40 % as dense as Ti-based alloys and 20 % as dense as stainless steel and cobalt-chrome alloys making them an optimum choice for light-weight surgical implants[5].

As noted earlier, one advantage of Mg is its degradability, but the degradation rate has to be adjusted in accordance to the application. In pursuit of this aim, either ultrahigh-purity Mg is utilized or Mg is doped with other elements to improve its mechanical properties and with the appropriate treatment and processing the degradation could also be tailored. In this regard, several Mg alloy systems have been developed with several favorable properties compared to pure Mg. In this thesis, two binary Mg-based alloys, namely Mg-2Ag (2 weight percent (wt. %) of Silver (Ag)) and Mg-10Gd (2 wt. % of gadolinium (Gd)), and a ternary Mg-baesd alloy, namely Mg-4Y-3RE (4 wt. % of Yttrium (Y), 2 wt. % of Neodymium (Nd), 1 wt. % of Cerium (Ce)), are considered. Aside retarding rapid degradation, the aforementioned alloyants possess unique characteristics. Ag has an anti-bacterial property[11] which could be useful in curbing implant-related infection. Gd, Y, Nd and Ce are rare earth elements (REE) which have good mechanical properties[12]. The reader is referred to chapter 2 for a detailed summary of the advantages of the aforementioned alloyants. As previously mentioned, the biodegradation of Mg-based alloys is one of its most attractive properties that is shifting the paradigm in orthopaedic research and application. At the same time, the biodegradability incites concerns about the impact and integration of the degradation products on the host bone. For this reason, the clinical use of Mg-based implants must be preceded with a series of *in vitro* and *in vivo* tests to ascertain their safety and efficacy in humans. Since the bone is hierarchically nested, it is pertinent to understand the impact of Mg degradation products on the various organizational levels (i.e. from the tissue level down to the ultrastructural level) (figure 1.1).

This thesis focuses on the macro- and micro-scale bone adaptation around Mg-based implants. The clinical success of an implanted medical device is predominantly assessed based on its anchorage in the bone and the proportion of mineralized bone formed next to it. However, the presence of mineralized tissue adjacent to bone implants after predetermined healing period is inadequate to fully comprehend its osseointegration. Additional characterization is pertinent to ascertain the quality of the formed bone in terms of health and

mechanical stability. Such characterization includes assessing the micro- and ultratructure of the bone to achieve a holistic understanding of its osseointegration. The need for a comprehensive hierarchical characterization of osseointegration is paramount for all orthopedic devices, but it becomes even more critical for degrading implants like Mg, where both surface and bulk chemistry undergo continuous changes throughout its implanted lifetime. Thus, the aim of this thesis is to first evaluate the long-term osseointegration of Mg-based implants on the bone macrostructure. Secondly, the functional and structural adaptation of the bone microarchitecture in the presence of the Mg degradation products will also be investigated. Although ultrastructure characterization is beyond the scope of this thesis, results of this studies will be compared with ultrastructure findings from other studies since the microarchitecture and ultrastructure of bone are functionally interconnected. The two aims were carried out in two different studies:

Study I: Evaluation of the long-term *in vivo* behavior of three developed Mg alloys. The specific aims are:

- To evaluate the bone formation, implant anchorage in the host bone and the evolution of the degradation products of Mg-10Gd, Mg-4Y-3RE and Mg-2Ag.
- To assess the impact of pre-incubation of Mg-10Gd, Mg-4Y-3RE and Mg-2Ag in blood on their *in vivo* behavior.

Study II: Characterization of the microstructural adaptation of bone around Mg-10Gd and Ti using multiscale X-ray imaging. The specific aims are:

- To characterize the lacunar and vascular porosity within the interfacial bone of Mg-10Gd.
- To characterize the LCN morphology of the interfacial bone of Mg-10Gd.
- To model the fluid flow within the LCN of the interfacial bone of Mg-10Gd using finite element modelling.

It is hypothesized in **Study I** that the long-term osseointegration of the three selected Mg alloys should be similar in terms of bone formation around the alloys and their anchorage to the host bone since the rapid degration Mg is expected to be mitigated by the alloyants providing suitable environment for osseointegration. The research strategy for **Study I** is to first assess the long-term osseointegration of Mg-10Gd, Mg-4Y-3RE and Mg-2Ag in a rabbit model at 6 and 9 months post-implantation using multimodal imaging technologies including high resolution synchrotron radiation micro-computed tomography (SRµCT), micro X-ray fluorescence and histomorphometry. Mg-4Y-3RE has a similar formulation to WE43 which is a part of the WE series and some of it's series is clinically approved for osseosynthesis and cardiovascular applications. Examples are Magmaris® (BIOTRONIK SE & Co. KG, Berlin, Geramny) for the treatment of coronary arteries lesions and MAGNEZIX® CS compression screws (Syntellix Ag, Hannover, Germany) for the treatment of scaphoid fractures. As explained above, the WE series are well studied and have so far shown optimum mechanical and *in vivo* performance therefore, due to the similarity in composition of Mg-4Y-3RE to WE43, the former was chosen as a reference material. By this strategy, the bone formation around the Mg-based implants, the contact of the Mg-based implants to the host bone as well as the evolution of their degradation products are investigated. A short-term *in vivo* study of Mg-10Gd, Mg-4Y-3RE and Mg-2Ag has revealed that in comparison to Mg-10Gd and Mg-4Y-3RE, Mg-2Ag yielded poor osseointegration due to inadequate contact with the host bone and fibrous tissue encapsulation at 1 and 3 months post implantation[13]. Galli *et al*. highlighted that the the accelerated degradation behaviour of Mg-2Ag critically hindered its proper osseointegration which was evident in its fast disintegrating degradation products. The presence of numerous microgalvanic couples due to the large difference in electrode potential

between Mg (-2.37 V at 25 º C) and Ag (+0.80 V at 25 ºC) was postulated as key factor in accelerating its degradation [13]. In view of this, it is necessary to re-evaluate the aforementioned alloys at longer healing times in order to understand if their short-term behavior differed from their long-term behavior in **Study I**. Long-term evaluations are particularly important because the lifetime of Mg-based alloys can be monitored *in vivo* until they are fully degraded which gives insight into their mechanical integrity upon degradation and the evolution of their degradation products. Knowledge of the aftermath of completed Mg degradation is essential for formulating Mg-based othopaedic implants for bone fractures requiring temporal fixatures. Furthermore, knowledge obtained from the influence of the various alloyants on the *in vivo* performance of the aforementioned alloy systems will be a guide in the future selection of alloying elements which can improve the osseointegration of Mg-based implants.

The hypothesis for **Study II** is that the alteration of the mechanical and chemical environment within the interfacial bone of Mg-10Gd induced by Mg degradation could alter its microarchitectural adaptation. In **Study II**, the vascular and lacunar porosities around Mg-10Gd are studied at 4, 8 and 12 weeks post-implantation using SRµCT. Then, the morphological structure of the LCN is characterized around Mg-10Gd implants at 10 and 20 weeks post-implantation using SR based transmission x-ray microscopy (TXM). Finally, to understand the impact of Mg-10Gd degradation on the functionality of the LCN, image-based finite element modelling will be employed to model the fluid flow within the LCN image data that is obtained from the TXM measurement. At the tissue level, Mg-10Gd has been shown to yield a good osteogenic response[13,14] and localization of Gd at the initial implantation site[15]. From ultrastructural analysis, differences in the hydroxyapatite platelet (HAP) crystal size and lattice spacing with possible deposition of Mg in the bone matrix has been reported for Mg-10Gd in a comparative study involving Ti[16]. To date, the impact of Mg degradation on the microarchitecture of bone remains scarce. Only one pilot study has reported that differences in the degradation rate of Mg-based implants may yield differences in LCN organization[17]. Therefore, the significance of **Study II** is to bridge the information gap between ultrastructure information and tissue level information to enhance understanding the impact of Mg degradation on the various hierarchical architectures of bone.

The essence of the proposed strategy is to combine information from the macroscale (tissue level) down to the microscale (microstructural level) to expedite an in-depth understanding of Mg degradation on bone healing. Moreover, as the tissue level response of bone is impacted by its microstructural adaptation during peri-implant bone healing, understanding the microstructural adaptation might explain certain tissue level indices such as BV/TV and BIC. The findings of **Study I**[18] is published in Frontiers in Biomaterials Science while that of **Study II**[19] is published in Bioactive Materials.

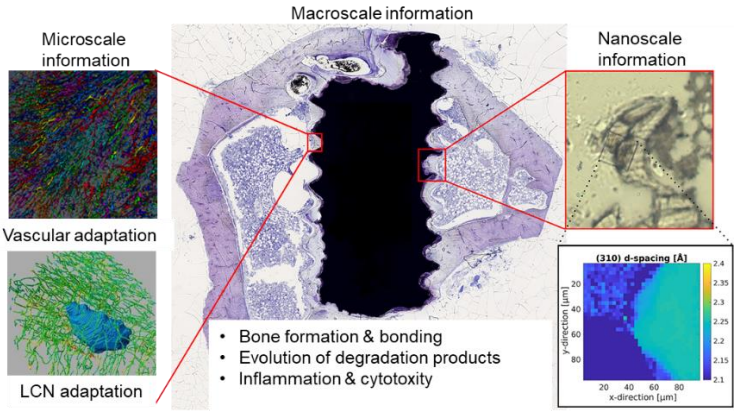

Figure 1.1: Information obtained at the various hierarchical *in vivo* investigations of Mg alloys. Adapted from Zeller-Plumhoff *et al*.[16]. Published under the Creative Commons CC-BY 4.0 Licence.

Chapter 2

State of the art

2.1 Bone

2.1.1 The gross anatomy and histology of bone

Bone is a hard, dynamic, and vascularized tissue and most of its functions depend on its loading-bearing properties. Long bones have two major regions namely the diaphysis and the epiphysis separated by the metaphysis. The diaphysis is a hollow tubular shaft between the proximal and distal ends of the bone and contains the medullary cavity within which yellow bone marrow is found. The exterior of the diaphysis is made of hard compact bone called cortical bone (figure 2.1). Metaphysis relays loads from weight-bearing joints to the diaphysis. The epiphyses are the wider regions at each end of the bone and are internally made of cancellous or trabecular bone and filled with red bone marrow. The demarcation between the epiphysis and the metaphysis is the epiphyseal plate (in children) or epiphyseal line (in adults). The outer regions of the bone are covered by a double-layered structure called periosteum while the inner region of the bone is lined with a layer of bone cells called endosteum. The periosteum contains blood vessels, nerves and lymphatic vessels that nutrify the cortical bone whereas the endosteum contains bone cells that grow and remodel the bone throughout its existence. The ends of the bone are covered with articular cartilage to absorb shock and minimize friction at bone joints.[20] As previously stated, bone tissue is either cortical or trabecular with each tissue type having a distinct organization and function. The dense nature of compact bone enables it to withstand compressive forces whereas the lightweight characteristic of spongy bone accelerates remodelling to accommodate the changing needs of the body[21]. Within compact bone are highly organized concentric osteons made of collagen and a calcified matrix called lamellae (figure 2.1). Within the centre of the osteons are the Harversian canals, which contain blood vessels, nerves and lymphatic vessels responsible for nourishing the bone. Perpendicular to the Harversian canals are the Volkmann's canals within which branching blood vessels, lymphatic vessels and nerves extend to the periosteum and endosteum. The Harversian canals and the Volkmann's canals form the vascular porosities.

Bone contains fewer cells and a large proportion of extracellular matrix (ECM)[21]. The extracellular matrix contains 33.33 % collagen (organic component) and 66.66 % hydroxyapatite (inorganic component)[22]. The collagen constituent gives bone its elastic nature and serves as a scaffold for bone cells whereas the hydroxyapatite constituent gives the bone its hardness and strength[21]. The cellular components of the bone are osteoprogenitor cells, osteoblasts, osteoclasts and osteocytes (figure 2.1) and constitute less than 2 % of the bone mass[21]. Osteogenic cells are cells that have mitotic abilities and differentiate into osteoblasts. They are located in the endosteum and the cellular layer of the periosteum (figure 2.1). Likewise, osteoblasts are also found in the endosteum and the cellular layer of the periosteum but do not possess mitotic capabilities rather, they are bone forming cells responsible for the synthesis and secretion of the collagen matrix and proteins (figure 2.1). Osteoclasts are bone-resorbing cells that originate from monocytes and macrophages[21] (figure 2.1). The shape of the bone is maintained through a balance between osteoclasts and osteoblasts activities[21]. The most abundant bone cells in the mature bone are the osteocytes which are responsible for maintaining bone health and modulating its remodeling[23]. Osteocytes are formed when the matrix surrounding the osteoblasts calcifies and becomes entombed, thereby differentiating (changing the structure of the osteoblasts) within the matrix to become osteocytes. The osteocytes and their cell processes are located within cavities called lacunae and the canaliculi

respectively, with the canaliculi connecting different lacunae. Together, they form the lacunar-canaliculi network (LCN). Often, the LCN is studied as a proxy for osteocytes and their cell processes respectively because they are difficult to access within the bone matrix.

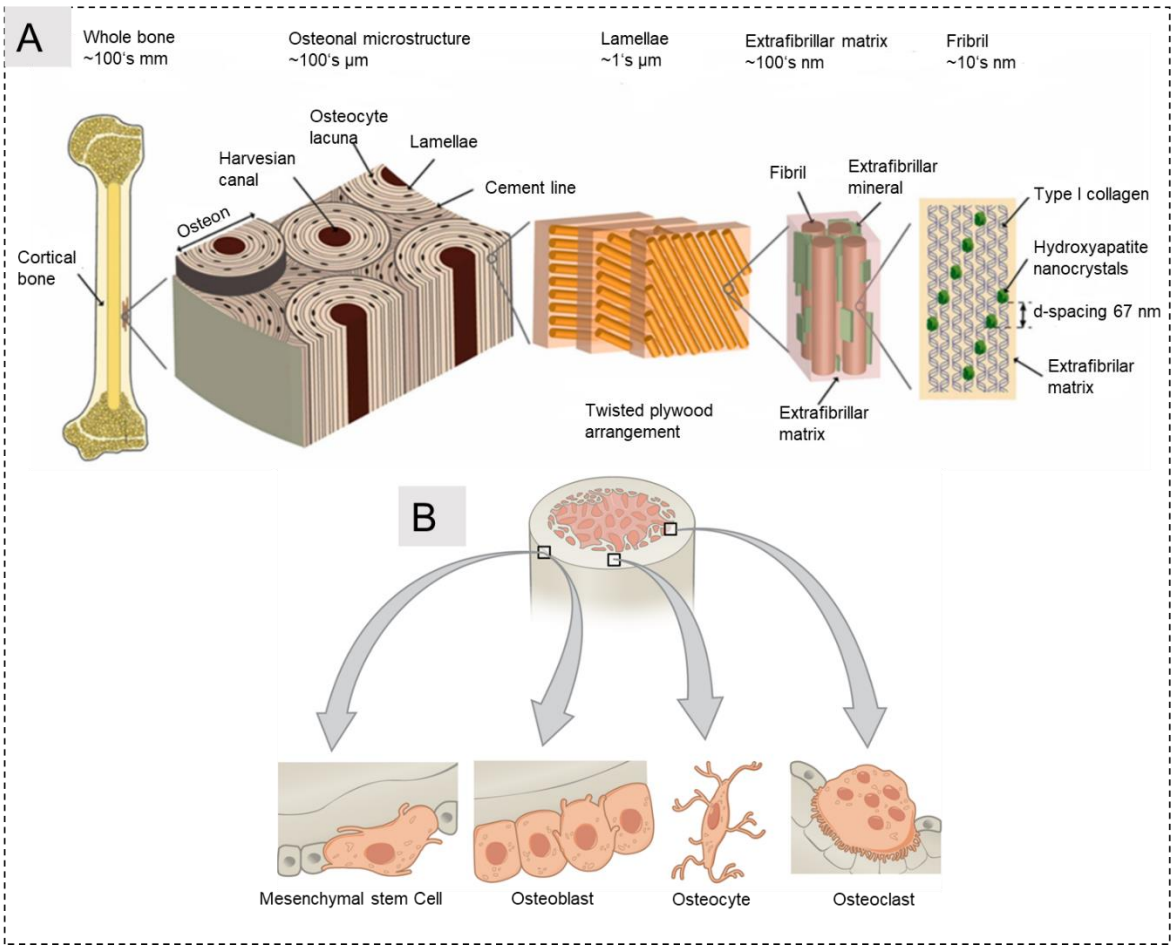

Figure 2.1: Schematic diagram of the hierarchical structure of a long bone and bone cells. Adapted from Zimmermann *et al.* [24] and Biga *et al.* [21]. Published under the Creative Commons CC-BY 4.0 Licence.

2.1.2 Bone porosities and interstitial fluid flow

Bone has hierarchically nested porosities across three dimensions. The largest is the vascular porosity followed by the LCN which are the intermediate pore spaces made up of the lacunar and canaliculi porosities. The smallest sized pores are the collagen-apatite porosity which is associated with the spaces between the collagen and the crystallites of the hydroxyapatite[25]. The fluid within the collagen-apatite porosity is attached to the hydroxyapatite[26] thus it does not significantly contribute to mechanotransduction within bone[27]. Vascular porosity ranges from 4 to 16 % in humans[23] and from 1 to 5 % in mice[25]. The LCN porosity (LCN volume/total bone volume) is reported to vary between 1.5 % -14 % in rat femur and tibia[28,29]. Other LCN microarchitectural parameters that are usually quantified are the lacunar number density, lacunar volume density, lacunar shape, lacunar surface area, volume, length and width. Several researchers have reported lacunar number density ranging from 26 x 10^3 to 90 x 10^3 lacunae per cubic millimeter[28–31]. The osteocyte lacunar volume ranges between 290-500 cubic micrometer[28–32], in length between 9-29 µm[30,33–35] and in width between 2-8 µm[33–35]. Usually, parameters that are quantified for canaliculi are the number of canaliculi per unit surface area, canaliculi branching, canaliculi diameter, surface area and volume. Canaliculi

number per unit area have been reported to vary between 0.5 to 0.9 canaliculi per square micrometer[35,36]. The average canaliculi diameter ranges between 100 -700 nm[28,35–37].

The health of bone tissue majorly depends on effective transport of solutes and fluid between the blood supply and the bone cells, therefore, changes in the bone porosity are indicative of altered metabolism and mechanical integrity[38]. Vascular and LCN porosities constitute the bone pathways within which fluid flows. The fluid within bone is either blood or interstitial fluid, within both fluid systems continuous metabolic exchange occurs. Metabolic exchange between vascular porosity and LCN occurs within capillaries when arterial blood which is rich in oxygen and nutrient, passes through the capillary bed and deposits nutrients in the interstitial fluid and then departs with cellular waste and carbon dioxide[25]. The nutrient-rich interstitial fluid then nourishes the cells. Apart from nutrient transport, the movement of interstitial fluid within the osteocyte LCN is known to elicit mechanotransduction[25]. Several evidences suggest that both mechanotransduction and metabolic exchanges are substantially enhanced by mechanical loading[25,39,40]. The vascular porosities and the osteocyte LCN are hypothesized to form a hydraulic network which is optimized to effectively transport fluid and solute between the blood supply and the cells[41]. The vascular porosity and the osteocyte LCN differ in size by several orders of magnitude which implicates differences in fluid pressures within the two pore systems. The vascular porosities have relatively large pore sizes which relax the fluid pressure faster (10^{-6} s) thus it is considered a low-pressure domain. In contrast, the relatively small pore sizes of the LCN relaxes the fluid pressure rather slowly (10^{-3} s). Therefore, the vascular porosities relax the fluid pressure within the LCN to ensure efficient metabolic exchange[25].

2.1.3 Progression of peri-implant bone healing

In peri-implant bone healing, there is either distant or contact osteogenesis. In distant osteogenesis, osteoblasts deposit new bone on old bone surfaces within the peri-implant site and move towards the implant surface[42]. It has been shown that distant osteogenesis is likely to occur in cortical bone due to its slow remodeling rate[43]. In contrast, contact osteogenesis involves the deposition of new bone directly on the implant surface. Both types of osteogenesis occur in every bone healing site and directly affect the structure and composition of the bone at the bone implant interface[44]. Preparation of the implantation site causes osteocyte apoptosis due to thermal necrosis and/or manipulation of the implantation site and is known to extend to a depth of 100-500 µm from the implantation site[45,46].

The clinical success of bone implant relies on successful osseointegration which in turn depends on a cascade of biological reactions at four distinct phases. The phases are osteoconduction, callus formation, callus ossification (modelling) and bone remodeling which form the hallmark of bone healing and bone regeneration[42]. The first and most important stage is osteoconduction which involves the recruitment and migration of osteogenic cells to the healing site[47]. The migration of progenitor cells is initiated when surgical sites are prepared thus causing bleeding and subsequently hematoma. Hematoma provides the mechanical and biochemical components needed for osteoconduction. Once the implant surface contacts the blood, protein adsorption, platelet activation, blood clot formation and inflammation occur; a process which is influenced by implant surface chemistry and topography as well as initial stability of the implant[45]. After successful osteoconduction, the next phase is the formation of woven bone which begins by the differentiation of osteogenic cells (mesenchymal cells) into osteoblasts followed by the secretion of the bone matrix[45]. Osteoconduction and the bone formation have shown to occur as early as within 24 h during peri-implant healing in a porcine model[48]. The bone formed is subsequently mineralized and envelopes the osteoblasts, which differentiates into osteocytes. Bone modelling results in the formation of immature woven bone

with different properties from native lamellar bone[49] and is continuously remodeled throughout the lifetime of the host bone. Woven bone bridges the gap between the implant and the host bone thus, it stabilizes the implant within the host bone which results in bone bonding depending on the surface topology of the implant[44]. Remodeling could also be triggered by changes in mechanical stresses and microdamage to the host bone which occur as far as 2 mm[50] from the implantation site.

Figure 2.2: Timeline of bone peri-implant bone healing

As previously mentioned, osteocytes are the most abundant bone cells whose functions include mechanosensation, bio-transport, regulation of mineral homeostasis within the bone and bone remodelling[23,51,52]. As orchestrators of bone remodeling, osteocytes sense mechanical loads as mechanical signals and transduce them into chemical signals which modulate the recruitment and activities of osteocytes and osteoclasts resulting in bone mass and structure adaptation[53]. The mechanism of mechanosensation majorly includes changes in the bone strain, hydrostatic or streaming potentials which results in cell deformation or shear stress on the osteocyte cell process and body[53]. It has been estimated that interstitial fluid retains about 12 % of the applied mechanical load and generates pressures between 2-3 MPa[54] or even up to 5 MPa *in vivo*[55]. Klein-Nulend *et al*. have demonstrated that osteocytes are more sensitive to fluid shear stress than hydrostatic stress[56].

The death of osteocytes during implant site preparation results in an alteration in bone mechanosensation which triggers extensive remodeling to maintain bone structure and homeostasis[49]. The regeneration of the bone with its associated osteocytes' morphometric adaptation reveals information regarding the state of the peri-implant bone in response to the biomaterial. Within a peri-implant bone, osteocytes directly communicate with the surfaces of implants through their canaliculi by responding to mechanical stresses which consequently results in the alteration of their numbers and morphology[57,58]. The direct attachment of osteocytes' cell processes to the surface of bone implants is known to actively influence osseointegration by facilitating strong bone-implant interlocking[49]. Furthermore, newly formed peri-implant tissue has been shown to be compositionally less mature and possesses higher osteocyte density compared to native lamellar bone in Ti6Al4V (90 wt.% Ti, 6 wt.% Al, 4 wt.% V) implants[59]. In terms of morphology, the osteocytes in peri-implant bone are usually less elliptical[58,59] and slightly larger[59] than those of native lamellar bone.

2.2 The importance of Mg in the body

Magnesium (Mg) naturally occurs in the human body and has several physiological functions. As the second and fourth most abundant mineral in cellular compartments and the body respectively[60], Mg functions as a cofactor in more than 300 enzymatic reactions and is also crucial for DNA, RNA, and protein synthesis as well as reproduction[61]. Furthermore, Mg is involved in muscular contraction, neuromuscular conduction, bone metabolism by calcium absorption, osteoblast adhesion and bone formation[61–63]. The body contains between 21 – 28 g of Mg with the greater percentage (65 %) distributed in the skeleton, 34 % in intracellular compartments, and 1 % in fluids / blood[60,64–66]. The homeostasis of Mg is crucial for the

treatment and prevention of diseases[60], therefore the introduction of additional Mg as a biomaterial into the body requires careful consideration.

2.3 Mg as a biomaterial

2.3.1 Mg-based implants in musculoskeletal applications

The use of Mg as a biomaterial was first recorded in 1878 when the physician Edward C. Huse used Mg wires as ligatures to stop the bleeding of blood vessels of human patients[67]. Soon afterwards, physician Edward Payr reported extensively on the versatile use of Mg in several clinical applications[68] stimulating other clinicians to apply Mg in various surgical areas which broadened the application spectrum of Mg. The versatile use of Mg included connectors for vessel anastomosis[68–70] wires for aneurysm[71] and in osteosynthesis where Mg plates and screws were used to stabilize a transdiaphyseal humerus fracture in a child[72]. Over time, the use of Mg as a biomaterial in several other application areas gained popularity.

In musculoskeletal applications, Mg-based implants are used as fixtures to support the bone allowing healing to take place or as a scaffold on which new bone can grow[5]. Mg-based bone cements rose to prominence over 20 years ago when health concerns were raised against the use of PMMA for orthopaedic applications. The issues raised against PMMA were that they were non-degradable, non-bioactive, had poor osseointegration and emitted heat which caused thermal necrosis[73]. In view of this, magnesium-phosphate[74] and magnesium oxide[75] bone cements have been promoted as good candidates to support bone healing because of their biodegradability, osteoconductivity and good adhesive properties. Mg-based bone cements have been tested potentially for maxillofacial applications and as oral implants[76] as well as tendon and ligament repair[77,78]. OsteoCrete (Bones Solutions Inc(Colleyville, Texas)) is an example of Mg-based bone cement that is already in clinical use[79]. The utilization of Mg-based scaffolds in treating bone defects *in vivo* has been promising due to their biodegradable and osteoconductive properties[80]. Witte *et al.* reported that open porous Mg-based AZ91D (90 wt.% Mg, 9 wt.% Al, 1 wt.% Zn) scaffolds yielded appropriate inflammatory host responses without significant harm to the surrounding tissues in comparison to autologous bone[81]. Furthermore, the same authors reported that the AZ91D porous scaffold yielded higher bone mass and a higher tendency of bone maturation compared to autologous bone[82]. Porous Mg scaffold systems have successfully been used to engineer cartilage[83]. The development of Mg-based implants as fixative devices to support bone healing is one of its prioritized areas of application mainly because of its optimal properties. Due to continuous scientific efforts, there is a broad spectrum of knowledge on the fixation capabilities of Mg-based implants for fractures and bone flaps[84–86]. A variety of Mg-based osteosynthesis devices such as intramedullary nail[87], interfusion cage[88], rings[89], and bone plates and screws systems[90] have been designed for different anatomical areas (figure 2.3). Mg-Y-RE-Zn with the tradename MAGNEZIX® CS compression screws (Syntellix Ag, Hannover, Germany) was the first Mg-based screws to be used for the treatment of hallux valgus after it received a CE mark in 2013[91] with equivalent clinical performance similar to titanium (Ti)[86]. Afterwards, several other anatomical areas such as maxillofacial fracture and osteotomy[92–95], humeral fracture[96,97], carpus[98,99] and knee intercondylar tibial[100], have been treated with MAGNEZIX.

2.3.2 Other applications of Mg as a biomaterial

Mg-based implants are also used in cardiovascular applications as stents to correct vascular stenosis caused by arteriosclerosis. To this end, the biodegradable property of Mg-based implants is also explored[101] to curb the risk of re-stenosis caused by permanent implants. In 2005, the first Mg-based stent successfully restored blood in the pulmonary artery of a premature baby[102]. Improved versions of Mg-based stents with drug-eluting capabilities are currently underway[103]. In nerve regeneration, Mg is used as microfilaments within hollow nerve conduits to repair peripheral nerve gas[104]. Furthermore, Mg is used as wound closure devices in the form of clips and sutures[105–108]. An example is Velox CD (Transluminal Technologies LLC, Syracuse, USA) which is already in clinical use as a closure device for arterial wounds[106].

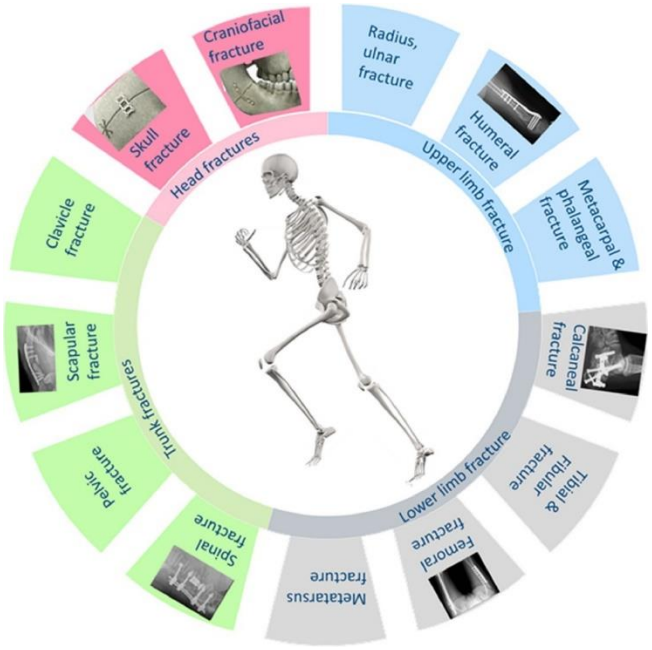

Figure 2.3 Mg-based fixative devices in different application areas. From Albaraghtheh *et al*.[109] Published under a Creative Commons CC-BY 4.0 Licence.

2.3.3 Challenges of Mg as an implant material

Amomg the benefits of biodegradable Mg as an implant material, some challenges remain. First, its relatively brittle nature makes it easily breakable[5]. The second and the most prominent challenge is the rapid degradation of pure Mg which needs to be curbed in order to maintain optimum strength to support bone healing as well as not to interfere with the healing process[5]. A high degradation rate can alter the pH value in the environment, elevate the Mg ion content and produce hydrogen gas and which could have deleterious consequences for the bone and surrounding tissues[110] such as the disruption of local bone mineralization which could alter the biomechanics of bone[111]. The degradation of Mg is an electrochemical reaction involving anodic and cathodic reactions. The most common reactions in aqueous solution are given in equations 1.1-1.3.

$$\text{Anodic reaction: } Mg \leftrightarrow Mg^{2+} + 2e^{-} \quad (1.1)$$

$$\text{Cathodic reaction: } 2H_2O + 2e^{-} \leftrightarrow 2OH^{-} + H_2 \quad (1.2)$$

$$\text{Overall reaction: } Mg + 2H_2O \leftrightarrow Mg(OH)_2 + H_2 \quad (1.3)$$

In an aqueous solution, Mg is oxidated into metal cations (Mg^{2+}) and simultaneously releases electrons (equation 1.1). In the course of the cathodic-anodic reaction water is splitted to form hydrogen (H_2) and hydroxide (OH^-) species (equation 1.2). OH^- further react with Mg^{2+} to form magnesium hydroxide ($Mg(OH)_2$) and hydrogen gas (H_2) (equation 1.3). The $Mg(OH)_2$ formed is insoluble at high pH and hence could potentially mitigate further corrosion. However, the chlorine ions present in a physiological environment combine with Mg^{2+} to form $MgCl_2$ which counters the passivating effect of $Mg(OH)_2$.

The degradation of Mg and its alloy in physiological conditions is complex due to the presence of sugars, proteins and salts[112]. In simulated body fluids, Mg-rare-earth alloys degradation has been shown to yield complex products with the general formular $(Mg,Ca)_x(PO_4)_y(CO_3)_z(OH)_l$[113] (where x, z and I are real numbers). Several other immersion tests have further shown that under cell culture conditions, $MgCO_3$ salt presipitates[114,115]. It is widely known that the degradation of Mg could be accelerated upon contact with other metals due to the formation of a galvanic couple. Some studies have reported enhanced degradation of ultra high purity Mg when in contact with Ti consequently resulting in declined mechanical strenghth *in vitro*[116] and *in vivo*[117]. The challenges with the rapid degradation of Mg can be dated back to the 1900's when Lambotte first discovered that Mg degraded rapidly with the formation of subcutaneous gas cavities in a human subject[118]. These gas cavities have also been reported in recent times[81,119]. Though the gas cavities have raised health concerns, Witte *et al*. have demonstrated that the generated H_2 gas bubbles did not have a deleterious effect on the bone and surrounding tissues[81,119]. However, it has been cautioned that the possibility of gas gangrene occurrence should not be overlooked[5]. Additionally, the rapid degradation of Mg causes a local increase in pH which might impede healing[5].

2.3.4 Proposed solutions for improving Mg as an implant material

Metallurgically, two solutions have been proposed to combat the outlined challenges of rapid degradation. The first is the purification of Mg to eradicate impurities (such as Fe, Si and Ni) which form cathodic sites in galvanic corrosion and have low solid-solibility in alpha-Mg matrix[120]. However, high purity Mg is extremely resistant to corrosion and the purification results in only a moderate improvement of the corrosion profile[121]. Furthermore, the purification of Mg does not offer flexibility in the modification of its mechanical properties closer to that of bone[13]. The second approach is the modification of the microstructure of Mg by alloying it with other materials or modifying the surface structure. The underlying mechanism is the modification of the alpha-Mg matrix potential by these alloying elements[121]. Some alloyants have successfully reduced Mg degradation either by forming stable passivating films or combining with the impurities, thereby eradicating their negative effects[122]. As Mg is chemically reactive, careful consideration must be given to the possible reaction of the alloyants with Mg, which can create intermetallic phases and segregations. These are formed when the alloyants are not in solid solution and might distribute along the grain boundaries of the Mg matrix leading to galvanic corrosion[123]. Moreover, the biocompatibility of ions released from the alloyants is of utmost importance. Considering the above factors, suitable alloying elements include but not limited to Calcium (Ca), Zinc (Zn), Manganese (Mn), Silver (Ag) and several other rare earth elements (REE) such as Yttrium (Y), Gadolinium (Gd), Cerium (Ce) and Neodymium (Nd). Various combinations of Mg with these elements have yielded a broad spectrum of Mg alloy systems with improved mechanical properties and suitable degradation rates. Alloy selection is a crucial process that requires careful consideration and rigorous testing. In this regard, some alloy systems have yielded promising results. For example, Mg-10Gd, Mg-2Ag and Mg-4Y-3RE (also known as WE43) have been in the limelight.

The mechanical properties of each Mg alloy system are distinct, depending on the type of alloyants (Figure 2.4A&B). For instance, classical Aluminum-Zinc-Manganese (AZ), Zinc-Zirconium (ZK) and Aluminum-Manganese (AM) series are known to have poor ductility and lower yield strength than Mg alloys containing REE at room temperature[124]. Much consideration is usually given to REE due to their atomic structure and properties thus when combined with Mg, they can refine grains, reduce galvanic corrosion, combine with impurity to reduce defects, form oxide-dense films and increase corrosion resistance[125,126]. Several researchers have reported that low or medium concentrations of REE weaken the adverse basal texture of Mg in Mg-REE alloy systems, thereby enhancing ductility and strength[127–132]. During Mg production, REE react with the hydrogen in molten Mg to form rare earth hydrides which have an inhibitory effect on the inflammation caused by the evolution of H_2 gas during Mg degradation[133]. Aside the mechanical and corrosion resistivity as a hallmark for Mg alloyants, antibacterial properties are also highly desirable, especially in the case where an implant-related infection occurs[11]. Such antibacterial alloying elements include but not limited to Ag, Mn and Zn. Among the antibacterial Mg alloy systems, ZX00 (0.45 wt.% of Zn, 0.45 wt.% of Ca) has been reported to facilitates the expression of macrophage polarization *in vivo* thereby improving tissue healing and immune response[134].

When the composition modification of Mg is inadequate, a surface modification can be employed to further decelerate the Mg degradation. Thus, the use of calcium phosphate coatings composed of hydroxyapatite and its chemical variants can enhance the biocompatibility[135], bioactivity[136], wear[137] resistance, bone conduction, bone induction and improved corrosion resistance of Mg alloys[138] by changing the surface chemistry. For instance, coated AZ31 alloys have been shown to have higher degradation resistance than uncoated AZ31[139]. As an alternative, the adhesion of protein unto the surfaces of Mg alloys is known to improve their performance. Adhesion of proteins unto Mg alloys can be achieved either by coating Mg alloys with proteins or by exploiting the natural protective layer formed around Mg alloys when in contact with blood. Proteins are immediately adsorbed unto Mg based implants after implantation[140] and determine the biological response of the implant by modulating cellular adhesion, spreading, migration, proliferation and differentiation[141,142]. Mg^{2+} exhibit a high affinity for bovine serum albumin because of the strong attraction between negatively charged hydroxyl ions and the Mg ions generated during degradation[143]. Proteins that are adsorbed unto Mg alloys improve cellular adhesion[144,145] as well as act as a barrier against a physiological environment that protects against rapid corrosion[146].

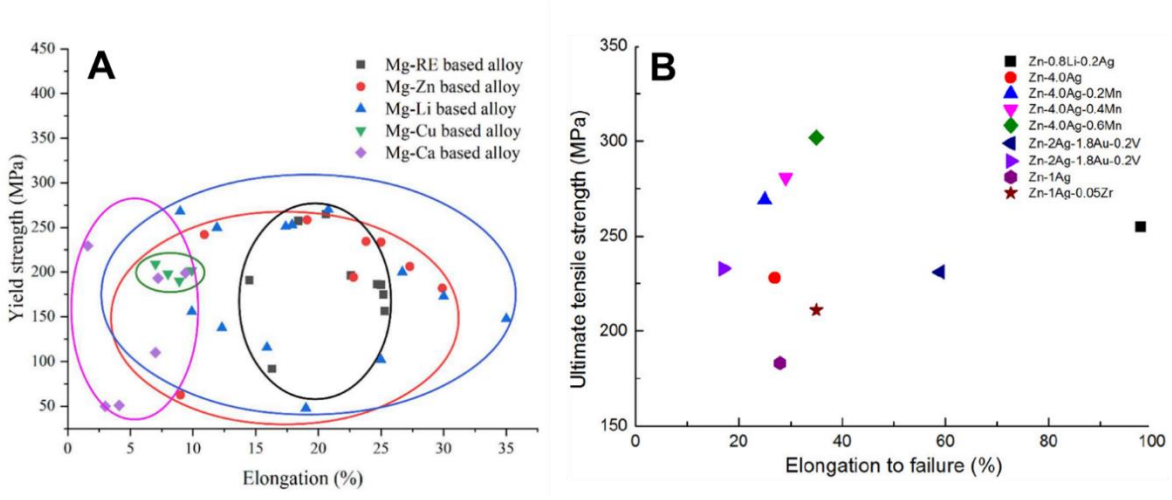

Figure 2.4 shows the mechanical properties of some Mg-based alloy. Image A is obtained from Chen *et al.*[147] and image B is obtained from Jessen *et al.*[148]. Both images are published under the Creative Commons CC-BY 4.0 Licence.

2.4 Mg-10Gd, Mg-2Ag and Mg-4Y-3RE in orthopedic application

With the advancement in medical technology, a variety of Mg alloy systems exist to be used as bone implant materials in the human body. The access to the medical market for Mg based implants necessitates a sequence of testing for assurance of their biocompatibility, safety and efficacy. To this end, Mg based implants are subjected to scientific investigations from the alloy production, to *in vitro* and *in vivo* tests prior to clinical applications. This section focuses on the current advances in terms of physicochemical properties, *in vitro* investigations and the *in vivo* osseointegration of three selected Mg-based implants namely, Mg-2Ag, Mg-4Y-3RE (WE43) and Mg-10Gd which are the alloy models considered in this thesis.

2.4.1 Physicochemical properties, *in vitro* and *in vivo* investigations of Mg-10Gd, Mg-2Ag, Mg-4Y-3RE

Ag has been in use as an antibacterial agent for several centuries due to its antibacterial and anti-biofilm formation capability[149] hence it is used in coatings, dressings and as alloyants[150–152]. These properties are also exploited in Mg alloy fabrication, thus, Ag is a common alloyant of Mg[153]. Metallurgical analysis and phase identification have revealed the addition of 2 wt.% of Ag to 98 wt.% of Mg significantly improved its mechanical properties and degradation resistance[153]. Furthermore, *in vitro* tests have shown that Mg-2Ag has acceptable cytocompatibility and negligible cytotoxicity in primary osteoblasts and cell lines with over 90 % bacteria-killing rate. The aforementioned properties are beneficial in curbing post-operative infections[153,154]. Costantino *et al*. further reported that Mg-2Ag has good cytocompatibility and inhibits M1 macrophage profile[154] as macrophages are key inflammatory cells that influence tissue healing and implant performance. *In vitro* investigations have shown degradation rates between 16.71 ± 0.62 to 0.68 ± 0.04 mm/year at 7 days[110] depending on the testing medium. The highest degradation rate (16.71 ± 0.62 mm/year) was recorded in phosphate buffered saline (PBS) while the lowest (0.68 ± 0.04 mm/year) was recorded in Dulbecco's Modified Eagle Medium (DMEM). This indictates the constituent and complexity dependency of testing mediums during Mg alloys degradation tests[155]. Generally, there exist an inverse relationship between degradation rate and complexity of testing medium[155]. In *in vivo* investigations, the reported degradation rates are 0.13 ± 0.04 mm/year at 7 days[110], 0.24 ± 0.13 mm/year at 1 month[110] and 0.02 ± 0.017 mm/year at 9 months[110].

Mg-10Gd is another extensively studied Mg alloy because of its desirable mechanical properties and corrosion resistance[156]. The properties include increased compressive yield strength and ultimate compressive strength, decrease in deformation in compression, improved corrosion resistance[156], homogenous microstructure and a weaker texture[157]. It has been shown that an addition as low as 0.75 wt.% of Gd to Mg yield Gd-rich short-range ordered (SRO) clusters that interact with dislocations in Mg resulting in increased strength and ductility[124]. In another study, the addition of 1wt.% Gd to Mg-4Zn exhibited higher tensile strength (336 MPa), elongation (20.6 %) and higher corrosion resistance than without the Gd due to the formation of a protectivoxide layer[158]. The *in vitro* degradation rates have been reported to be 1.57 ± 0.62 to 0.20 ± 0.01 mm/year after 1 week[110], 0.3 ± 0.01 mm/year after 2 weeks, 0.31 ± 0.02 mm/year at 4 weeks and 0.15 ± 0.03 mm/year at 8 weeks[157]. *In vivo* degradation data has also revealed that the degradation rate is 1.11 ± 0.05 mm/year at 1 week and 1.15 ± 0.19 mm/year at 4 weeks[159]. So far, *in vitro* tests have not recorded cytotoxicities associated with Mg-10Gd degradation[157] and in *in vivo*, no increment in Mg or Gd in blood levels has been detected[160]. Furthermore, Gd has been shown to possess anticarcinogenic properties[161].

Y is another widely used alloyant of Mg which is often combined with other REE such as Ce[162] and Nd[163]. Y is highly soluble and increases the creep resistance of Mg[164,165] while Nd and Ce improves the microstructure Mg. Mg-4Y-3RE (WE43) is a ternary Mg alloy that is made up of 4 wt.% Y, 3 wt.% Ce and 1 wt.% Nd and belongs to the WE series. Some form of the WE series has already obtained the CE mark and is currently used in clinics for various orthopaedic interventions[91]. Mg-4-Y-3RE alloys possess excellent strength and good degradation resistance[166,167]. It has been shown that, the addition of up to 5 wt.% of Y to Mg enhances the mechanical properties and improves the corrosion resistance. Hänzi *et al.* reported that depending on the surface treatment, Mg-4Y-3RE exhibits a decreasing degradation rate in SBF[168] as the formation of Y_2O_3 increases . Furthermore, Mg-4Y-3RE has been shown to have higher corrosion fatigue strength (40 MPa) compared to AZ91D (20 MPa) in SBF[169].

Due to the hierarchical composition of bone, the *in vivo* behavior of Mg based implants needs to be studied at different length scales and in different animal species. At the tissue level (macro-micro level), investigations are mostly related to the temporal assessment of mineral apposition rates and bone mass which are generally quantified as bone volume fraction (BV/TV); implant anchorage to the bone which is quantified as bone implant contact (BIC); degradation rate; evolution of the degradation products; tissue toxicities. The osseointegration of Mg-10Gd, Mg-2Ag and Mg-4Y-3RE is well studied at the tissue level. Beginning with Mg-2Ag, Jähn *et al.* reported enhanced osteoblastic function and subsequent bone formation with no systemic adverse effect at 133 and 210 days post implantation of Mg-2Ag nails in mice femora[170]. After 1 day of implantation of Mg-2Ag in a rat femur, large amounts of gas formation were observed but subsided after 7 days[110]. At 3 months post-implantation, there was a report of fibrous tissue encapsulation around Mg-Ag implants in rabbit femur[13]. For Mg-10Gd alloys, issues about their *in vivo* toxicities elicited health concerns. Gd as a free ion is toxic[171,172] but when it is alloyed with Mg, it is assumed that the alloy will be swiftly and entirely excreted from the body due to its degradation. In a study involving a rat model, Myrissa *et al.* reported the accumulation of Gd in the spleen, brain, muscle and heart but not in the blood after 36 weeks post implantation[160]. Later, several other researchers have reported otherwise: Gd is localized at the implantation site after the degradation of Mg-10Gd at 3 months[13,173]. The osteointegration of Mg-10Gd has been shown to be comparable to standard Ti implants[14] with good bone-implant contact[13,14]. As previously mentioned, some formulations of the WE are already in clinical use[91]. A typical example is the MAGNEZIX® compression screw (Syntellix AG, Hannover, Germany) which is used for surgical correction of hallux valgus. Several researchers have shown that the *in vivo* behavior of Mg-4Y-3RE yield acceptable BV/TV, BIC and a low degradation rate[13,86]. Although less health concerns have been raised against Mg alloys that contain RE elements, skeptics argue about the hepatoxicity of Y, Nd and the Ce components and are currently being researched[12]. As short- and mid-term tissue level evaluations of the aforementioned alloys have been well studied, it is worthwhile to further understand their long-term *in vivo* behavior to gain a thorough insight into their temporal performance prior to clinical application.

Nanoscale information mostly pertains to the bone ultrastructure and microstructure and are major determinants of bone-implant biocompatibility. In general, there exists sparse information on the ultrastructural adaptation of bone to Mg-based implants. Depending on the degradation rate, Mg is known to accumulate around blood vessels, lacunae and bone marrow and directly influences the hydroxyl apatite (HAP) structure[174]. Elsewhere, it was shown that the initial high concentration of Mg upon degradation reduces the hardness of the bone in its vicinity but is later resolved when the concentration of Mg decreases at later healing times[175]. Also, it was reported that the mineral platelets' orientation deviated from the normal orientation along the shaft of WZ21 implants[176]. Information on the bone ultrastructure pertaining to Mg-2Ag and Mg-4Y-3RE remains unexplored, however, that of Mg-10Gd is adequately studied. It

has been shown that the HAP crystal size and lattice spacing are different for Mg-10Gd compared to that of Ti, with the possibility of Mg deposition in the bone matrix[16]. To date, the impact of the degradation of Mg-based implants on the microstructure (bone porosity) of bone remains unexplored.

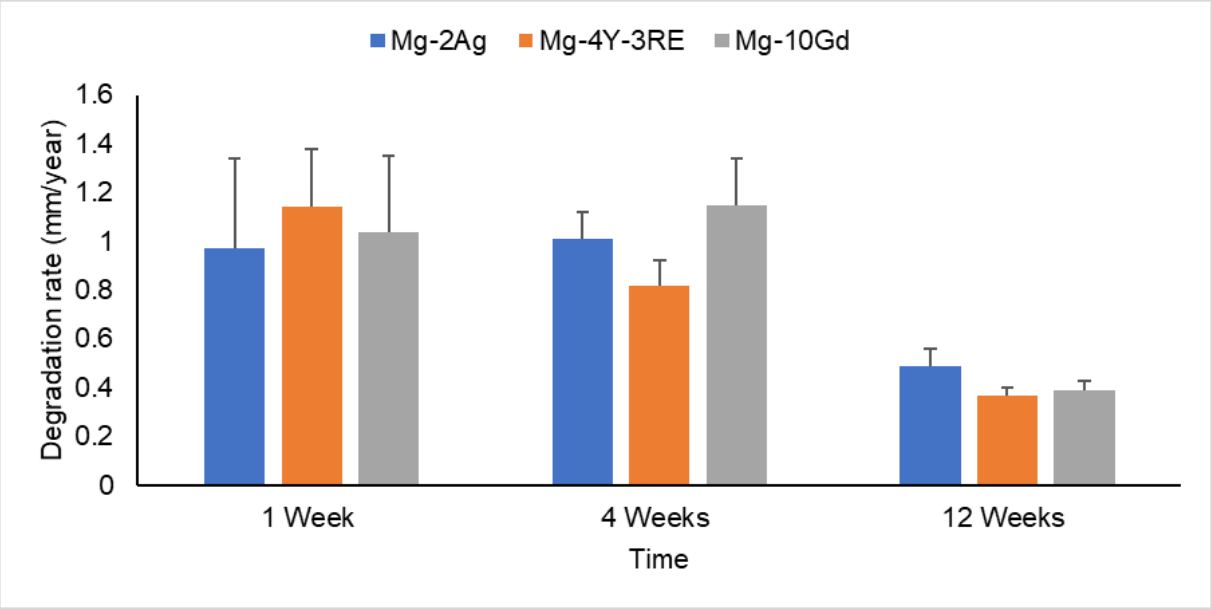

Figure 2.5 shows the visual comparison of the *in vivo* and *in vivo* degradation rate of Mg-2Ag, Mg-4Y-3RE and Mg-10Gd from 1 week (*in vitro*), 4 weeks (*in vivo*) and 12 weeks (*in vivo*). Values for the plot were obtained from Gali *et al.*[13]

2.4.2 Effect of Mg degradation on bone cells

It is well known that Mg^{2+} plays a critical role in numerous metabolic processes. However, in the case of increased Mg concentration, the possible interference of Mg degradation products on metabolic pathways has to be considered[177]. There is a general consensus that the degradation of Mg induces osteopromotive and osteoconductive effects on bone. Nevertheless, there have been conflicting reports from several cell culture studies regarding this hypothesis. Wang *et al.* showed in an experiment involving four different cell lines (primary osteoblasts, bone marrow-derived mesenchymal stromal cells, murine fibroblast cells and murine preosteoclast cells) that elevated concentrations of Mg^{2+} resulted in cytotoxic effects with average cell viability below 50 %[178]. For osteoblasts, Mg^{2+} has been shown to upregulate osteoblast markers such as ALPL and osteocalcin[179,180]. On the contrary, several other authors have reported decreased ALP activity in osteoblasts and a reduction in the mineralization of the ECM in Mg^{2+} extracts[111,181–184]. Wu *et al.* also reported an elevated resorption activity of osteoclasts in the Mg^{2+} and Mg extracts[185]. Later, the same authors reported elevated TRAP activity and increased expression of osteoclastic markers in Mg extracts[186]. It has recently been shown that pure Mg degradation did not alter the morphology of osteocytes, osteoblasts and osteoclast although a down regulation of MEPE was recorded for osteocytes in simple and triple cultures[187].

2.5 Synchrotron based imaging

2.5.1 Synchrotron radiation (SR) production

Current advances in synchrotron technology have led to improved beam quality for various applications. X-ray imaging based on SR is more advantageous than laboratory sources because of the flexibility with different phase techniques, high beam coherence, high beam collimation, and high brilliance which enable fast imaging[188]. Figure 1.6A is a schematic diagram of a synchrotron. In principle, electrons are generated in an electron gun through thermionic emission from a hot filament. The electrons are accelerated to approximately 100 MeV using a linear accelerator and injected into a booster ring where they are further accelerated. They are then injected into a storage ring to maintain a constant current[189]. While in the storage ring, the electrons are maintained in a closed trajectory by an array of magnets. The electrons within the storage ring possess relativistic velocities and kinetic energies in the GeV range[190]. The bending magnets in the storage ring deflect the electrons in an arced trajectory and produce SR. Insertion devices (wigglers and undulators) also produce SR but with significantly higher fluxes and brilliance than that of bending magnets[186]. Insertion devices operate by forcing the electrons to follow an oscillatory path within a set of magnets with alternating magnetic fields within the storage ring. The emission of SR by the electrons is associated with a loss of energy which is replenished by radiofrequency supply[189]. Beamlines are placed along the axes of the insertion device and are tangential to the storage ring. A typical beamline (figure 2.6) consists of the front end, optics and experimental hutch. The front end is responsible for monitoring the photon beam position. Within the optics hutch, the beam is monochromated by the use of X-ray mirrors it enters the experimental hutch[189].

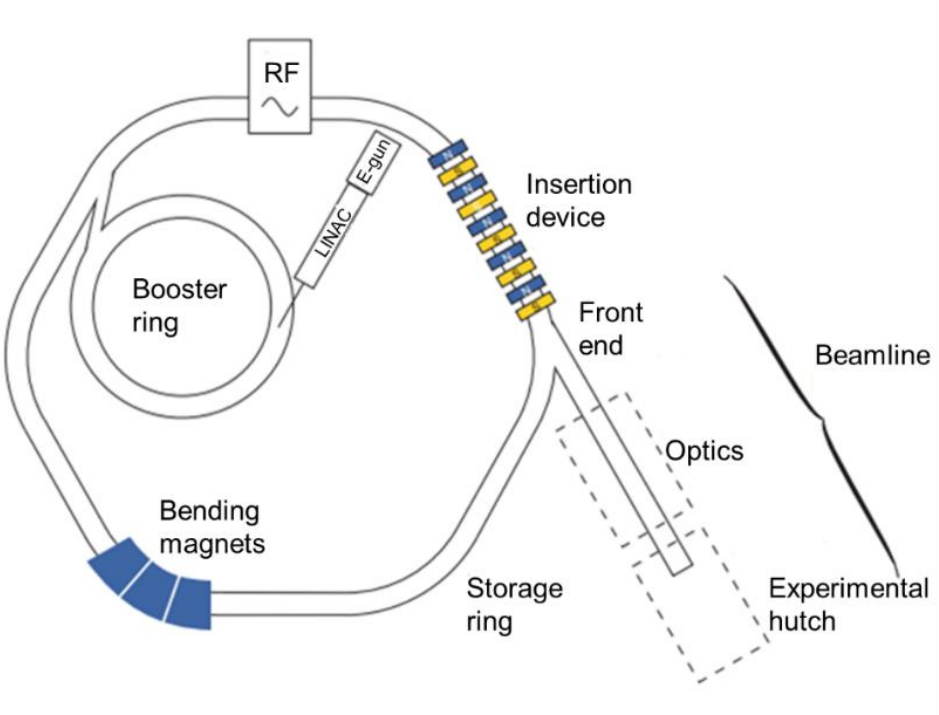

Figure 2.6: Diagram of a synchrotron layout showing the electron gun, the booster ring, the storage ring, the bending magnets, the radio frequency supply, insertion device, the front end, optics and the experimental hutch of a beamline[189].

2.5.2 SR imaging

2.5.2.1 SR micro-computed tomography imaging concept

By the use of X-ray tomography, the three-dimensional internal structure of an object can be visualized and quantified non-destructively by analyzing transmitted X-ray projections[191,192]. In X-ray imaging, contrast can be generated using either absorption or phase contrast. In this thesis, absorption-based SRμCT was utilized to quantify the bone healing response to Mg-based implants due to the excellent signal-to-noise ratio and resolution approximately 1 μm[193]. In absorption contrast mode, image contrast is generated based on the X-ray attenuation coefficient (μ) which is an inherent property of different sample features related to their electron density. The principle of absorption contrast mode imaging is shown in figure 2.7. In brief, the sample is placed perpendicular to the quasiparallel X-ray beam and rotated 360°. After interaction with the sample, the signal is converted to visible light using in a scintillator then magnified by magnifying optics and finally recorded by a detector. There are several detectors such as charged coupled device (CCD) and complementary metal oxide semiconductor (CMOS). The spatial resolution of the image depends on the point-spread function of the scintillator, the magnification factor of the microscope's objective lens (M), the pixel size (Δz) and the point spread function of the detector camera[189]. The number of acquired projections (N) to avoid undersampling is governed by the Nyquist sampling theorem given by equation 1.4[189]. To create the tomograms, the response (N_p) from each detector row of pixels as a function of rotation angle, namely, sinograms are generated and delivered into a computer. The detector pixel response is proportional to the intensity of the transmitted X-rays along a path (L) through an object and given by equation 1.5 and 1.6[189]. The projection (P) of a pixel at any given angle is the line integral of the object along the line L given by equation 1.7[189]. From the set of line integrals, the attenuation distribution is reconstructed for the whole object. From sinograms, tomograms are reconstructed using mathematical algorithms such as filtered back projection which is based on the radon transform[194].

$$N = N_p \times \frac{\pi}{2} \tag{1.4}$$

N_p is the number of pixels in the detector row.

$$I = I_0 e^{-\mu_1 \Delta z} e^{-\mu_2 \Delta z} e^{-\mu_3 \Delta z} \dots e^{-\mu_M \Delta z} \tag{1.5}$$

$$I_0 \exp\left(\sum_{k=1}^{M} \mu_k \, \Delta z\right) \tag{1.6}$$

Where μ is the X-ray attenuation coefficient, I is the transmitted X-ray and I_o is the incident X-ray.

The projection measurement is defined as:

$$P = -\ln\left(\frac{I}{I_0}\right) = \sum_{k=1}^{M} \mu_k \Delta z \approx \int \mu(z) dz \tag{1.7}$$

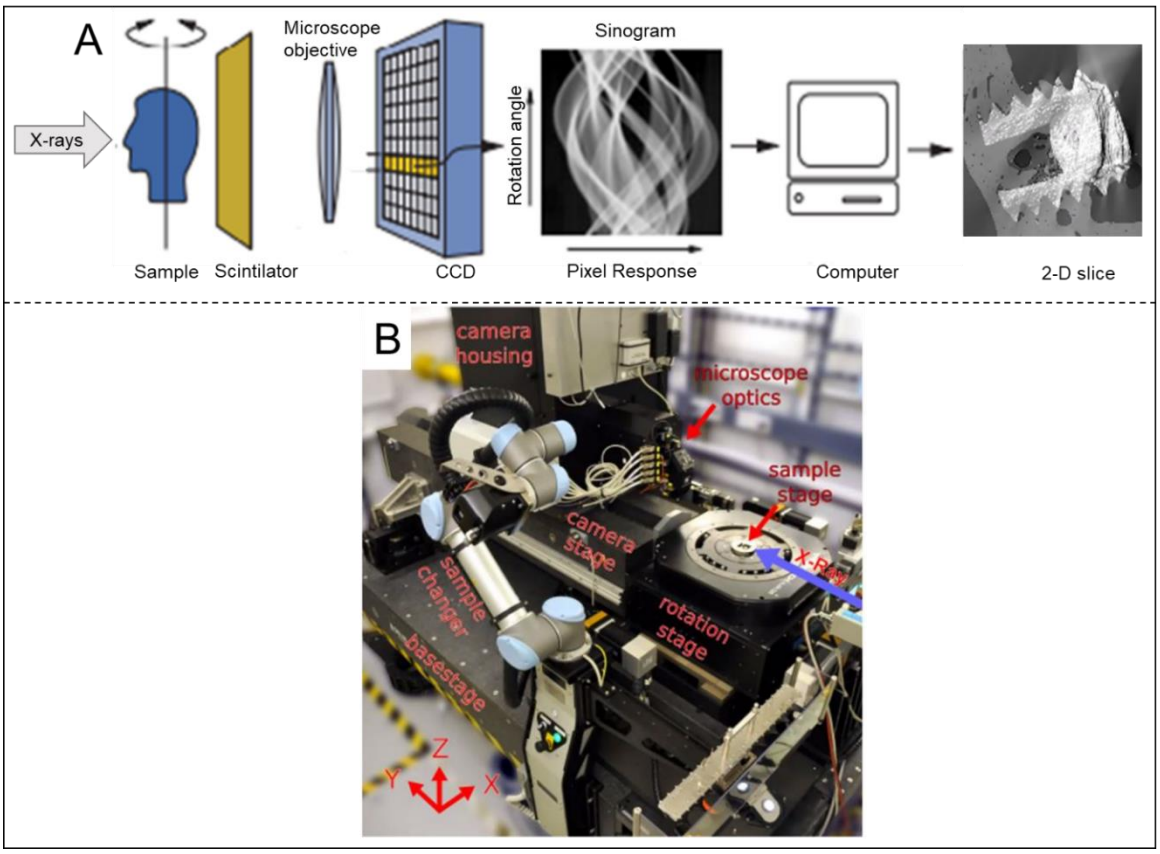

Figure 2.7: (A) schematic diagram of µCT imaging. Image with permission from[189]. (B) µCT imaging setup at the P05 beamline operated by Helmholtz-Zentrum Hereon[195].

2.5.2.2 Transmission X-ray microscopy (TXM)

To obtain detailed qualitative and quantitative morphological analysis of the LCN, which have structures measuring less than 200 nm, transmission X-ray microscopy (TXM) in phase contrast mode was preferred in this thesis. In contrast to bench top machines, SR based nanotomography techniques offer fast scanning times and/ high image quality due to the high brilliance of synchrotron sources[196]. In TXM imaging, spatial resolution of approximately 50 nm[197,198] can be achieved enabling the visualization and assessment the morphology of the LCN in conjunction with Zernike phase contrast. Zerinke phase contrast technique enables fast imaging at a single distance in comparison to other phase contrast techniques[194] such as free-space propagation[199] and grating interferometers[200]. Usually in phase contrast techniques, the phase shift introduced in the transmitted X-rays caused by differences in the refractive indices of the features in a sample is utilized to generate the image contrast. Alternative SRnCT techniques, such as ptychography and near-field X-ray holotomography (NFHT), were found not optimal for the specific research needs of this thesis. With NFHT, imaging is performed at several sample-to-detector distances for quantitative phase reconstruction[201] which makes the phase retrieval process cumbersome prior to image reconstruction[202,203]. For ptychography, 2D diffraction patterns of the sample are first obtained from which quantitative phase projections can be retrieved. Whereas with full-field TXM, the entire sample can be illuminated at once and at a single distance resulting in shorter imaging time[204]. Furthermore, ptychography can take several hours to image a 40 µm diameter sample whereas, depending on the desired image quality, TXM can image the sample in minutes to hours[204–206]. Considering the factors mentioned above, it was opted to utilize TXM in combination with Zernike phase contrast for the detection of the LCN within the bone. Zernike phase contrast is

a well-established technique in full field TXM[207] for various applications. Figure 2.8 is a typical layout of a full-field TXM from a synchrotron source. In brief, the X-ray beam is focused onto the sample with a beamshaping condenser. Afterwards, the X-rays are focused and magnified with a Fresnel zone plate (FZP) objective lens onto a detector. To enhance the contrast, a phase ring is used (eg. Zernike phase ring). A rotating paper is used as a decoherer in order to reduce coherence effects while a beam stop blocks the direct beam. Based on Abbe's theory, the radiation illumination of an object is divided into diffracted and undiffracted components[208]. The undiffracted component, i.e., the background information, is spatially separated in the back focal plane of the objective lens (FZP) using Zernike phase rings (90° for positive contrast and 270° for negative contrast). The phase-shifted, undiffracted component interferes with the diffracted (foreground signal) component. The phase contrast image is formed by translating the phase modulations into intensity modulations in the image plane within the detector system. Reconstruction of the 3D tomogram from TXM projections is performed the same way as that of the SRµCT reconstruction described above.

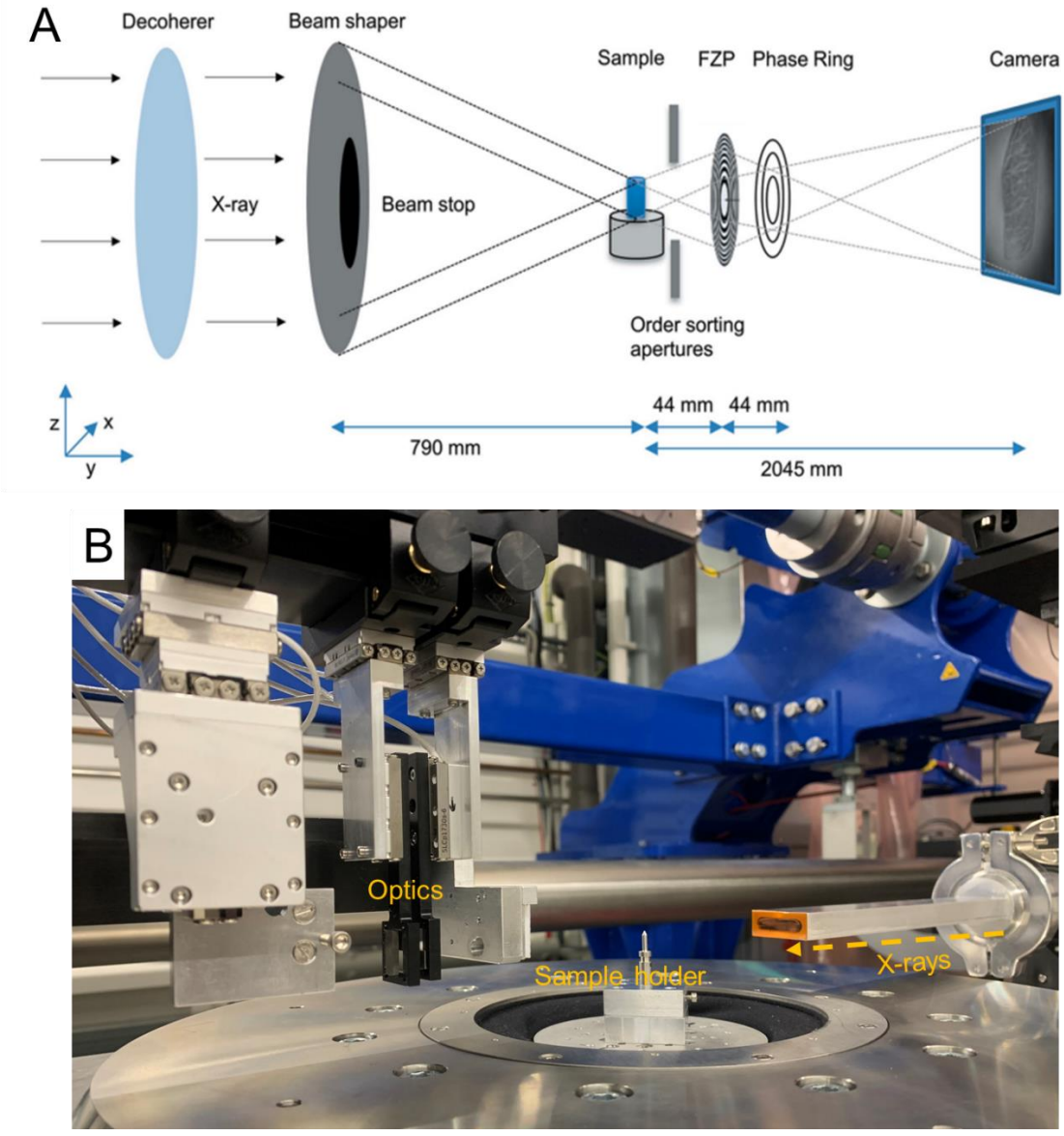

Figure 2.8: (A) schematic diagram of Zernike phase contrast imaging[204]. (B) Full-field nanoCT imaging setup at the P05 beamline operated by Helmholtz Zentrum.[209]

2.5.2.3 Micro X-ray fluorescence (µXRF) imaging

In certain instances, apart from the 3D internal structure of a material, knowledge of its elemental composition is needed to gain deeper insight. In this regard, micro X-ray flouresence (µXRF) imaging is desirable. In principle, when a material interacts with high energy X-rays, inner electrons within the inner shell of the atoms within the material are knocked out which creates a vacancy. This vacancy is occupied by electrons from the outer shell to stabilize the atom, in the process seconday X-ray photons are released. The secondary X-ray photon is termed fluorescence[210]. Every element produces fluorescence that is characteristic (unique) to themselves which enables the identification of the presence of that specific element in a material[210]. In µXRF imaging, the emitted fluorescent energy is recorded by a detector where it is converted into an electrical signal and digitized. The digitized image can be qualitatively or quantitatively analyzed.

2.5.3 SR imaging of Mg-based implants and surrounding tissue

To accelerate the translational application of Mg-based implants in the clinics, prior testing to ascertain their suitability is indispensable. In this regard, synchrotron radiation techniques have been pivotal in studying the morphology and composition of the implant and the surrounding tissues by spectroscopic techniques or direct imaging[193]. With a focus on direct imaging, the use of SR micro-computed tomography (SRµCT) and SR nano-computed tomography (SRnCT) are powerful tools to investigate osseointegration *ex vivo*[193]. The hierarchical nature of bone requires that osseointegration has to be characterized at different length scales in order to fully understand the impact of Mg degradation on bone. On the micro-macro scale, SRµCT imaging has been successfully used to characterize the osseointegration of Mg-based implants *ex vivo* and in 3D[193]. *Ex vivo* investigations are carried out using explants (implant plus surrounding bone) which are obtained after experimental animals are sacrificed during *in vivo* investigations. The explants are either imaged embedded in PMMA, critically point dried or frozen, depending on the research question. Following comprehensive image analysis, parameters that are usually quantified are the BV/TV, BIC and the degradation rate. The first SRµCT study involving Mg-based implants was conducted by Witte *et al.* where the degradation rates of AZ91D and LAE442 were calculated following implantation in guinea pigs for 18 weeks[211]. Afterwards, several other studies[13,14,157,212,213] have also utilized SRµCT to quantity the degradation rate, BIC and BV/TV of various Mg-based implants in different animal models at different time points. Notably, BIC was first reported by Galli *et al*. who simultaneously studied the Mg-10Gd, Mg-2Ag and WE43 in comparison to Ti implants in a rabbit model for 1 and 3 months. They reported a BIC of less than 50 % for the Mg-based implants in comparison to 80 % for Ti[13]. In addition to the bone healing healing response, the homogenous degradation and uniform distribution of the degradation products of Mg-based implants are indispensable in accelerating their clinical application. To this end, µXRF has been employed to study the evolution of degradation products of some Mg-based implants. Helmholz *et al*. has succesfully quantified the degradation products of Mg-2Ag alloy where, elevated levels of potassium and decreased levels of calcium were detected after 133 days of implantation[214]. Furthermore, another study recorded the migration of Y into the adjacent bone in a WZ21 alloy (2 wt. % Y,1 wt. % Zn, 0.25 wt. % Ca, 0.15 wt. % Mn, and 96.4 wt. % Mg) after 18 months of implantation in a rat model[215].

Macro-scale information may be insufficient to fully understand the behavior of Mg-based implants *in vivo*. In that case, a sub-micron resolution which can be achieved with SRnCT imaging is desirable. With sub-micron resolution, the microstructure and the ultrastructure of the bone adjacent to the implants can be studied. Regarding the bone microarchitecture, the

LCN is popularly studied because in them reside the osteocytes and their cell processes which orchestrate bone remodeling[216,217]. The LCN has been well studied but in different pathological contexts[218–224] where changes in their morphology and density are usually quantified. In peri-implant research, several researchers have detailed the impact of biomaterials on the LCN morphology in 2D technologies[49,57–59]. Although information from both 2D technologies have revealed altered LCN morphology and organization during peri-implant bone healing, the advantages of utilizing high-resolution 3D SRnCT are pertinent to accurately quantify LCN morphology[225].

2.5.4 Image-based modelling of the LCN

To understand osteocyte's mechanosensation several computational models have emerged to calculate local stresses, molecular signalling and the transport of nutrients and waste products. In view of the fluid flow hypothesis which explains that osteocytes are activated due to fluid shear stress acting on the cell process membrane[39], homogenized poro-elastic models were used to visualize the fluid flow patterns within the bone osteons[226–228]. Although homogenized models enhanced the study of mechanosensation at the osteon level, such models obscured the influence of osteocytes by limiting transport within them and/or disregarding the potential role of molecular cues that affects osteocyte mechanical stimulation[229]. A robust approach was to study the deformations of a single isolated cell subject to a well-defined mechanical load. On this note, several finite element (FE) studies have confirmed that the osteocytes' cell processes experience higher stresses than the cell body[230–232]. In a fluid structure interaction FE model, Verbruggen *et al*. successfully calculated the fluid velocity and shear stress in the osteocyte cell body and cell processes[230]. Although idealized models yield valuable information, Qiu *et al*. demonstrated that the use of the actual cell geometry instead of an assumed idealized shape could accurately describe the cell behavior under fluid flow[233]. The aforementioned models do not directly pertain to mechanosensation in peri-implant bone healing, however, they provide vital cues on the fluid flow mechanism within the LCN. These cues could be useful in understanding mechanosensation in peri-implant remodelling, which is one of the aims of this thesis.

Chapter 3

Materials and method

Study I: Assessing the long-term *in vivo* degradation behavior of Mg-10Gd, Mg-4Y-3RE and Mg-2Ag alloys.

The aim of **Study I** was to investigate the long-term osseointegration of Mg-10Gd, Mg-4Y-3RE and Mg-2Ag with a focus on bone formation, implant anchorage and evolution of their degradation products. Secondly, the influence of blood pre-incubation of the aforementioned implants on their osteointegration was also investigated. The description of materials and methods for **Study I** has been published here[18], thus this section is paraphrased from the publication.

3.1.1 Material production

The Mg-based alloys used as implant materials for this study were produced from the following materials: magnesium (99.99%, Xinxiang Jiuli Magnesium Co. Ltd., China), yttrium (99.95%, Grirem Adv. Mater. Co. Ltd, China), gadolinium (Gd, 99.95%, Grirem Adv. Mater. Co. Ltd, China), a rare earth mixture (Nd and Ce), (RE, Grirem Adv. Mater. Co. Ltd, China) and silver (Ag, 99.99% ESG Edelmetall-Handel GmbH & Co. KG, Germany). The production of the implant materials was performed at the Functional Materials department of the Institute of Metallic Biomaterials (Helmholtz-Zentrum Hereon, Germany) using the permanent mold direct chill casting technique[234]. In the first step, the respective alloyants (Gd, Ag, Y, RE) were pre-heated and separately added to molten pure Mg at 720 °C while continuously stirring for 15 minutes. The mixture was poured into a pre-heated (550 °C) permanent steel mold (S355, material number: 1.0577). The casting procedure was done in a controlled environment with 2 vol.% Sulfur Hexafluoride followed by solution heat treatment (T4) for 6 h at 420 °C for Mg-2Ag, 500 °C for Mg-10Gd and 550 °C for Mg-4Y-3RE. The billets were extruded using the indirect extrusion method. For Mg-2Ag, the extrusion was performed at 360 °C with a speed of 2.5 mm/s. For Mg-10Gd, extrusion was performed at 430 °C with a speed of 3.5 mm/s, while Mg-4Y-3RE was extruded with a speed of 3 mm/s and a temperature of 390 °C. After extrusion, the rods were refined to obtain threaded mini screws with a length of 4 mm and an outer diameter of 2 mm. The screws are packaged in sealed plastic bags and sterilized by gamma radiation (dose of 27 kGy at BBF, Sterilization service, Kersen, Germany).

3.1.2 Characterization of initial screw volumes

To obtain the reference screw volumes prior to implantation, the initial volume of each screw was determined. The selected screws were scanned using a Phoenix Nanotom benchtop µCT (GE inspection and sensing technologies, Wunstorf, Germany) at an operating voltage of 100 kV and a current of 70 µA. Each scan was performed with an exposure time of 1000 ms, 2700 projections and with a binned voxel size of 2.5 µm. The image data were processed in the open-source image processing software, Fiji (Fiji is just ImageJ, GPL v2)[235,236]. Prior to the volume calculation, the image data were binarized using interactive thresholding, then the

voxel counter plugin was used to sum the foreground voxels. The summed voxels were converted to mm^3 by multiplying with the voxel size cubed.

3.1.3 Animal experiment for the *ex vivo* study

The French Ministry of Higher Education and Research approved the *in vivo* study (approval number 00391-01). The study was performed at the National School of Veterinary Medicine of Maison-Alfort (Maison-Alfort, France) using six mature female New-Zealand white rabbits weighing between 3-4 kg. The animals were anesthetized with 250 mg/kg of medetomidine (Domitor, Zoetis, France), 20 mg/kg ketamine (Imalgene 1000, Merial, Sanofi, France) and 1 mg/kg of diazepam (Valium, Roche, France) intramuscularly. Prior to implantation, three of the screws (one per material) were pre-incubated in a few ml of blood samples collected from each animal. The pre-incubation was done by adding the collected blood directly to the selected screws in their sterilized containers for 30 minutes. 1 mg of lidocaine was locally administered into the surgical area. Within the distal femoral metaphysis, a full thickness incision was made, exposing the bone in the diaphysis of the femur. Afterwards, a full thickness incision of three osteotomies were performed in this region with a rotating drill under irrigation with sterile saline. The osteotomies were performed first with a round bur with a diameter of 1.4 mm, then with a parallel bur with a diameter of 2 mm and finally tapping with a Ti instrument with the same threaded shape of the Mg-screws. Using a manual screwdriver, three Mg-screws (one per material) were inserted into the osteotomies with a distance of 5 mm between each screw (figure 3.1). Within each leg, either three pristine Mg-screws or three blood pre-incubated Mg-screws were implanted based on random allocation of the right or left leg. A total of 36 screws were implanted in six animals (Table A). Subsequently, the periosteum, muscle and skin were repositioned and sutured with a resorbable suture in 2 layers (Vicryl 3.0). The animals were administered antibiotics and analgesics therapy for 5 days after the surgery and were allowed to freely move and eat *ad libitum*. The animals were euthanized with a lethal dose of sodium pentobarbital (Euthasol, Virbac, Fort Worth, United States) after 6 and 9 months post-implantation (three animals each per time point). The implanted legs were dissected using a cylindrical trephine bur (3 mm in diameter) to harvest the screws with the surrounding bone.

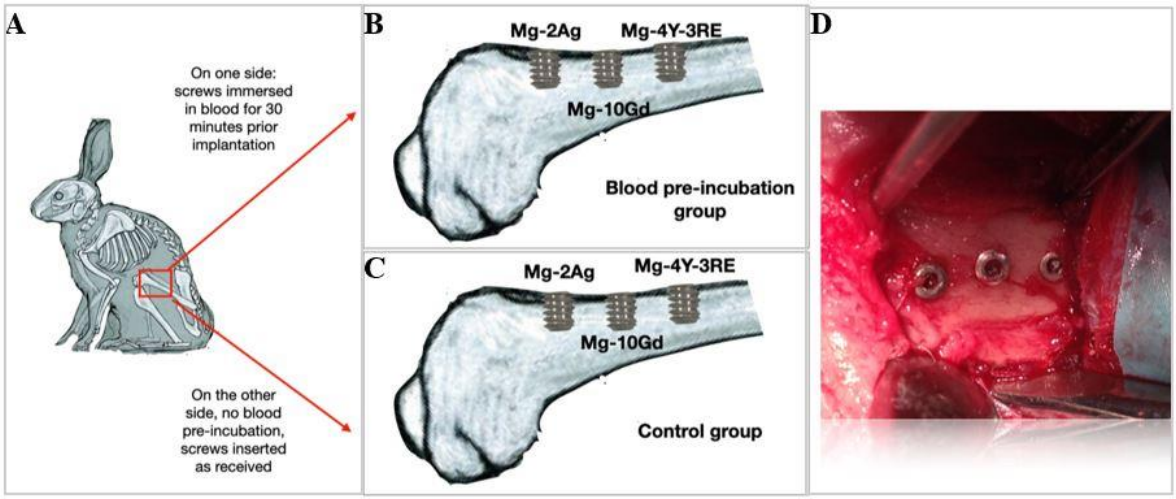

Figure 3.1: Schematic figure of the implanted Mg-based screws in the rabbit femur. A), B) & C) Schematic figure of the insertion of the screws into the rabbit femur. Each rabbit received 3 blood pre-incubated screws, one per material, on one leg and 3 screws without blood pre-incubation, one per material, on the other leg, for a total of 6 screws per rabbit (36 screws in the entire study). D) A photo of three screws in one rabbit femur. From Sefa *et al*[18]. Published under the Creative Commons CC-BY 4.0 Licence.

3.1.4 Explants preparation for *ex vivo* experiments

After harvesting the bone implant blocks with implant screws (explants), it was necessary to prepare and preserve the samples for further analysis. In order to halt further degradation of the Mg-screws, the explants were fixed in 70 % ethanol for 24 hours under vacuum and frozen at -80 °C. At this condition, the electrochemical reactions are absent thereby halting the degradation process. Considering the long scanning times of SRµCT, the samples were also critically point dried to ensure the preservation of the explants during scanning. Critical point drying is a common method that is normally used in cell cultures to preserve cell morphology by removing all the water from the cells[237] prior to scanning electron microscope examination. Critical point drying exploits the properties of CO_2, which under certain pressure and temperature becomes liquid or gas with zero surface tension. Before infiltrating the explants with CO_2, they were first dehydrated in ascending concentrations of 2-Propanol (Sigma-Aldrich Chemie GmbH, Munich, Germany) for 24 hours. The samples were subsequently transferred into a CriticalPointDryer (Leica EM CPD300, Leica Mikrosyteme Vertrieb GmbH, Wetzlar, Germany) sample holder and 2-Propanol was replaced with CO_2. The temperature and pressure of the Critical Point Dryer were tuned until complete evaporation of the CO_2 (40 °C and 75.5 bar) resulting in completely dried samples with unaltered morphology. Table 3.1 is the summary of the explants used for **Study I**.

3.1.5 Undecalcified-tissue histology

To investigate the structure and the morphology of the peri-implant bone tissue, non-decalcified histology was performed on the explants of all the Mg screw types and at both time points (6 and 9 months). With undecalcified histology, fixed specimens are directly embedded in hard plastic resin without decalcification. The embedded samples are then cut, stained with a dye and subsequently observed under a light microscope, resulting in high resolution 2D images of the peri-implant bone and the implant screw. Identification of tissue and cellular structures are based on their affinity to the dye used for staining. To this end, first the critically point dried samples were incubated in 100 % ethanol for 1 week followed by infiltration with methyl-methacrylate based resin (Technovit 7200, VLC; Hereaeus Kulzler, Germany). The samples were then photopolymerized to render them into hard blocks. Based on the grinding and cutting protocol stipulated in Donath's protocol[238], 40 µm thick sections of the explants were cut using an Exakt system (Exakt Apparatebau, Nordertedt, Germany) followed by staining with Toluidine blue dye (Histlab, Göteborg, Sweden). The stained specimens were imaged with an optical light microscope (Eclipse ME600; Nikon, Tokyo, Japan) using a digital camera (DS-Ri2, Nikon, Japan) and NiS elements software (Nikon, Japan).

Table 3.1: Number of explants used in **Study I**

Time point (months)	Alloy type		
	Mg-10Gd	Mg-4Y-3RE	Mg-2Ag
6	6	6	6
9	6	6	6

3.1.6 SRµCT experiment

SRµCT Image Acquisition

SRµCT imaging was performed on the explants to investigate the bone response to the Mg-based implant screws at 6 and 9 months post-implantation. The image acquisition was performed in absorption mode in two batches at the P05 imaging beamline IBL operated by Helmholtz-Zentrum Hereon at the PETRA III storage ring at the Deutsches Elektronen Synchrotron (DESY), Hamburg, Germany[195,239–241]. The first batch consisted of 24 samples and were scanned at 45.33 KeV with 2400 projections resulting in a 3D image volume with binned effective pixel size of 2.56 µm. The second batch had 12 samples and were scanned at 51.50 keV with 4800 projections with a binned effective voxel size of 3.84 µm. In both batches, the samples on the rotating stage were rotated in steps of 0.2° within a 180° range in a total of 900 steps. Reference images were taken intermittently to correct variations of the X-ray beam. After the interaction of the X-ray beams with the sample, the attenuated beams are converted to visible light by a scintillator and recorded by a CCD camera. The image data were subsequently reconstructed using filtered back projections algorithm[242].

SRµCT Image processing

The resulting tomographic image data were processed in Fiji/ImageJ to reduce their size to accelerate analysis. Processing of the image data entailed isotropic binning with a factor of two followed by reducing the bit depth from 32 bits to 16 bits within -0.004 to +0.02 range resulting in 5.12 µm voxel size for the first batch of data and 7.68 µm for the second batch of data. Afterwards, the image data were filtered with iterative nonlocal means denoising filter[243]. To equalize the voxel size of the image data from the two batches, the image data from the first were resampled to 7.68 µm. Prior to quantitative analysis, segmentation is necessary in order to delineate the voxels to either bone label, screw label or background. To this end, the semi-automatic WEKA segmentation plugin in Fiji/Image was employed by exploiting the X-ray absorption coefficients of the different regions within the image. The differences in the X-ray absorption coefficient resulted in variations of the grey scale intensities which enabled the delineation of the image regions into bone, screw or background labels. The resulting image labels were further manually corrected in Avizo software (version 9.4.2, Thermo Fisher Scientific, Waltham, MA) followed by registration and resampling to a custom-made orientation cylinder as a pre-requisite for the quantitative analysis. Figure 3.2 shows the result of the image processing steps.

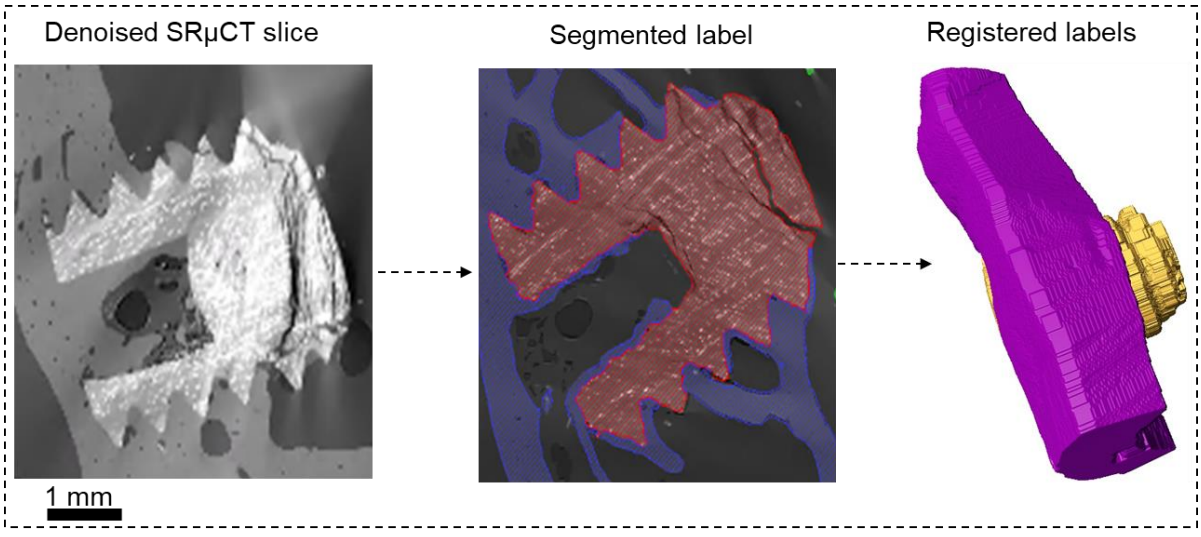

Figure 3.2: SRµCT labels obtained during image processing

Image quantification

To quantitatively assess osseointegration, the BV/TV and BIC were calculated over the whole image volume (3D) of the tomograms within 300 µm volume of interest (VOI) around the screws using a custom-written Fiji script[244]. The analyzed VOI represented the region in the screw thread and the thread tips. Unfortunately, the degradation rate could not be quantified because the degradation layers could not be distinguished from the residual screws due to the similarity in their electron densities (figure 3.2). Nonetheless, the final volumes of the 'remnant screws' were calculated and compared with their initial screw volumes. Remnant screw refers to the residual screw and the undistinguished degradation layer. The final remnant screw volumes were calculated in Avizo software (version 9.4.2, Thermo Fisher Scientific, Waltham, MA) as the screw voxels multiplied by the voxel size cubed. One important aspect of osseointegration is the BIC, which is defined as the region of the screw in contact with the surrounding bone. The normalized BIC was calculated using equation 1. Another quantitative measure of osseointegration is the BV/TV, which depicts the amount of bone formed around the screws within the observation period. Equation 2 was used to quantify the BV/TV as the ratio of mineralized bone (BV) to the volume of bone tissue (TV).

$$3D - BIC\ [\%] = \frac{\#\ surface\ voxels\ of\ implant\ in\ contact\ with\ bone}{\#\ total\ surface\ voxels\ of\ screw} \quad (1)$$

$$3D - BV/TV\ [\%] = \frac{\#\ voxels\ of\ bone\ volume}{\#\ voxels\ of\ total\ volume\ of\ the\ VOI} \quad (2)$$

3.1.7 µXRF experiment

To characterize the degradation products of the screw types after the *in vivo* degradation, µXRF was performed on the explants. For this, elemental mappings of the various screw types were performed with Tornado M4 µXRF spectrophotometer (Bruker Nano, Berlin, Germany) set up with a rhodium (Rh) tube and tungsten (W) tube at a working voltage of 50 kV and an anodic current of 600 µA. The fluorescence signals generated after illuminating the samples with X-rays are detected by a Bruker XFlash® silicon detector with an energy resolution of 45 eV for 250 cps. The measurement was carried out in vacuum (20 mbar) using a beam spot size of 25 µm and a beam spot distance of 25 µm with an acquisition time of 1.5 ms per pixel. Obtaining high resolution image data required preforming the measurement in three cycle runs resulting in 2D image datasets which were subsequently analyzed with Bruker ESPRIT microanalysis software version 1.3.0.3273.

Statistical analysis

All statistical analyses were performed in Origin 2021b. The mean and standard deviation of all analyzed parameters were calculated for each screw type per time point. The group means were compared using one-way analysis of variance (ANOVA) with Tukey´s multiple comparison test assuming a normal distribution. In addition, a paired t-test was performed between the group means of the blood pre-incubated screws and the control group to investigate the effect of pre-incubating the screws on the BV/TV and BIC for each screw type and at each post-implantation time. The parameters were compared between the alloy types at the implantation times (6 and 9 months). All analyses were performed at 95 % confidence interval, thus, a p-value below 0.05 was considered statistically significant.

Study II: Characterizing the microstructural adaptation of bone around Mg-10Gd using multiscale imaging.

The microstructural evaluation in **Study II** involved characterizing the lacunar and vascular density around Mg-10Gd at 4, 8 and 12 weeks post-implantation using SRµCT. Then, the LCN architecture around Mg-10Gd was characterized at 10 and 20 weeks using TXM. Finally, the fluid flow dynamics based on the TXM data was evaluated using finite element modelling. **Study II** has been published in Bioactive Materials journal thus the following sections are paraphrased from the publication[19].

3.2.1 Material production

The Mg-10Gd screws used for the SRµCT and TXM experiments in **Study II** were prepared using a standardized protocol[157]. The preparation of Mg-10Gd was performed in an induction furnace using a combination of Argon and 3 volume percent of Sulphur Hexafluoride as shielding gas. In the first step, Mg was melted and cast based on permanent mold direct chill casting method. Afterwards, 10 wt.% Gd was added to the molten Mg at 700 °C and stirred for 20 minutes at a rotation speed of 150 per minute. A permanent steel mold (S355, material number: 1.0577, diameter of 110 mm, height of 230 mm) was pre-heated to 680 °C and the molten materials were transferred into it followed by quenching the ingots with water to cool them down[234]. The ingots were further heat treated (T4) at 525 °C for 8 h and again quenched with water. Subsequently, the ingots were indirectly extruded to a final diameter of 12 mm with an extrusion ratio of 84, a ram speed of 0.52 mm/s and a temperature of 400 °C. Using the electrical discharge method, 3 mm diameter rods were cut from the extruded bars. The 3 mm rods were further machined by turning and slitting into headless screws with a length of 4 mm, a diameter of 2 mm with M2 thread and a 0.5x0.5 mm slot. In both the SRµCT and the TXM experiments, Ti screws which were purchased from Prominic AB (Mölndal, Sweden) were used as a reference material.

3.2.2 Animal experiment for the *ex vivo* studies

The two *ex vivo* experiments (SRµCT and TXM) were implemented using explants from two different animal experiments that were performed by project partners at the Malmö University in Mälmo and the Christian Albrecht University of Kiel. It is worth mentioning that the resulting ex-plants have also been studied to quantify the ultrastructural adaption of bone here[15].

For the SRµCT animal experiment, the Malmö/Lund regional board for animal research, Swedish Board of Agriculture approved the animal experiment with approval number DNR M 188-15. Fifteen Sprague Dawley male adult rats with mean weight of 350 g were used for the study. Prior to the implantation, the animals were housed in cages with two or three animals per cage. Details of the implantation protocol can be found in the publication by Krüger *et al.*[14]. In brief, the rats were administered a general anesthesia with an intraperitoneal dose of Fentanyl 300 µg/kg plus Dexmedetomidin 150 µg/kg. The legs of the rats were shaved and disinfected with Chlorhexine ethanol solution 0.5 mg/ml, Klorhexidinsprit (Fresenius Kabi, Uppsala Sweden) and a local anesthesia was injected in the tibial area (1 ml Xylocaine, Aspen Nordic, Ballerup, Denmark) and a full thickness flap was created. After exposing the tibia metaphysis, an osteotomy was created by drilling with a 1.4 mm round bur and then enlarged with a cylindrical bur of 1.6 mm diameter while simultaneously irrigating with sterile saline. After tapping, the screws were inserted monocortically using a manual screw driver, one screw was

inserted in each leg with about two or three threads of the screw sticking out of the tibial plate. Each rat received two Mg-10Gd screws or two Ti screws making a total of 30 screws with random allocation to the left or right leg. Afterwards, the flaps were sutured and the rats received an analgesic dose of Buprenorfin of 0.01 – 0.05 mg/kg (Temgesic, Indivior Europe Limited, Dublin, Ireland). The rats were fed *ad libitum* and moved freely in the cage. Ten rats (five rats per material) were euthanized at 4, 8 and 12 weeks post-implantation respectively with a lethal dose of anesthetic. After euthanasia, the legs were dissected to expose the bone around the implant area. Bone together with the implants were extracted using a trephine bur of 6 mm diameter. The bone-implant blocks were then fixed with 70 % ethanol for at least 1 day followed by dehydration in a graded series of ethanol. All explants were prepared and preserved using the protocol described in critically point dried in Chapter 3.1.4. A summary of the number of explants and time points used in the SRµCT study is in table 3.2.

TXM animal experiment involved eighteen Sprague Dawley rats obtained from Charles River Laboratories (Sulzfeld, Germany). Approval of the animal experiment was given by the Ethics Committee for Animal Experiments at Christian-Albrechts University of Kiel, Germany with approval number V 241-26850/2017(74-6/17). The animals were housed in cages with two or three animals per cage and fed *ad libitum*. In brief, the rats were administered a general anesthesia with an intraperitoneal dose of 75 mg/kg Ketamine and 0.5 mg/kg Medetomidine. The legs of the rats were shaved and disinfected with a skin disinfectant (Octenisept) and a longitudinal incision was made medially along the lower leg 8 mm below the knee joint (about 2 mm distal to the knee joint and about 1 mm median to the crest of the tibia) with a scalpel. After exposing the tibia metaphysis, an osteotomy was created by drilling with a 1.4 mm electric drill (dental micromotor Marathon s04 (N7S)). The screws were inserted monocortically using a manual hand drill, with about two or three threads of the screw sticking out of the tibial plate. Each rat received a Mg-10Gd screw or a Ti screw making a total of eighteen screws with random allocation to the left or right leg. Afterwards, the wound was sutured with an absorbable suture (5-0, Vicryl USP) and the rats were placed on a warm plate and partially antagonized (Atipamezole, 1 mg/kg bw, 50 µL subcutaneously). The rats were administered Metamizole (100 mg/kg) after 2 hours of surgery and tramadol for 5 days after surgery via the drinking water (in the dosage of 0.5 mg/ml drinking water, according to Lang *et al.*[245]. After 72 hours, the rats received an analgesic dose of 0.5 mg/mL of tramadol via drinking water. The rats were fed *ad libitum* and moved freely in the cage. Afterwards, they were euthanized at 10 and 20 weeks post-implantation with a lethal dose of anesthetic. The legs were dissected to expose the bone around the implant area. Bones surrounding the implants were explanted using a trephine bur of 6 mm diameter. The bone-implant blocks were then fixed with 70 % ethanol for at least 1 day followed by dehydration in graded series of ethanol and embedded in methyl-methacrylate based resin (Technovit 7200, VLC; Hereaeus Kulzler, Germany) by LLS Rowiak GmbH (Hannover, Germany). A summary of the number of explants and time points of SRµCT and TXM study are in Table 3.2. The explants were prepared and preserved using the protocol described in Chapter 3.1.4.

Table 3.2: Number of explants investigated via SRµCT and TXM

	SRµCT			TXM	
Time point (Weeks)	4	8	12	10	20
Mg-10Gd	5	5	5	4	5
Ti	5	5	5	4	5

3.2.3 Image acquisition and analysis for SRµCT experiment

SRµCT image acquisition

For this experiment, the explants from the animal experiment that were obtained at 4, 8 and 12 weeks were used. The explants were imaged at the P05 imaging beamline IBL of the PETRA III storage ring at the Deutsches Elektronen Synchrotron (DESY), which is operated by Helmholtz Zentrum Hereon, Hamburg, Germany[195,240]. The samples were scanned in absorption contrast mode at an energy of 25 keV at a stepwise rotation using a double multilayer layer monochromator (DDM) with a horizontal and vertical beam profile of 6.5 mm and 7 mm. The number of projections was 1200. The effective pixel size of the resulting tomograms was 1.25 µm but was binned to 2.5 µm with a binning factor of two. The tomographic reconstruction pipeline at the IBL[242] was implemented in MATLAB to reconstruct the tomograms based on the filtered back projection (FBP) algorithm using the ASTRA back projection toolbox[246,247]. The resulting image data were resampled to 5 µm voxel size and subsequently analyzed.

SRµCT image processing

Tomographic datasets require comprehensive processing prior to quantitative analysis. First, the image data were automatically segmented into bone tissue and the implant screws using a U-net convolutional neural network (CNN)[248] that was developed by Moosmann *et al.* since manual segmentation is time consuming. The details of the image processing and the segmentation to generate bone and screw labels are found in reference[14]. The bone and screw labels were further processed and analysed in this work using both Avizo (Version 2021.1, Thermo Fisher Scientific, Waltham, USA) and MATLAB (Version 2021a, MathWorks, Massachusetts, United States). Segmentation of the bone microporosity involved several steps and was based on the segmentation method of Nunez *et al.*[249]. The segmentation protocol majorly combined morphological and Boolean operations that were available in Avizo (Version 2021.1, Thermo Fisher Scientific, Waltham, USA). First, the bone labels were cleaned using a 3D opening operation. In the second step, interactive thresholding was performed to segment the bone porosity. To remove the clustered pixels that should be a part of the background but were incorrectly identified as bone porosity, a third step was performed to generate a bone mask. This involved performing a 3D closing operation on the clean bone to fill or close the bone porosity. Then, the bone porosity label obtained from the second step was combined with the solid bone mask in an 'AND' logical operation resulting in a data set containing only the bone porosity excluding the background. Finally, the lacunar porosity was separated from the vascular porosity via component labelling. The vascular porosity was then skeletonized. Skeletonization extracts the centrelines of filamentous structures from image data and was originally designed to analyse vascular structures[250]. The skeletonization module extracts the centrelines by first calculating the 3D distance map of the image followed by thinning to remove non-connected pixels such that finally a string of connected voxels remains. The resulting datasets were then exported to MATLAB (R2021b MathWorks, Inc., Massachusetts, USA) for quantitative analysis. The description of the segmentation workflow and the labels generated are presented as a process chart flow in figure 3.3 and figure 3.4 respectively.

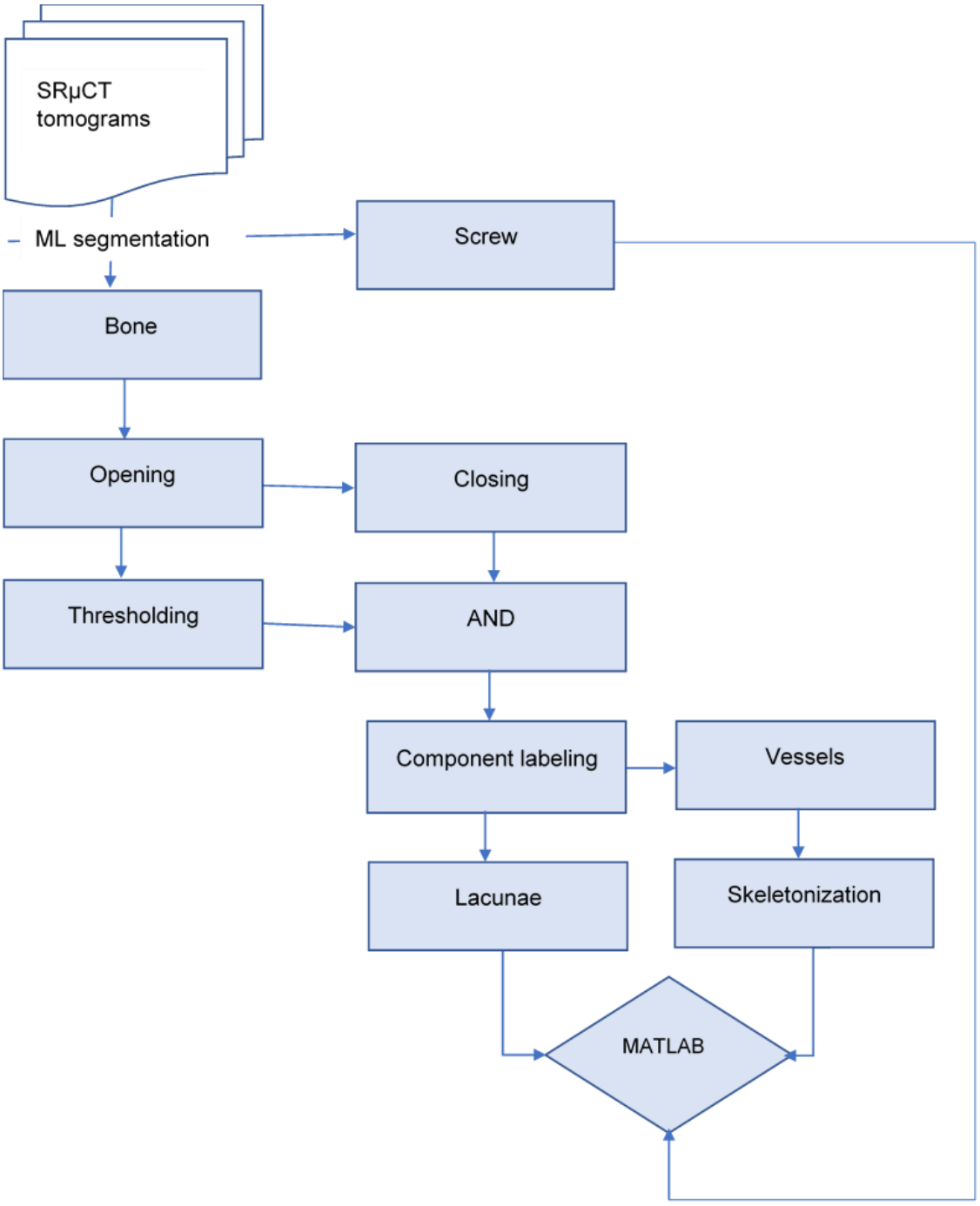

Figure 3.3: SRμCT image processing flow chart

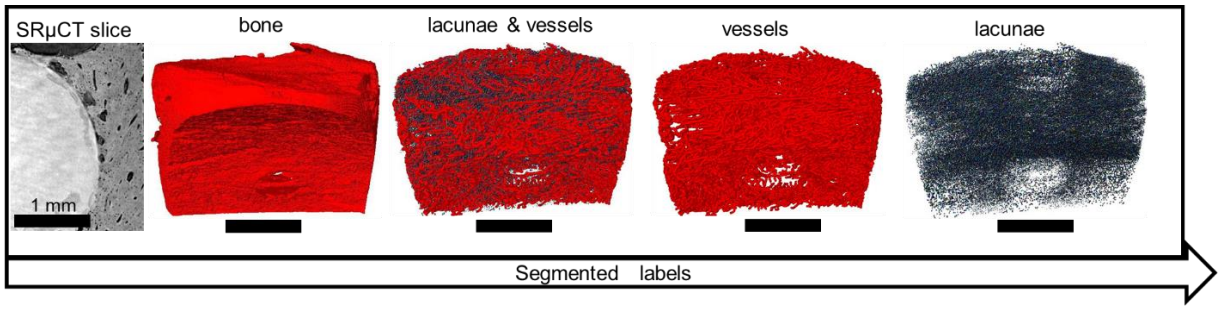

Figure 3.4: Segmented labels of SRμCT data into osteocyte lacunae and vascular porosities. From Sefa *et al.*[19]. Published under the Creative Commons CC-BY 4.0 Licence.

SRμCT quantitative analysis

To understand the local and global effect of the Mg-10Gd degradation on the interfacial bone porosity, all quantified parameters were obtained within a 200 μm^3 and 500 μm^3 volume of interest (VOI) respectively from the screw. Since the depth of the M2 screws was 250 μm, VOI 200 μm (local) represents the region between the screw thread and screw tips while VOI 500 μm^3 (global) represents the local region (200 μm^3) plus an additional 300 μm^3 region from the screw. The 200 μm^3 VOI was generated by dilating the screw 40 times while the 500 μm^3 was generated 100 times. The quantified parameters were defined as: vascular number density (N.Vs) and lacunar number density (N.Lc). All quantified parameters were normalized by the total bone volume (BV) which was calculated using equation 3. Lacunar and vascular number density were calculated as the total number of labelled objects normalized by BV (equation 4).

$$Total\ Bone\ volume = Sum\ of\ voxels\ within\ bone\ mask\ \times voxel\ size\ cubed \quad (3)$$

$$Lacuna/vascular\ number\ density = \frac{Number\ of\ lacunae\ or\ vessels}{BV} \quad (4)$$

3.2.4 Image acquisition and analysis for TXM experiment

Scanning electron microscopy (SEM) image processing and analysis

To appropriately select regions of interests (ROIs) for TXM measurement and to obtain 2D quantified vascular and lacunar porosity, SEM imaging was performed prior to the TXM measurement. For this, the embedded explants were cut into two halves using a diamond saw (Well Diamond Wire Saws SA, Mannheim, Germany) to expose the bone and the implanted screws. The samples were then cleaned with ethanol and polished using a Diamond suspension (particle size 3 μm) for 7 minutes and viewed under a light microscope to ascertain effective polishing. The polished samples were sputtered with gold for a minute using Cressington sputter coater (TESCAN GmbH, Dortmund, Germany). Afterwards, the samples were scanned using TESCAN AMBER X (TESCAN GmbH, Dortmund, Germany) SEM with a current of 10 pA and a voltage of 10 kV. This yielded images with a pixel size of 0.195 μm.

To bridge the gap between nano- and micro-scale (i.e SRμCT and TXM experiment), the lacunar and vascular number density were also quantified for the 2D SEM image datasets. The image processing and analysis were performed in Avizo (Version 2021.1, Thermo Fisher Scientific, Waltham, USA) and Fiji/ImageJ. Similar to the 3D analysis of the SRμCT study, the lacunar and vascular number density were quantified within a 200 μm^2 and 500 μm^2 area of interests (AOIs). First, the image data were manually segmented in Fiji/ImageJ to separate the bone and the screw. The screw was then dilated by 1024 and 2560 times to obtain 200 μm and 500 μm AOI labels respectively. The dilated screw was combined with the bone label in a Boolean logical 'AND' operation resulting in a label that contained only the bone in the specified AOI. Afterwards, the manual counting was performed to determine the bone porosity. Both the lacunar and vascular porosity were normalized by the bone area (BA) which was calculated as the sum of pixels multiplied by pixel size squared to obtain the lacunar number density (N.Lc/BA) and vascular number density (N.Vs/BA) respectively.

Sample Preparation for TXM specimens

From the SEM image data, two ROIs were defined for each sample of each implant material per time point: one from the cortical region of the bone implant interface (peri-implant bone within cortical bone) (figure 3.5 panel IC) and one from the trabecular region (peri-implant bone

adjacent the intramedullary cavity) (figure 3.5 panel IB) in order to obtain representative samples across the bone. Bone specimens were also cut from bone in Ti samples far from the implantation area to serve as an additional control (figure 3.5 panel IA). The ROIs were then cut using focused ion beam (FIB) milling (Fraunhofer-Institut für Integrierte Syteme und Bauelementetechnologie (IISB)). The FIB cutting generated 45 bone specimen pillars (Table 3.3) with a diameter of 50 µm and a height of 50 µm mounted on custom made pins (figure 3.5 panel ID).

Table 3.3: Bone specimens used for TXM investigation

	Cortical bone		Trabecular bone	
Time Point (Weeks)	10	20	10	20
Mg-10Gd	4	5	4	5
Ti	4	5	4	5
Control	4	5	-	-

TXM image acquisition

The bone pillars were imaged using full-field TXM. The image data acquisition was acquired at the P05 nanotomography endstation at Petra III, DESY, which is operated by Hemholtz-Zentrum Hereon. The imaging was performed using a monochromatic beam with an energy of 11.1 keV which was selected using a Si(111) double crystal monochromator ($\Delta E/E \sim 10^{-4}$). The illumination of the bone specimens was performed using a beam shaping condenser with square fields and a Frensel zone plate objective lens with an outermost zone width of *dr* = 50 nm. To achieve phase contrast, Zernike phase rings were placed in the back focal plane of the Fresnel zone plate. Paul-Scherrer-Institut (Switzerland) X-ray Optics and Applications group designed and fabricated all the optics. A Hamamatsu C12849-101U camera with a sCMOS chip with 6.5 µm physical pixel size and a 10 µm Gadox scintillation layer was used. The high resolution scanning generated 3D images with 22.8 nm voxel size. The raw image data were reconstructed using a TomoPy reconstruction pipeline at the imaging beamline[251] with a binning factor of two resulting in a voxel size of 45.6 nm.

TXM image processing

Similar to the SRµCT data, the TXM tomographic images required processing to be denoised and segmented prior to quantitative analysis. For this, the high-resolution image data were first filtered using an iterative non-local mean filter to remove textural noise[243] caused by back projection during image data acquisition, followed by segmentation in Avizo (Version 2021.1, Thermo Fisher Scientific, Waltham, USA). Segmentation involved a combination of interactive thresholding and morphological operations to separate the LCN from the extracellular matrix (ECM) as well as to separate the lacunae and canaliculi. First, the bone was manually segmented using the Auto Trace tool in Avizo. To separate the LCN (figure 3.5 panel II) from the ECM, interactive thresholding was employed followed by manual correction. To extract the lacunae (figure 3.5 panel II) from the LCN, an opening operation was performed to remove the canaliculi retaining only the lacunae. To extract the canaliculi (figure 3.5 panel II) from the LCN, the lacunae were inverted and combined with the LCN using a Boolean ‘AND’ operation. The outlined segmentation steps are presented as a process chart in figure 3.6.

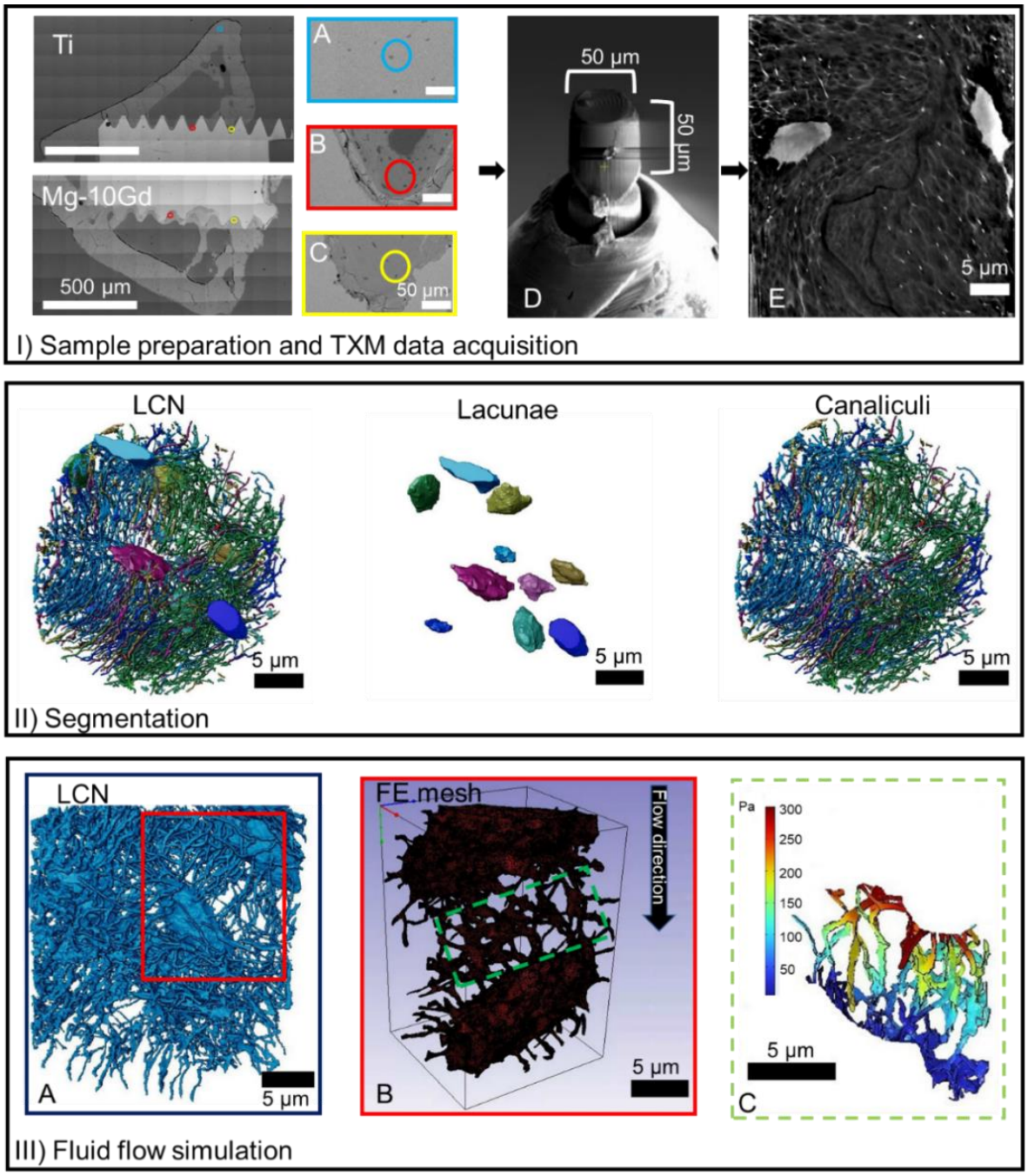

Figure 3.5: Sample preparation steps for TXM image data acquisition and finite element modelling. (Panel IA) – (Panel IC) SEM slice showing the selection of ROIs. (Panel IA) ROI fom control region; (Panel IB) ROI from cortical region, (Panel IC) ROI from trabecular region, (Panel ID) cut ROI, (Panel IE) example slice through 3D TXM image data. (Panel IIA) - (Panel IIC) segmented TXM image data into LCN, consisting of lacunae and canaliculi. (Panel IIIA) – (Panel IIIC) finite element simulation of the selected lacunae pair; (Panel IIIA) selection of lacunae pair, (Panel IIIB) meshing of lacunae pair, (IIIC) selected ROI for quantitative analysis. From Sefa *et al.*[19]. Published under the Creative Commons CC-BY 4.0 Licence.

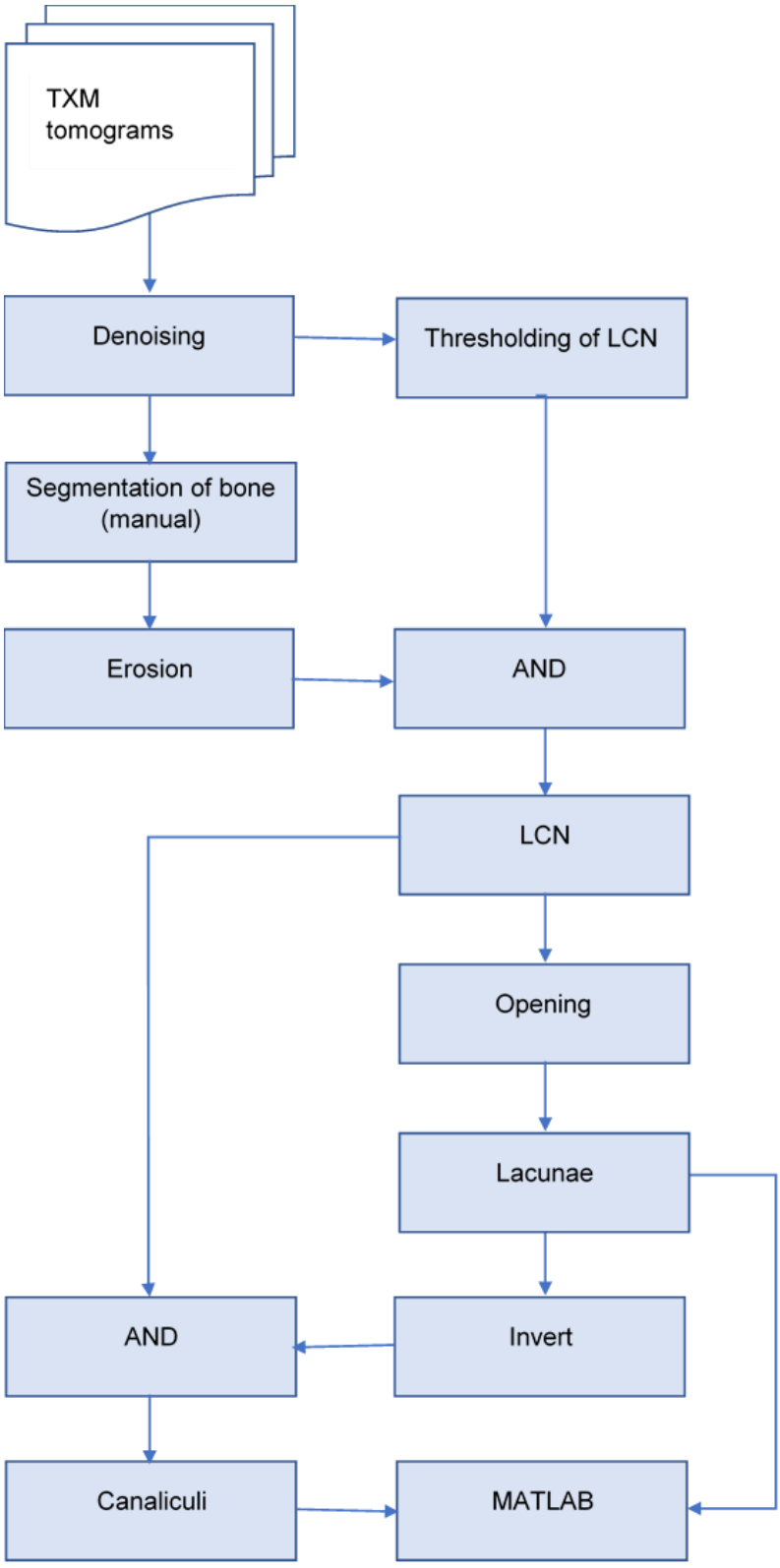

Figure 3.6: TXM image processing flow chart

TXM quantitative analysis

Quantification of lacunar descriptors & canaliculi descriptors

Quantification of the lacunae and canaliculi morphological descriptors were performed using the label analysis module Avizo (Version 2021.1, Thermo Fisher Scientific, Waltham, USA). Quantified parameters include:

Lacunae and canaliculi size

The size of the lacunar and canaliculi are constituted by their volume and surface area and were calculated using their respective image labels generated after segmentation. The average surface area of both lacunae (Lc.SA) and canaliculi (Ca.SA) was calculated as the area of the labelled object's boundaries within the image labels by modifying equation 6 to include the "intercepts" in order to consider the exposed surface of the outer voxels. The average volume of the lacunae (Lc.V), canaliculi (Ca.V) and total bone (BV) were calculated (using their respective labels) as the sum of voxels multiplied by the voxel size cubed (equation 7). Furthermore, the total volume of the LCN porosity (LCN/BV) was calculated using equation 7 and then normalized by the BV. Furthermore, the canaliculi junction density was quantified as the total number of canaliculi nodes normalized by BV (Ca.nodes/BV) using the auto skeleton module in Avizo (Version 2021.1, Thermo Fisher Scientific, Waltham, USA). Also, the number of canaliculi per lacunar surface area was quantified as the total number of canaliculi normalized by the lacunar surface area.

$$Surface\ area = \int_{\delta x}^{\delta x} \sqrt{x^2 + y^2 + z^2 dt} \tag{6}$$

Where *x(t), y(t)* and *z(t)* are parametric representations of the boundary curve of a labelled image.

$$Volume = Sum\ of\ voxels\ \times (Cx \times Cy\ \times Cz) \tag{7}$$

Lacunae shape

The shape characteristics of the lacunae were calculated using equation 8 and the second order moment of inertia since the shape of the lacunae is generally assumed to be ellipsoidal[252]. The second order moment of inertia is used to find the lengths and orientations of the axis of the best fitting ellipsoid. The inertial matrix is given by equation 9.

$$Sphericity = \frac{\pi^{\frac{1}{3}}(6 \times Volume)^{\frac{2}{3}}}{Surface\ area} \tag{8}$$

$$M_{inertia} = I\ \times tr(M_{cov}) - M_{cov} \tag{9}$$

Where *I* is the identity matrix, *tr* is the transformation and M_{cov} is the covariance matrix given by equation 10.

$$M_{cov} = \begin{bmatrix} M_{2x}\ M_{2xy}\ M_{2xz} \\ M_{2xy}\ M_{2y}\ M_{2yz} \\ M_{2xz}\ M_{2yz}\ M_{2z} \end{bmatrix} \tag{10}$$

From equation 10, the three eigenvalues $\lambda_1 \geq \lambda_2 \geq \lambda_3$ were obtained. Then, the anisotropy, which measures the deviation from a spherical shape, was calculated using equation 11.

$$Anisotropy = 1 - \lambda_1 \tag{11}$$

Distance distribution of lacunae and canaliculi

To explore the spatial arrangement of the lacunae and their osteocyte canaliculi within the bone matrix, their distance maps, which depict the distance of the bone matrix from the nearest lacunae and canaliculi were calculated[252,253] in MATLAB (R2021b MathWorks, Inc., Massachusetts, USA). For this, the 3D distance maps of the lacunae and canaliculi were first calculated. In the second step, the normalized cumulative histogram of the distance maps was calculated. The values which correspond to 50 % of the distribution denoted as $Lc.Dist_{50}$ and $Ca.Dist_{50}$ were determined for lacunae and canaliculi respectively. The resulting values

indicate that 50 % of the bone matrix can be found within a distance $Lc.Dist_{50}$ from the nearest lacunae and $Ca.Dist_{50}$ from the nearest canaliculi respectively.

3.4.5 Image-based computational fluid dynamics analysis

Model Generation

To further understand the impact of degradable Mg-10Gd implants on the functionality of the LCN, image-based fluid flow simulations were performed in COMSOL Multiphysics (version 6.0, COMSOL AB, Stockholm, Sweden). To this aim, a sub volume consisting of a pair of osteocyte lacunae with their connected canaliculi were extracted from the segmented LCN of each bone specimen for both Mg-10Gd, Ti and the control bone specimens. The extracted sub-volumes (lacunar pairs) (figure 3.5 panel IIIA) were modelled to represent the 'basic unit' of the LCN within which cellular communication occurs. The lacunar pairs were meshed (figure 3.5 panel IIIB) using Simpleware ScanIP (version P-2019.09, synopsis, North Carolina, United States) voxel-meshing software to create tetrahedral elements. The meshed lacunar pairs were then exported to COMSOL Multiphysics (version 6.0, COMSOLAB, Stockholm, Sweden) for the fluid flow simulation implementation.

Fluid flow simulation

The fluid flow simulation used in this study was adapted from that which was utilized here[224,254]. Darcy's Law[254] (equation 12), which governs the flow of fluid within a porous media, was employed to investigate the pressure and velocity distributions of interstitial fluid flow within the osteocyte LCN pair. All the parameters used for the fluid flow simulations are summarized in table 3.4. During mechanical loading in bone, a pressure gradient is generated from the compression and tension which occur in different regions of the bone to drive fluid across the bone network[255–257]. This phenomenon was incorporated into the model by applying a pressure gradient across the model. Thus, an inlet pressure of 300 Pa was assigned to the inlet on one face and the opposite face was assigned an outlet pressure of 0 Pa in the flow direction[255–257]. The remaining faces of the mesh were assigned symmetry boundary conditions. The resulting stationary fluid equations were solved and the average pressure and velocity were analyzed for the canaliculi that connects the lacunar pair (figure 3.5 panel IIIC). To this end, the connected canaliculi were segmented from the lacunar pair and multiplied with the pressure and velocity matrix obtained from the solution to the fluid flow equations in MATLAB (R2021b MathWorks, Inc., Massachusetts, USA). To account for differences in the volume of the analyzed region, the average pressure and velocity were further normalized by the total volume of the connecting canaliculi.

$$u = -\frac{k}{\mu}\nabla p \qquad (12)$$

where u is Darcy's velocity, k is the permeability of the porous media, μ is the fluid's dynamic viscosity and ∇p is the load induced fluid pressure gradient.

Table 3.4: Parameters used for finite element modelling

Parameter	Value	Unit
Permeability[254]	10^{-18}	m^2
Porosity[254]	5	%
Density of salt water[230]	997	kg m^{-3}
Dynamic viscosity[258]	0.000855	kg $m^{-1}s^{-1}$

Statistical analysis

All statistical analysis was performed in Origin 2021b (OriginLab, Northampton, Massachusetts, USA). The normality of the data was first evaluated using Shapiro Wilk normality test. Using one-way analysis of variance (AVOVA), the means of all 2D and 3D quantified parameters were evaluated between each material and time point. Also, to quantitatively evaluate the impact of Mg-10Gd on the specific bone types, group means were tested between the trabecular and cortical bone specimens. To explicitly determine the significance of the parameters among the groups, a post hoc analysis for pairwise comparison among means was performed using Tukey's honestly significant difference (HSD) tests. A significance level of $p < 0.05$ was considered significant.

Chapter 4

Results

Study I: Assessing the long-term *in vivo* degradation behavior of Mg-10Gd, Mg-4Y-3RE and Mg-2Ag.

The results obtained from **Study I** have been published[18] hence this section is copied from the publication.

4.1.1 Qualitative evaluation of osseointegration

"All screw types were altered in their original shape and density. In figure 4.1, 2D SRμCT slices of each screw type after 6 and 9 months of implantation show that Mg-10Gd and Mg-4Y-3RE had retained the original threaded screw shape, whereas Mg-2Ag had a distorted shape. This observation is also corroborated by the 3D rendering of the screws shown in figure 4.2. Interestingly, even though the degradation products of Mg-2Ag appear to be severely disintegrated, they remained attached to the bone, as seen in the inset of figure 4.1. The X-ray absorption coefficient between the degradation layer and residual screw was similar and could not be distinguished in the SRμCT image data (figure 4.1) thus, the degradation rate could not be calculated. Nonetheless, representative 2D histological slides show that almost all the original metal had transformed in degradation products. For Mg-10Gd and Mg-4Y-3RE, the degradation products remained attached to the original metal, maintaining the original threaded shape. For Mg-2Ag, part of the degradation layers was still attached to a core of residual original metal, but had not maintained the same original shape. For all three materials, a core of residual screws was visible at 6 months in the histology (figure 4.3, red arrows). The histological slides further reveal that the metallic residue in Mg-10Gd (figure 4.3) and Mg-4Y-3RE (figure 4.3) have a similar dark appearance compared to Mg-2Ag (figure 4.3), which appeared dark brown. The SRμCT slice of Mg-10Gd (figure 4.1) and Mg-4Y-3RE (figure 4.1) show the presence of high intensity structures. These high intensity structures seen in Mg-4Y-3RE can also be observed in their corresponding histological data (figure 4.3) but in the case of Mg-10Gd, the high intensity areas are not noticeable in their corresponding histological data (figure 4.3). The insets in (figure 4.1) and (figure 4.3) both highlight the bonding between the degradation layer and the bone of all screw types.

From the observations, the bone tissue response to the Mg screws appeared similar at both implantation times. At the end of the two implantation times (6 and 9 months) and for all screw types, the osteotomy gap had been completely bridged and the screws were fully integrated into the surrounding bone. Figure 4.1 and figure 4.3 show the intimate contact among all the screw types with the bone environs. All screw types appear to be surrounded by healthy bone due to the presence of osteocytes in the bone around the screws (figure 4.3).

Figure 4.4 shows representative constituent maps of the three Mg alloy types that were characterized using μXRF at 9 months implantation time. Small amount of residual metal was present in all screw types which can be deduced from the map showing the distribution of Mg. Therefore, it is obvious that the other part of the screw has turned into degradation layer. The degradation products of Mg-10Gd and Mg-4Y-3RE maintained their original screw shapes while the degradation products of Mg-2Ag appear distorted. As expected, Gd signal was detected in Mg-10Gd alloys. The alloy Mg-4Y-3RE clearly showed a Y signal in the degradation layer while Mg-2Ag had silver (Ag) signal in the degradation layer. Calcium (Ca) and phosphorus (P) signals were detected in the degradation layer of all screw types. Also, for all

screw types, sulfur (S) signals were detected in the degradation layer and surrounding soft tissue. The enrichment of S at the site of Mg-2Ag implant indicates the strong association of proteins to Ag[259,260]".

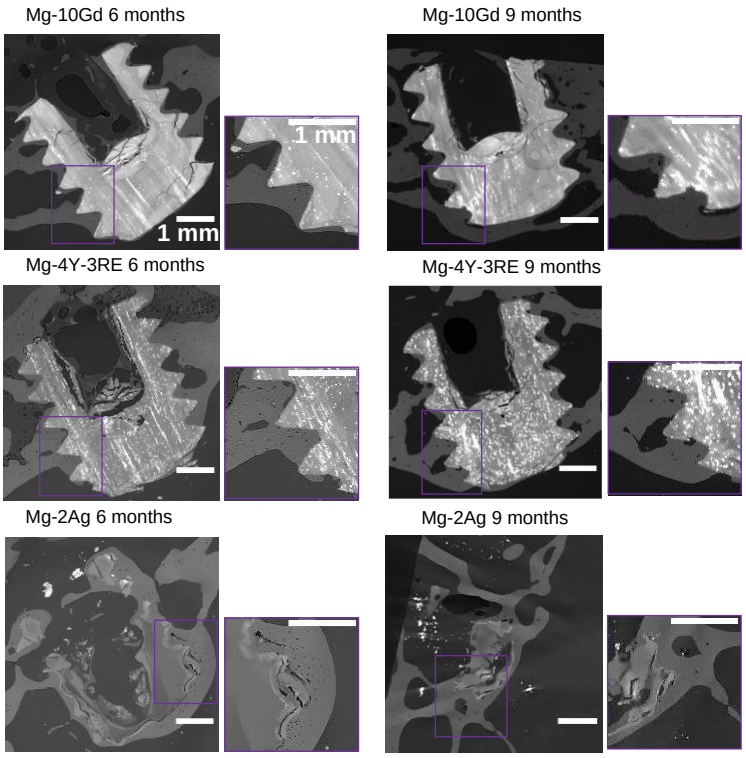

Figure 4.1 2D longitudinal slices of a SRµCT scan of three Mg-based screws after 6 and 9 months of implantation showing the encapsulation among all the screw types in the surrounding bone. The image shows good osseointegration involving all the screw types. The insets highlight the bonding between the degradation layer and bone of all screw types. Notably, Mg-2Ag bonded to the bone despite severe disintegration. From Sefa *et al.*[18]. Published under the Creative Commons CC-BY 4.0 Licence.

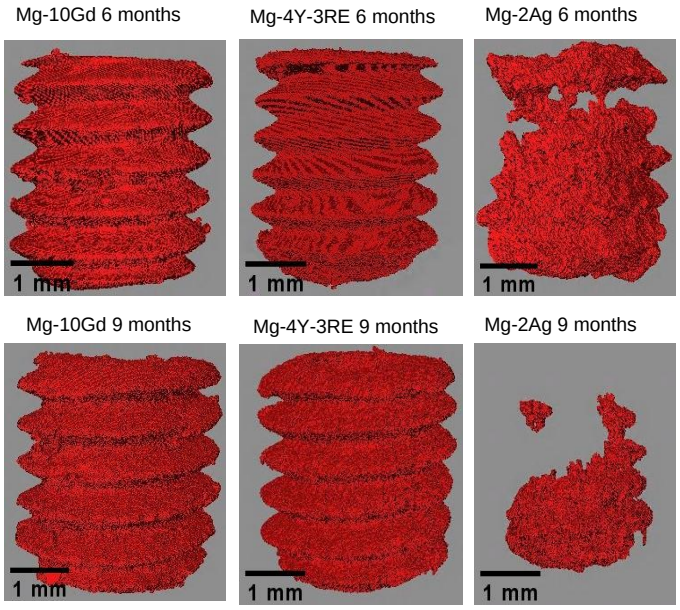

Figure 4.2: 3D rendering of a SRµCT scan of three Mg-based screws showing their appearance after 6- and 9-months implantation time. The image shows visible alteration in the geometry of Mg-2Ag, whereas the Mg-10Gd and Mg-4Y-3RE maintained the original threaded screw shape after degradation. From Sefa *et al.*[18]. Published under the Creative Commons CC-BY 4.0 Licence.

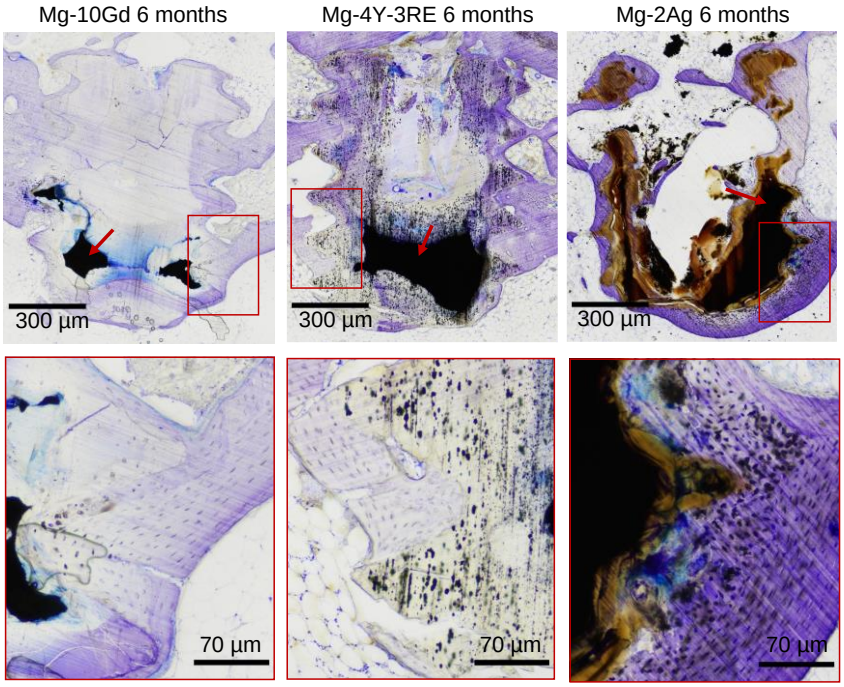

Figure 4.3 2D histological slides of Mg-10Gd, Mg-4Y-3RE and Mg-2Ag stained with toluidine blue after 6 months of implantation. Residual metal (red arrows) shown as black areas can be seen for all screw types. From Sefa *et al.*[18]. Published under the Creative Commons CC-BY 4.0 Licence.

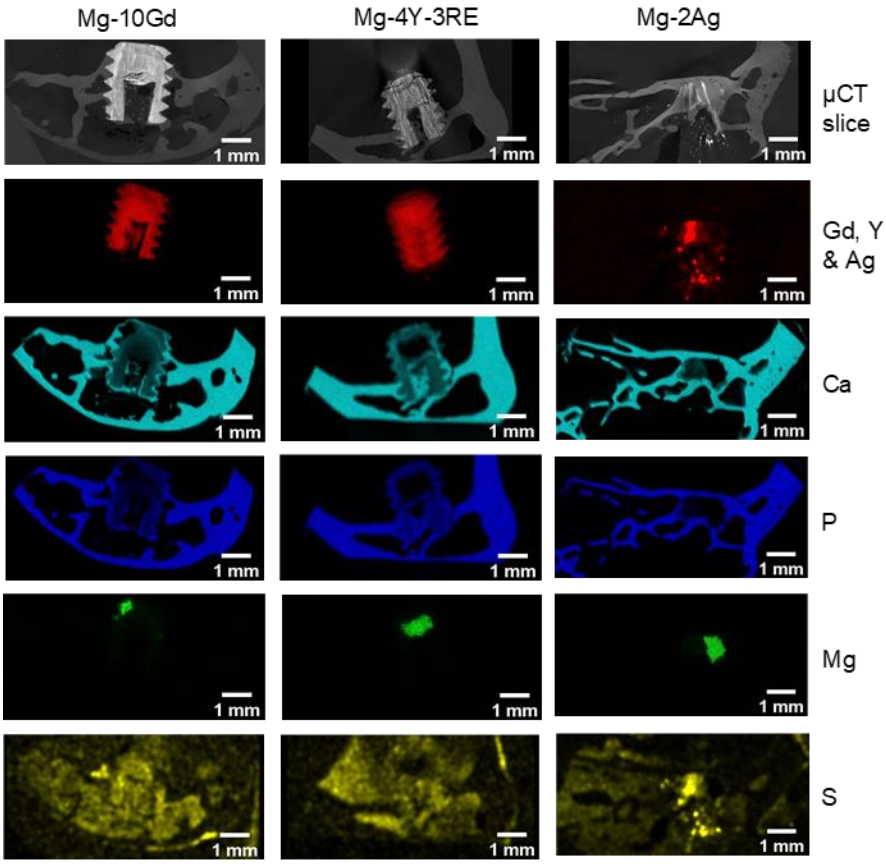

Figure 4.4: Exemplary µXRF maps of Mg-10Gd, Mg-4R-3RE and Mg-2Ag screws after 9 months of implantation. From Sefa *et al.*[18]. Published under the Creative Commons CC-BY 4.0 Licence.

4.1.2 Quantitative evaluation of osseointegration

The following results have been published in this publication[18]

The quantitative evaluation of osseointegration was based on the SRµCT image data evaluated within a distance of 300 µm from the implant. The evaluated parameters are all presented in figure 4.5 as box plots and the descriptive statistics summarized in table 1A and table 1B in Appendix A. From figure 4.5A&B it is apparent that the BV/TV and BIC among the screw types did not significantly differ at both 6 and 9 months. Mg-10Gd presented higher mean BV/TV compared to Mg-2Ag and Mg-4Y-3RE at 6 months but slightly declined at 9 months. For BIC, Mg-10Gd presented higher mean BIC compared to Mg-2Ag and Mg-4Y-3RE at both 9 and 6 months. Mg-2Ag had significally lower remnant screw volumes compared to Mg-10Gd and Mg-2Ag at both 6 and 9 months. The initial screw volumes prior to implantation did not significantly differ. Result of the effect of pre-incubating the screws prior to implantation is displayed as scatter plots (figure 4.5E&F) and the descriptive statistics summarized in table 1C in Appendix A. For Mg-10Gd and Mg-4Y-3RE, the blood pre-incubated screws did not yield BV/TV and BIC that was significantly different from the control group. Contrary for Mg-2Ag, higher mean BIC was recorded for the the blood pre-incubated group compared to the control group at 6 and 9 months respectively.

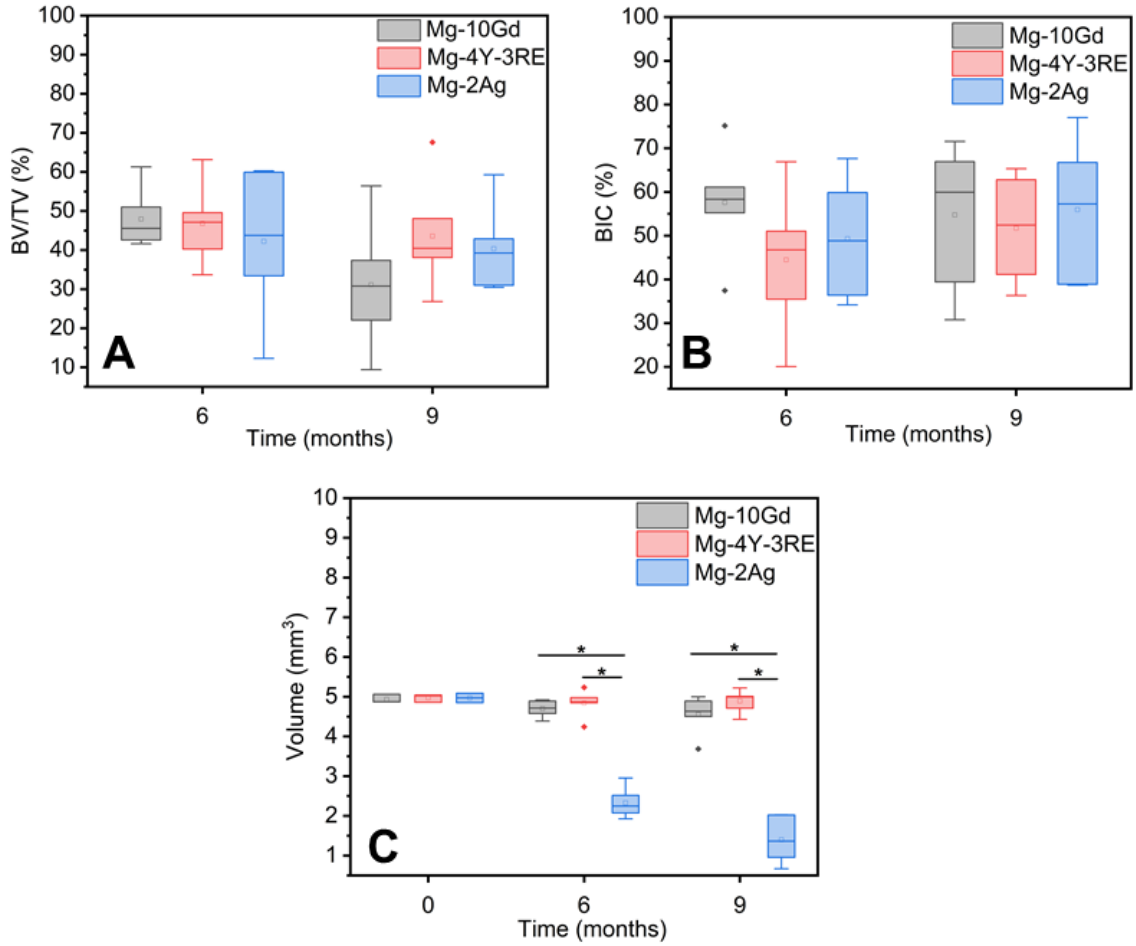

Figure 4.5: (A – C) Box plots of the results of bone volume fraction (BV/TV), bone implant contact (BIC) and volume of the screws calculated from the tomograms. The initial screw volumes are at time point = 0. The median is represented by a horizontal line in the box. Within each boxplot, the small box represents the mean. The whiskers correspond to the range. * means the result is significant. Number n = 36; test: one-way ANOVA. Published under the Creative Commons CC-BY 4.0 Licence.

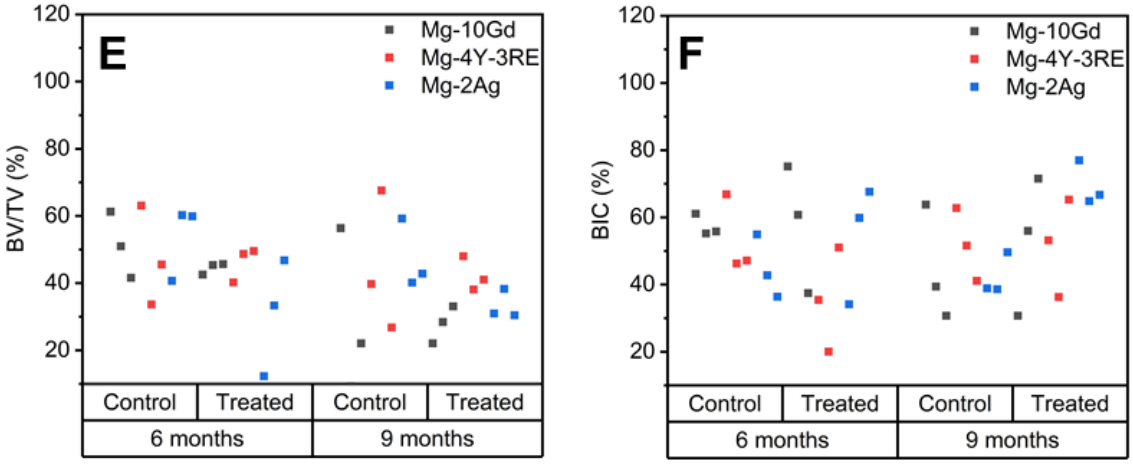

Figure 4.5: (E & F) scatter plots of the results of blood pre-incubation of the screws on bone volume fraction (BV/TV) (E) and bone implant contact (BIC) (F) between blood pre-incubated and control group of each material at 6 and 9 months. From Sefa *et al.*[18]. Published under the Creative Commons CC-BY 4.0 Licence.

Study II: To characterize the microstructural adaptation of bone around Mg-10Gd using multiscale imaging

In this section, the results of the SRµCT investigation, the TXM investigation and the fluid flow simulation are reported. Descriptive statistics to all parameters can be found in Appendix A. The following section is a paraphrase from the publication of **Study II**[19].

4.2.1 SRµCT investigation - Assessing the impact of Mg-10Gd degradation on vascular and lacunar porosity.

The local (distance 200 µm from the screw) and global distribution (distance 500 µm from the screw) of the vascular and lacunar porosity around Mg-10Gd and Ti at 8 weeks post-implantation are shown as 3D visualization in figure 4.6. In both local and global instances, the lacunar density around Mg-10Gd seemed sparsely distributed around the screws. However, there was no appreciable visual difference in the vascular distribution around both screw types in both globally and locally instance. Quantitatively, the lacunar number density was significantly higher around Ti in comparison to Mg-10Gd locally and globally at all time points (figure 4.7A-B). There was no significant difference in the vascular number locally and globally at all time points except at 8 weeks where Mg-10Gd had significantly higher vascular number density compared to Ti in the local instance (figure 4.7C-D). The descriptive statistics for the lacunar and vascular porosity distributions are summarized in table 2A&B in Appendix A.

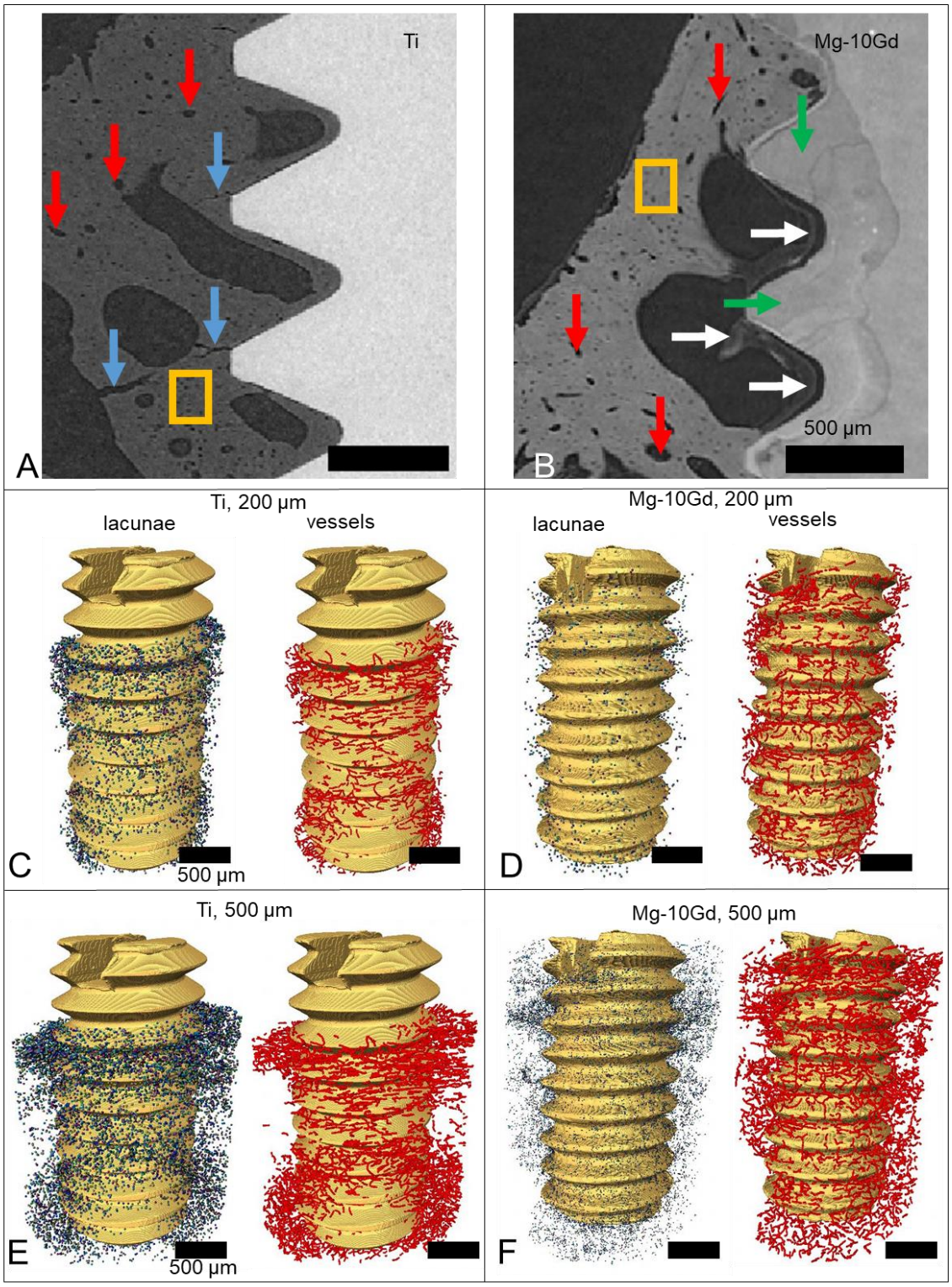

Figure 4.6: 2D and 3D visualization of the SRµCT data on bone microarchitecture within the interfacial bone of Mg-10Gd and Ti at 8 weeks post-implantaion. (A&B) are 2D slices showing the bone around Ti implant (A) and Mg-10Gd implant (B). The red arrows show vascular pores, yellow boxes show lacunae, blue arrows show cracks in the bone around Ti, white arrows show unmineralized bone regions around Mg-10Gd and green arrows show Mg-10Gd degradation layer. (C-F) were obtained at 8 weeks post-implantation 3D visualization of the lacunar (colored dots) and vascular distribution (red) locally and globally distributed around Mg-10Gd and Ti implant screws. The lacunar distribution around Ti appears denser than around Mg-10Gd. Adapted from Sefa *et. al.*[19]. Published under the Creative Commons CC-BY 4.0 Licence.

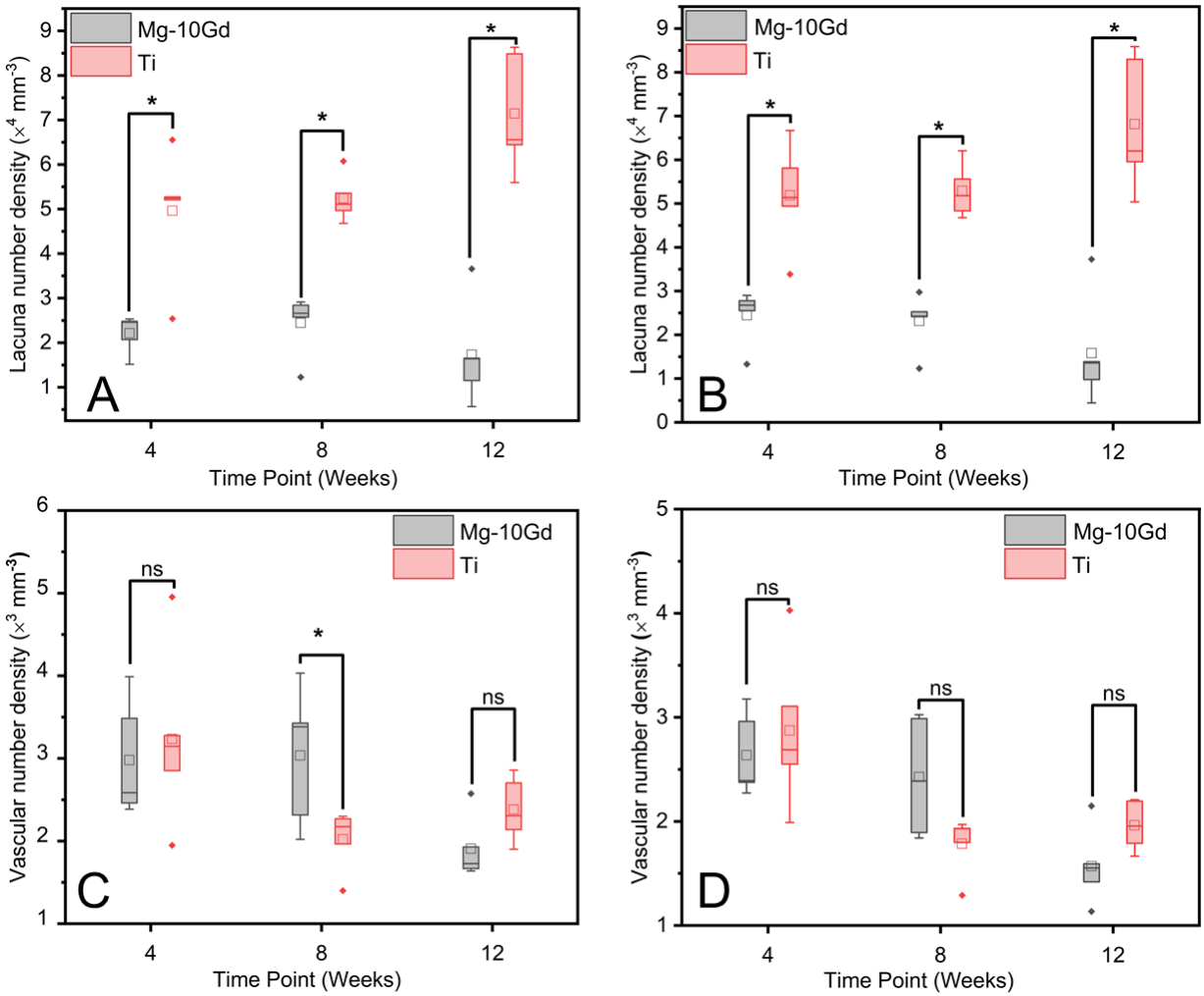

Figure 4.7: Boxplot of lacunar and vascular distributions around Mg-10Gd and Ti implant screws at 4, 8 and 12 weeks. (A) & (B) lacunar number density (distance 200 µm & 500 µm from screw). (E) & (F) vascular number density (distance 200 µm & 500 µm from screw). ns means not significant and * means significant. Within each boxplot, the horizontal line represents the median while the small box represents the mean. Adapted from Sefa *et.al.*[19]. Published under the Creative Commons CC-BY 4.0 Licence.

4.2.2 TXM study - Assessing the impact of Mg-10Gd degradation on the LCN

4.2.2.1 Lacunar and vascular distribution around Mg-10Gd and Ti - 2D assessment

To bridge the gap between the two length scales i.e. SRµCT and TXM, the local and global lacunar and vascular distributions were calculated from the SEM data. In contrast to the 3D analysis, there was no significant difference in lacunar number density between the two materials at 10 and 20 weeks post -implantation locally (distance 200 µm) (figure 4.8A). However, at 20 weeks, the lacunar number density was significantly higher for Ti compared to Mg-10Gd globally (distance 500 µm) (figure 4.8B). In both local and global instance, the vascular number density was not significantly different for Mg-10Gd and Ti at 10 and 20 weeks (figure 4.8C&D). The descriptive statistics for the 2D analysis of lacunar and vascular porosity distributions are summarized in table 2A&B in the Appendix A.

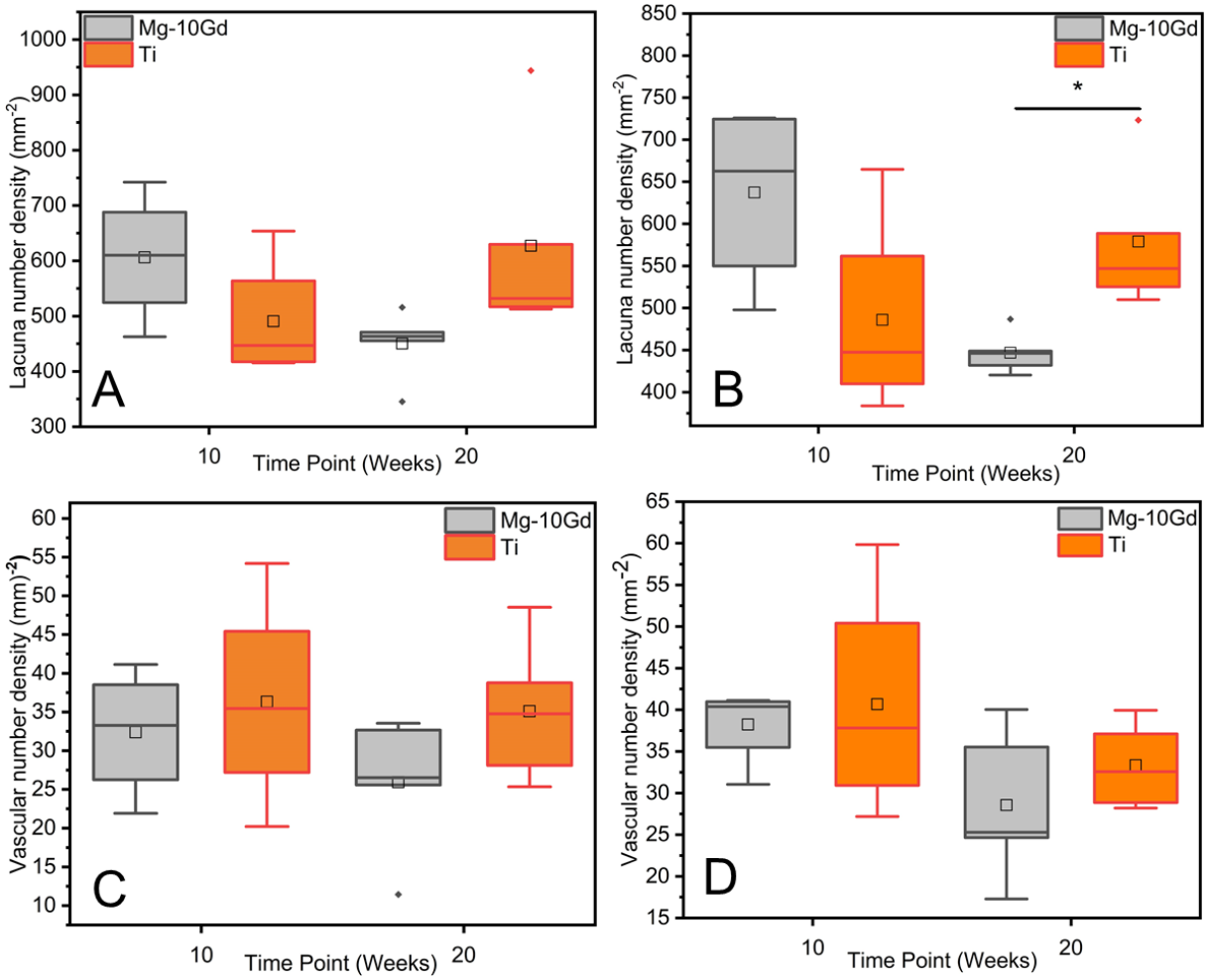

Figure 4.8: Boxplot of 2D lacunar and vascular density quantification for Mg-10Gd and Ti at 10 and 20 weeks. (A) & (B) lacunar number density local (distance 200 µm) and global (distance 500 µm) respectively. (C) & (D) vascular number density local and global respectively. ns means not significant and * means significant. Within each boxplot, the horizontal line represents the median while the small box represents the mean.

4.2.2.2 Qualitative evaluation of the LCN

By direct visualization of the LCN architecture in figure 4.9, it is apparent that the canaliculi attached directly to both Mg-10Gd and Ti implants but with a larger surface area at the point of attachment to the Mg-10Gd implants compared to that of Ti. At 20 weeks, there were no distinguishable differences in the architecture of canaliculi within the interfacial bone of both implants and rather appeared similar to that of the control. Moreover, there was no visible difference in the morphology of the lacunae around both implants, the long axis of the lacunae was oriented parallel to the screw thread around both Mg-10Gd and Ti implant screws.

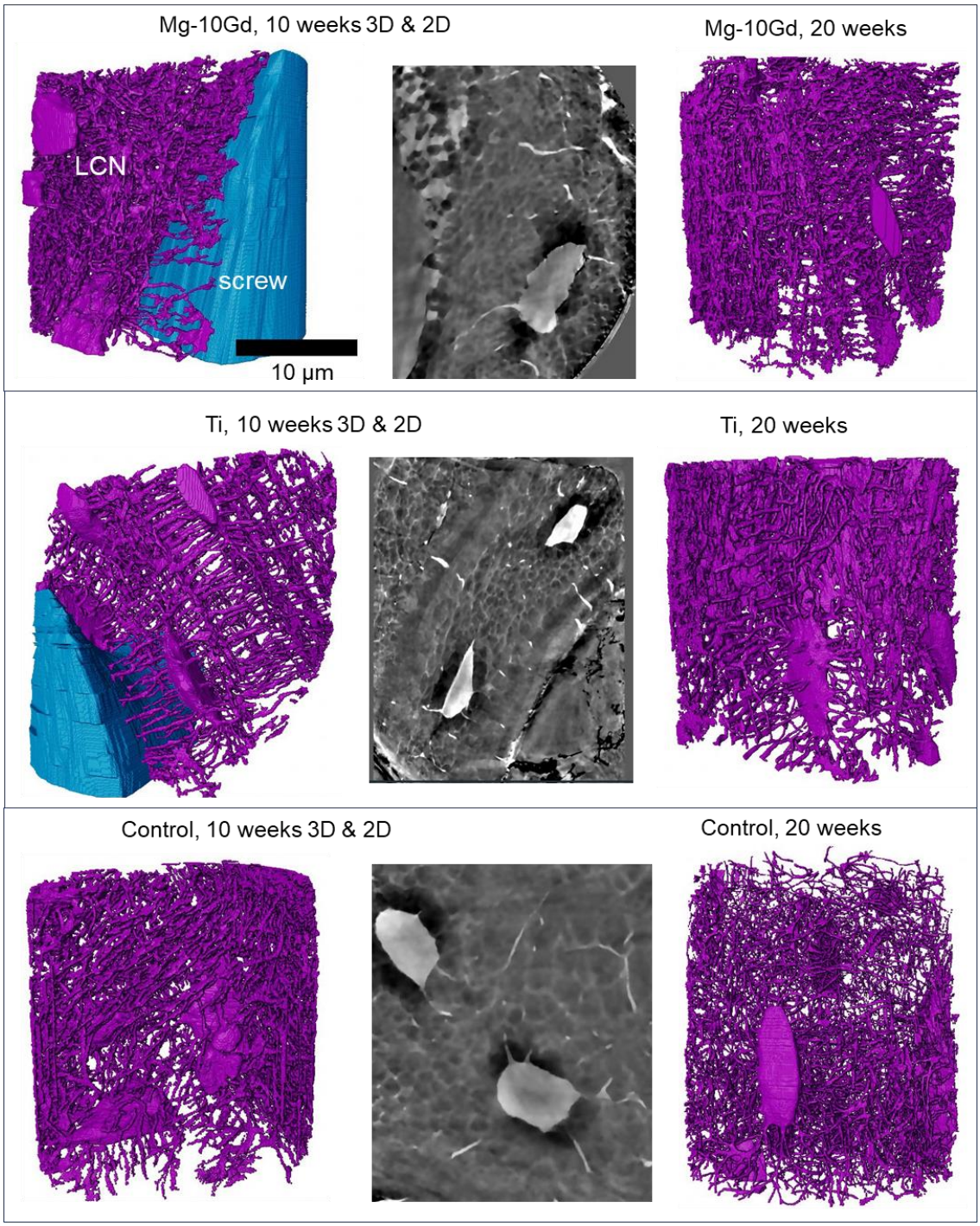

Figure 4.9: 3D rendering and 2D slice from the TXM image data showing the organization of the osteocyte LCN in the interfacial bone of Mg-10Gd, Ti and within the control bone specimens at 10 and 20 weeks.

4.2.2.3 LCN morphological descriptors

The lacunar morphological descriptors (volume, surface area and shape) are plotted as boxplots in figure 4.10A-D. Generally, the mean lacunar volume, surface area and the LCN porosity were higher for Mg-10Gd than for Ti and the control at 10 weeks but the order was reversed at 20 weeks with the lacunae around Ti having a higher mean volume, surface area and osteocyte LCN porosity (figure 4.10A-C). Furthermore, the mean lacunar volume, surface

area and LCN porosity continuously declined over time for Mg-10Gd and the control but not for Ti (Figure 4.10 A-C). The observed differences were not significant ($p > 0.05$). For the lacunar shape (Figure 4.10D), at 10 weeks, the highest sphericity index (0.71 ± 0.04) was associated with the lacunae of the control bone specimens followed by that of Mg-10Gd (0.67 ± 0.05) and finally that of Ti (0.65 ± 0.10). At 20 weeks, the highest sphericity index was recorded for the lacunae around Mg-10Gd (0.72 ± 0.05) followed by that of the control (0.70 ± 0.03) and finally Ti (0.69 ± 0.08). Regarding the anisotropy, at 10 weeks, the highest value was recorded for the lacunae around Mg-10Gd (0.90 ± 0.04), followed by that of Ti (0.89 ± 0.05) and finally that of the control (0.88 ± 0.05). At 20 weeks, Mg-10Gd and Ti had the same anisotropy values (0.87 ± 0.07) and (0.87 ± 0.10) respectively. That of the control bone specimens was (0.92 ± 0.03). The summary of the descriptive statistics can be found in table 3A&B in Appendix A.

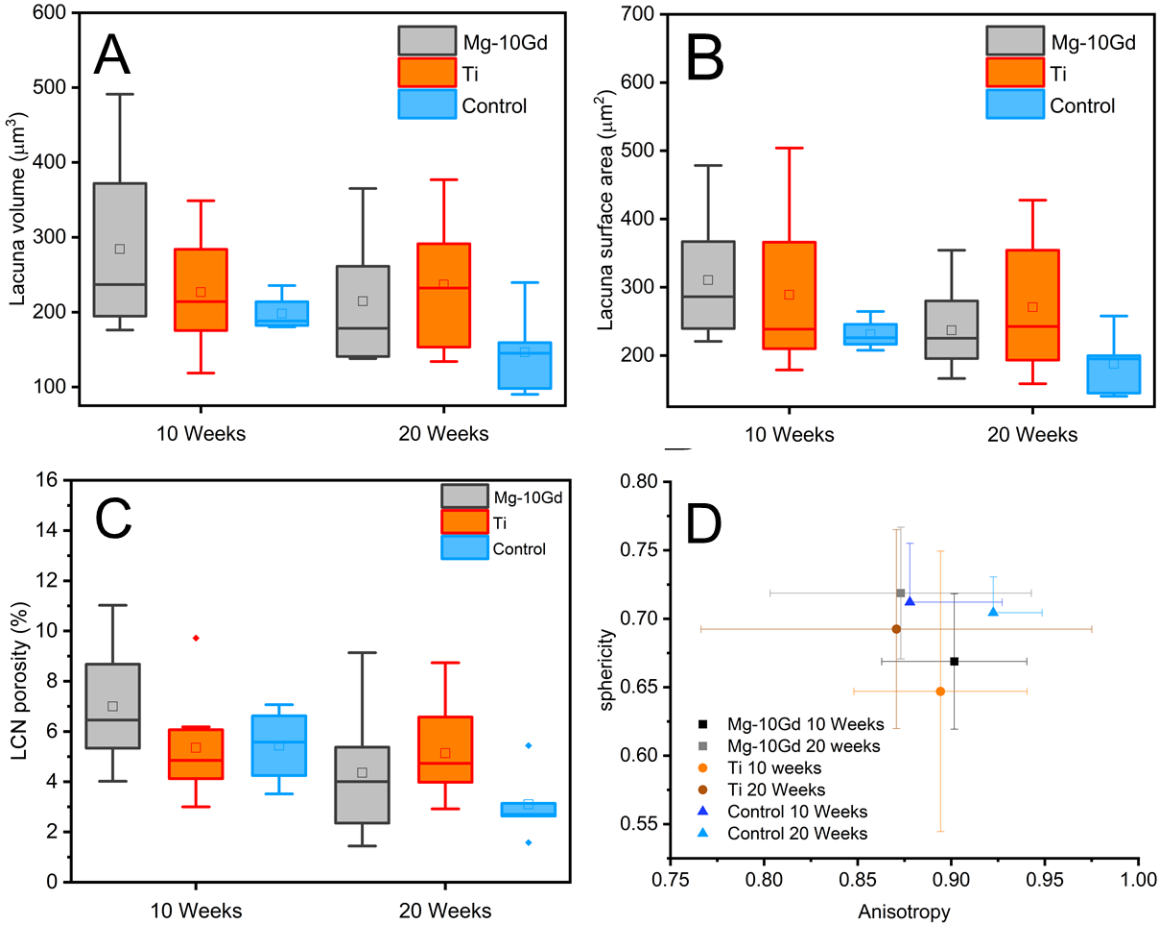

Figure 4.10: Boxplot of lacunar descriptors at 10 and 20 weeks post-implantation: (A) lacunar volume, (B) lacunar surface area, (C) LCN porosity and (D) lacunar shape descriptor. Within each boxplot, the horizontal line represents the median while the small box represents the mean. From Sefa *et. al.*[19]. Published under the Creative Commons CC-BY 4.0 Licence.

In figure 4.11A-D are the results of the canaliculi morphometric parameters calculated for Mg-10Gd, Ti and the control bone specimens at 10 and 20 weeks. Generally, higher mean canaliculi volume and surface area were recorded for Mg-10Gd than Ti and the control samples at 10 weeks but not at 20 weeks, the order was reversed with Ti showing highest values for the aforementioned parameters (figure 4.11A&B). The mean canaliculi junction density recorded did not significantly differ for Mg-10Gd ,Ti and the control specimens at both 10 and 20 weeks (Figure 4.11C). The canaliculi volume, surface area and junction density

descriptors did not reach the level of statistical significance ($p > 0.05$). Nonetheless, at 20 weeks, the mean number of canaliculi per lacunar surface area was significantly ($p < 0.05$) higher for Mg-10Gd in comparison to Ti but not the control (Figure 4.11D). At 10 weeks, the control samples had the highest mean number of canaliculi per lacunar surface area though not significantly ($p > 0.05$). The descriptive statistics are summarized in table 4A&B in the Appendix A.

The proximity of the bone matrix to the nearest lacunae and canaliculi was also calculated. At 20 weeks, highest Lc. $Dist_{50}$ distance (11.0 ± 3.21 µm) was recorded for Ti followed by Mg-10Gd (10.70 ± 2.54 µm) and finally the control (9.66 ± 1.18 µm). However, at 10 weeks, the control cohort had the highest Lc. $Dist_{50}$ (10.89 ± 2.26 µm) followed by Mg-10Gd (9.64 ± 2.3 µm) and Ti (9.17 ± 1.91 µm). Moving onto Ca. $Dist_{50}$, at 10 weeks, the following was recorded: (1.87 ± 0.58 µm), (1.72 ± 0.72 µm) and (1.08 ± 0.25 µm) for Ti, Mg-10Gd and the control bone specimens respectively. At 20 weeks, we obtained Ca. $Dist_{50}$ values of (1.29 ± 0.34 µm), (1.06 ± 0.20 µm) and (0.89 ± 0.09 µm) for Ti, Mg-10Gd and the control respectively.

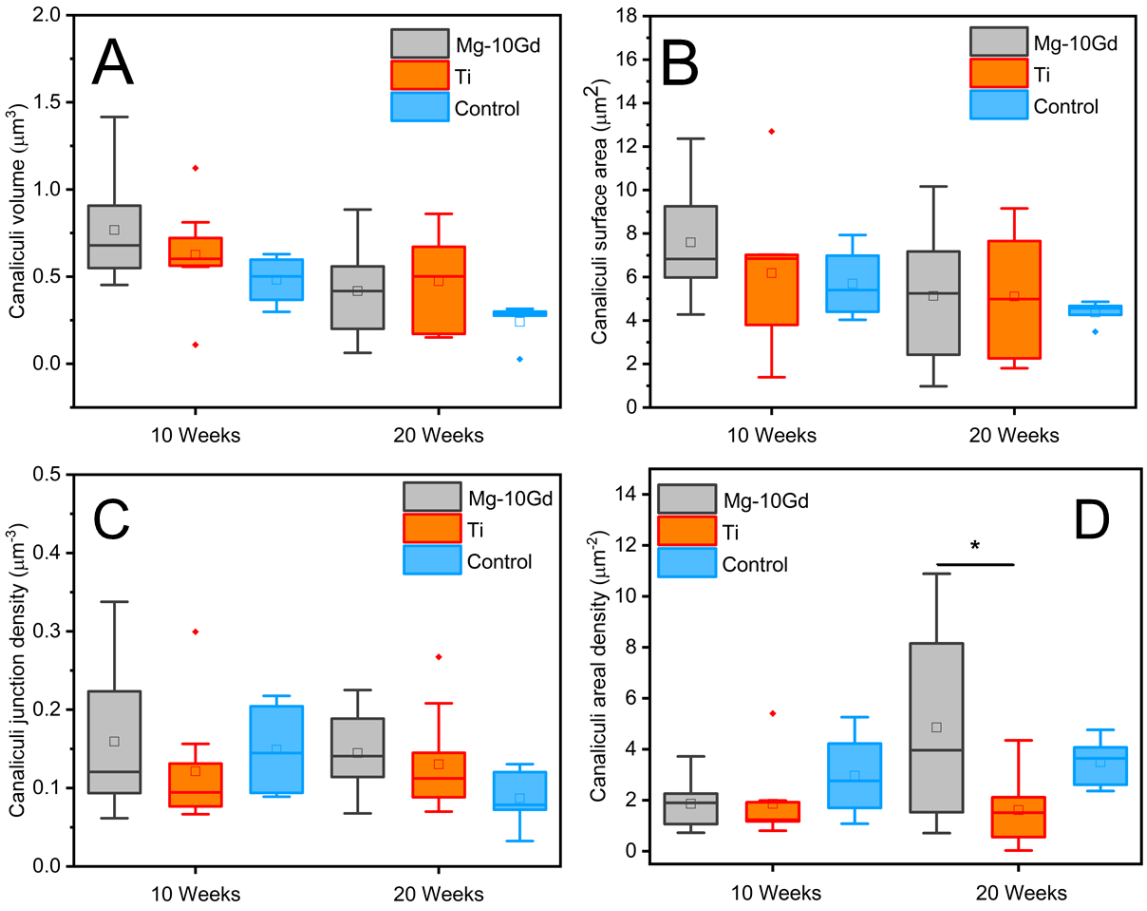

Figure 4.11: Boxplot of canaliculi descriptors (A) canaliculi surface area, (B) canaliculi volume, (C) junction density and (D) canaliculi areal density. * means significant ($p < 0.05$). Within each boxplot, the horizontal line represents the median while the small box represents the mean. From Sefa *et. al.*[19]. Published under the Creative Commons CC-BY 4.0 Licence.

4.2.2.5 Differences in the adaptation the LCN within the interfacial cortical and trabecular bone of Mg-10Gd

The descriptive statistics are summarized in table 5 in the Appendix A. For Mg-10Gd at 10 weeks, the mean lacunar volume of the cortical region was significantly ($p < 0.05$) higher than that of the trabecular region but not at 20 weeks (figure 4.12A). The same trend was seen in

the mean lacunar surface area where the bone within the cortical region had significantly higher mean lacunar surface area compared to that of the trabecular region at 10 weeks ($p < 0.05$) but not at 20 weeks (figure 4.12B). No significant ($p > 0.05$) differences in the mean canaliculi volume (figure 4.12C) nor canaliculi surface area at either 10 or 20 weeks (figure 4.12D) within trabecular bone and cortical bone for Mg-10Gd was recorded. By comparison, the trabecular and cortical bone within the interfacial bone of Ti did not significantly ($p > 0.05$) vary in terms of lacunar size (figure 4.13A&B) or canaliculi size (figure 4.13C&D) at 10 and 20 weeks.

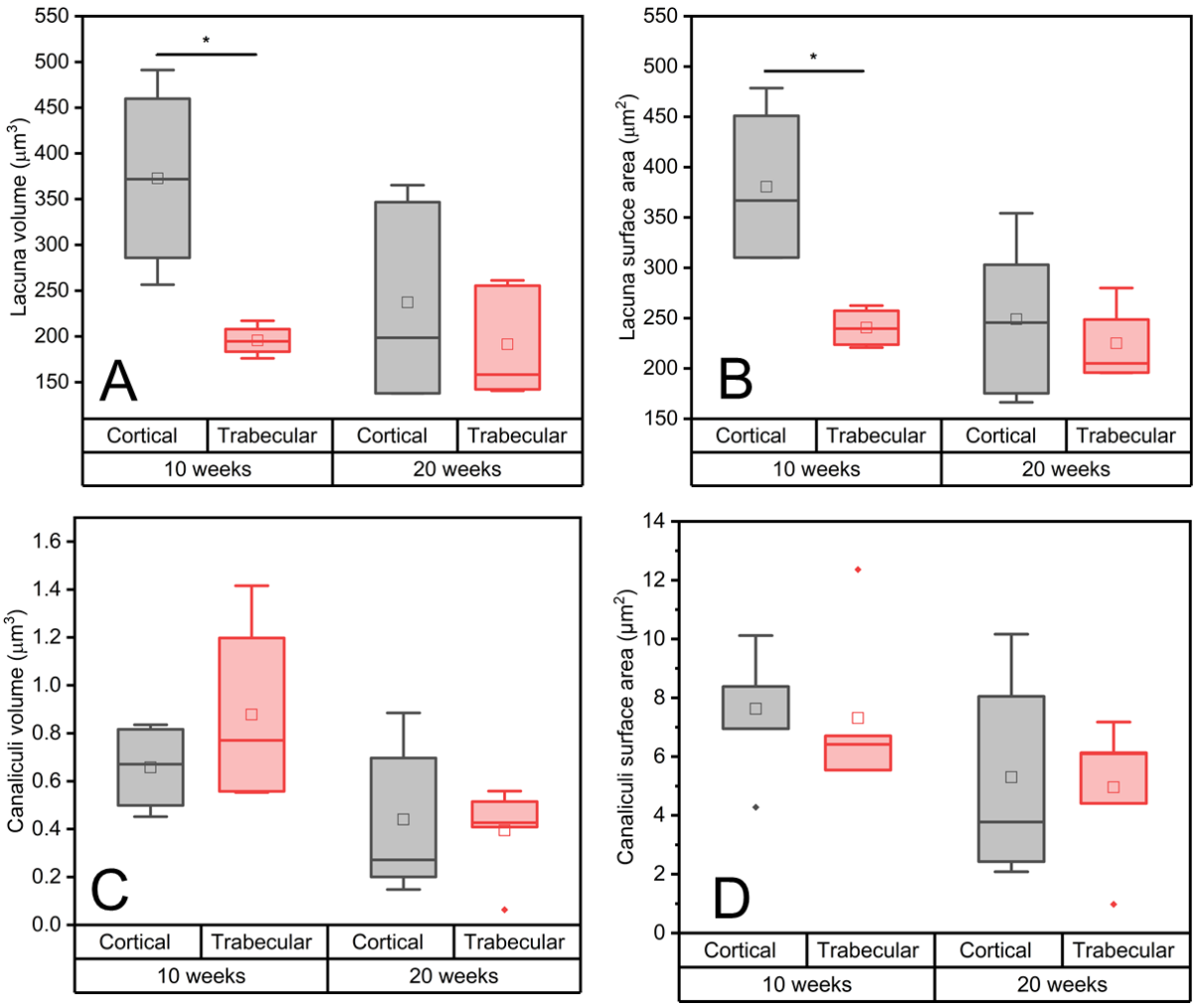

Figure 4.12: Boxplot of lacunar and canaliculi descriptors in cortical and trabecular bone of Mg-10Gd (A) at 10 and 20 weeks post-implantation. (A) lacunar volume, (B) lacunar surface area, (C) canaliculi volume, (D) canaliculi surface area * means significant ($p < 0.05$). Within each boxplot, the horizontal line represents the median while the small box represents the mean. From from Sefa *et. al.*[19].

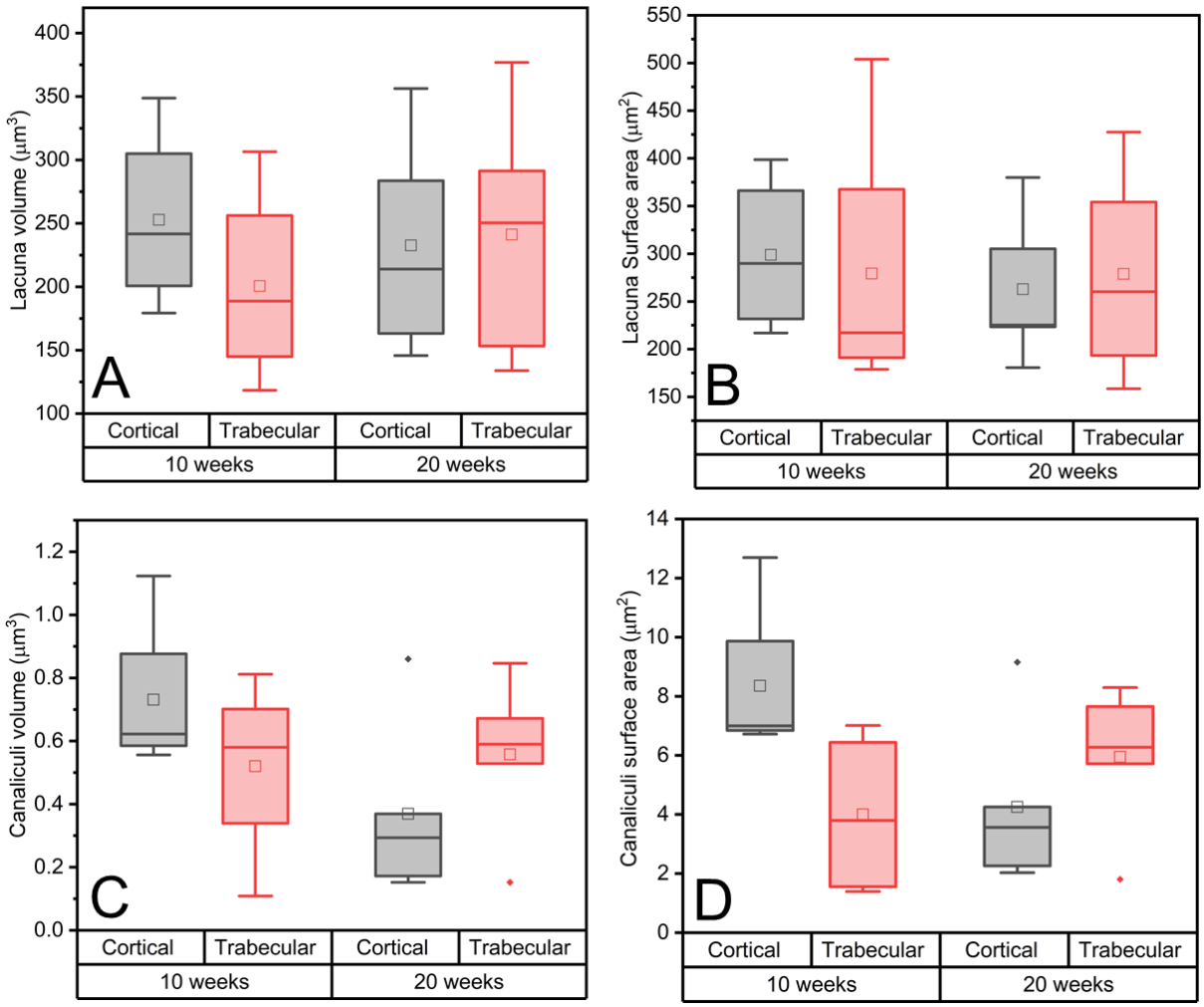

Figure 4.13: Boxplot of lacunar and canaliculi descriptors in cortical and Ti at 10 and 20 weeks post-implantation. (A) lacunar volume, (B) lacunar surface area, (C) canaliculi volume, (D) canaliculi surface area. Within each boxplot, the horizontal line represents the median while the small box represents the mean. From from Sefa *et. al.*[19]. Published under the Creative Commons CC-BY 4.0 Licence.

4.2.2.6 Fluid flow simulation

The results of the fluid flow simulation within the connected canaliculi of the lacunar pairs are displayed in figure 4.12 and the descriptive statistics are in table 4A&B in Appendix A. In figure 4.12A&B, it appears that the velocity and pressure distribution within the canaliculi vary depending on the number of canaliculi per lacunar surface area and junction density. However, the quantitative analysis based on the connected canaliculi (excluding non-connecting canaliculi) did not reveal significant differences in the average pressure and velocity within the canaliculi of Mg-10Gd, Ti and the control bone specimens (Figure 4.14C&D). A trend, however, was noticeable: for both implant types as well as the control group, the average pressure and velocity (Figure 4.14C&D) were lower and less variable at 20 weeks compared to 10 weeks.

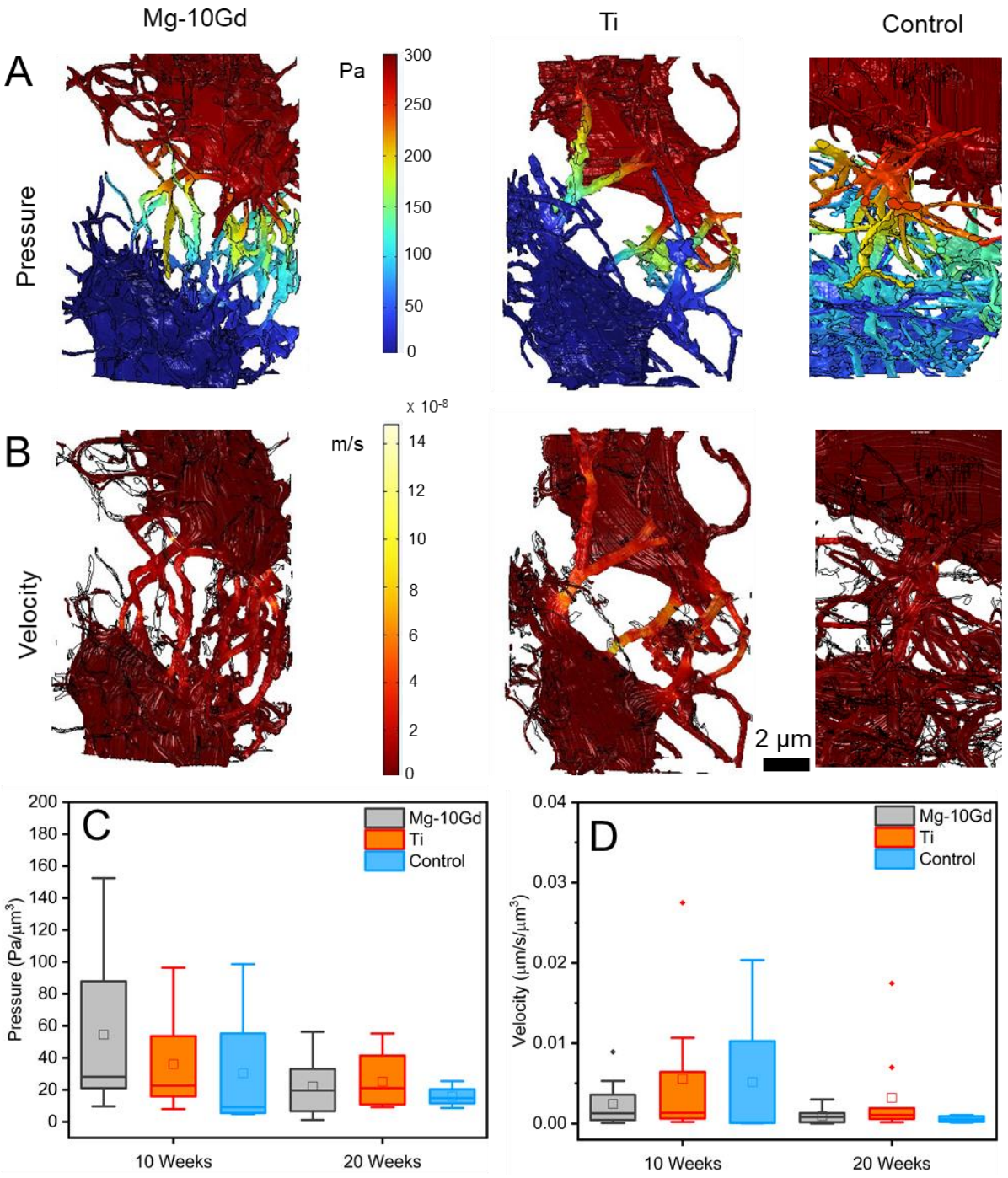

Figure 4.14: Display of the fluid flow within lacunae pair within the interfacial bone of Mg-10Gd, Ti and control bone specimens. 3D rendering of the pressure (A) and velocity (B) distribution within a pair of lacunae. (C) Boxplot of the mean pressure and (D) mean velocity within connected osteocyte canaliculi. Within each boxplot, the horizontal line represents the median while the small box represents the mean. Obtained from Sefa *et. al.*[19]. Published under the Creative Commons CC-BY 4.0 Licence.

Chapter 5

Discussion

In this thesis, the interaction of bone with biodegradable Mg-based implants was investigated at two length scales using both two and three dimensional analytical techniques in two *ex vivo* studies (**Studies I & II**). The Mg-based screws investigated were Mg-10Gd, Mg-4Y-3RE and Mg-2Ag. A macroscale investigation was performed in **Study I**, where the osseointegration of the aforementioned alloys was quantified in terms of bone formation, bone-implant bonding and the evolution of the degradation products. **Study II** was focused on characterizing the adaptation of the bone microstructure on the microscale, coupled with fluid flow simulation within the interfacial bone of Mg-10Gd compared to Ti and bone specimens taken far away from the implantation area of the Ti samples. The discussions pertaining to the two studies have been published here[18,19] thereby resulting in their rephrasing and further establishing a link between the two in this chapter.

Study I: Assessing the long-term *in vivo* degradation behavior of Mg-10Gd, Mg-4Y-3RE and Mg-2Ag.

The following sections have been rephrased from the publication here[18].

Osseointegration of Mg-based implants

In the extensive evaluation of bone response to both binary (Mg-2Ag) and ternary Mg-based (Mg-10Gd and Mg-4Y-3RE) implants over the long term, a consistent and comparable reaction of the bone tissue to all types of screws was observed. During the degradation process of Mg-2Ag implants, bright spots indicative of Ag-oxides[13] (figure 4.1) were prominent. Similarly, in Mg-10Gd degradation products, high X-ray absorbing areas were detected, possibly corresponding to GdH_2 (figure 4.1). Furthermore, in the degradation products of Mg-4Y-3RE, the presence of bright spots suggests the potential occurrence of Nd and Y precipitates[13] (figure 4.1 and figure 4.3). The degradation products of Mg-10Gd and Mg-4Y-3RE implants exhibited intermittent micro cracks, which might have been imposed during to sample preparation. At both implantation times, a substantial volume of bone was observed surrounding the screws (figure 4.1 and figure 4.3). The average bone volume fraction (BV/TV) was found to be above 40% for all screw types at 6 months, and this trend remained relatively stable for Mg-4Y-3RE and Mg-2Ag at 9 months. However, for Mg-10Gd, the BV/TV showed a slight decrease at 9 months compared to the 6-month measurement. In a previous short and mid-term study conducted by Galli *et al*., they reported fibrous tissue encapsulation around Mg-2Ag implants at 1 month, and later at 3 months, unmineralized bone was observed around the Mg-2Ag implants[159]. However, the current long-term evaluation revealed mineralized bone morphology around the Mg-2Ag implants, similar to that observed around the Mg-10Gd and Mg-4Y-3RE screws. This indicates that all three screw types induced a comparable osteogenic effect on the bone over the long term. The BIC consistently measured was above 40% for all screw types. Notably, Mg-2Ag and Mg-4Y-3RE screws displayed slightly higher BIC values at 9 months compared to 6 months. These findings suggest that despite the occurrence of degradation, all screw types remained firmly anchored in the bone. The BIC values indicated successful osseointegration, demonstrating the effective integration and stability of the screws within the surrounding bone tissue over time. Although Mg-10Gd showed a slight reduction in BIC at 9 months compared to 6 months, it is important not to hastily conclude that the BIC is

compromised. This is particularly evident due to the observed intimate contact between the Mg-10Gd screws and the surrounding bone at both healing times (figure 4.1 and figure 4.3). Despite the small decrease in BIC, the close interaction between the Mg-10Gd screws and the bone suggests that the osseointegration process remained intact, indicating that the screws maintained a secure and stable attachment within the bone tissue (figure 4.1 and figure 4.3). It is noteworthy to highlight that the osteotomy gap was fully bridged as early as 6 months, indicating a successful encapsulation of the screws within the surrounding bone. This observation aligns with a similar study by Krüger *et al*., where they reported excellent anchorage of Mg-5Gd and Mg-10Gd implants within the surrounding bone, with no gaps observed between the implants and the bone at the bone-implant interface, unlike in the case of PEEK implants[14]. This further supports the notion that the Mg-based implants exhibited effective osseointegration and provided a stable connection with the surrounding bone tissue. Remarkably, the current long-term investigation showed that the disintegration of Mg-2Ag during degradation did not compromise the bonding with the surrounding bone. However, it appears that the mechanical competence of Mg-2Ag screws could be affected due to the severity of the degradation. This contrasts with a contradictory observation reported by Galli *et al.,* who found that at 3 months, the bone-implant contact (BIC) of Mg-2Ag screws was sparsely in contact with bone, with an average value below 10 %[159]. A possible explanation for this discrepancy could be related to the different healing times assessed in the studies. It is hypothesized that during the shorter healing times of 1 and 3 months, faster changes might have occurred in the degrading Mg-2Ag screws, which potentially hindered the establishment of a stable interface for bone deposition and maturation around these screws. However, as the healing time extended, it was observed that the formation of more stable degradation layers, likely providing a favorable environment for bone formation and maturation to anchor securely to the screws. This finding highlights the importance of considering the healing timeline when assessing the effects of degradation on bone-implant interactions. The longer-term evaluation revealed a more stable integration of the Mg-2Ag screws with the surrounding bone, suggesting that the implants' degradation products eventually provided a suitable anchorage for bone formation and maturation. Thus, the findings suggest that Mg-2Ag implants were inherently non-toxic to the bone; however, it is likely that their degradation process did not favor initial bone integration. In contrast, the results for Mg-10Gd and Mg-4Y-3RE implants align with the current long-term study (**Study I**), demonstrating successful integration of these screws within the surrounding bone tissue. The observed discrepancies between the screw types in terms of their initial bone integration could be attributed to the specific degradation characteristics of each implant material. While Mg-2Ag implants may have faced challenges in the early stages of bone integration due to their degradation modality, their findings on Mg-10Gd and Mg-4Y-3RE implants showed favorable integration with the surrounding bone, proving to be effective choices for successful osseointegration just like the current findings in **Study I**.

Qualitative evaluation of degradation rate

As previously mentioned, it was challenging to calculate the degradation rate in the current long-term study (**Study I**) due to the similar electron density observed between the degradation layer and the remaining screw. Attempting to calculate the degradation rate from µXRF maps would lead to erroneous results due to the inhomogeneity present in the degradation layer. Therefore, quantitative determination of the degradation rate was not feasible using the available data. Given these limitations, qualitative assessment was employed to gain insights into the degradation behavior of the screws. The qualitative evaluation of the degradation profiles was based on the appearances and volumes of the remnant screws at both implantation times (figure 4.1, figure 4.2, and figure 4.3). This qualitative approach enabled drawing general comparisons between the different screw types in terms of their degradation

rates, providing valuable information despite the absence of specific numerical calculations. It is plausible to propose that Mg-10Gd and Mg-4Y-3RE displayed similar degradation patterns, as evidenced by the maintenance of their original screw shapes and comparable remnant screw volumes at 6 and 9 months of implantation (figure 4.1 and figure 4.2). Conversely, for Mg-2Ag, the shape of the remnant screws underwent considerable alterations (figure 4.1, figure 4.2, and figure 4.3), and the remnant screw volumes at 6 and 9 months were significantly lower compared to Mg-10Gd and Mg-4Y-3RE screws (figure 4.5C). These observations may imply that Mg-2Ag degraded at a different rate compared to Mg-10Gd and Mg-4Y-3RE implants. The distinctive degradation behavior of Mg-2Ag, reflected in the altered screw shape and reduced remnant screw volumes, suggests that its degradation rate may vary from that of Mg-10Gd and Mg-4Y-3RE implants. This finding underscores the importance of considering the individual degradation characteristics of different implant materials, which can influence their long-term performance and interactions with the surrounding bone tissue. The morphologies of the remnant screws presented in this study (**Study I**) are consistent with the findings of Galli *et al*.[159], except that, in their study, the degradation layer of Mg-2Ag was loosely attached to fibrous tissue. The observed changes in the appearance of Mg-2Ag can likely be attributed to its rapid degradation, leading to the formation of a smaller degradation layer and the generation of more soluble degradation products compared to Mg-10Gd and Mg-4Y-3RE implants. This assumption aligns with an earlier study by Zeller-Plumhoff *et al*., where the authors reported that a higher degradation rate was associated with a lower precipitation rate of degradation products[261]. Galli *et al*. reported highest *in vivo* degradation rate for Mg-10Gd (1.15 ± 0.19 mm/year) followed by Mg-2Ag (1.01 ± 0.11 mm/year) and lastly Mg-4Y-3RE (0.82 ± 0.10 mm/year) at 1 month observation period[159]. Furthermore, Myrissa *et al*. recorded that Mg-10Gd degraded faster compared to pure Mg and Mg-2Ag *in vivo* at 4 weeks observation period[262]. It is important to point out that the observations from the reference[13] and reference[262] were focused on the early phase of implantation while this thesis observations were focused on the late phase of implantation (6 and 9 months). In a study conducted by Witte *et al.*, they investigated the degradation rates of various magnesium-based implants and found that the addition of RE elements to Mg resulted in a decreased oxidation rate, leading to a slower overall degradation[119]. These findings are consistent with the results of this study (**Study I**). It is worth noting that there have been discrepancies in reports between short-term and mid-term evaluations of Mg-based alloys. These variations in observations reinforce the importance of conducting long-term evaluations to gain a comprehensive understanding of the *in vivo* temporal performance of Mg-based implants

Elemental analysis of the degradation layer

Using µXRF (figure 4.4), the qualitative assessment and visualization of elemental distribution within the degradation layer, surrounding bone, and soft tissue following a 9-month implantation period was performed. The surrounding layer consistently revealed the presence of Ca and P for all screw types while the presence of Gd, Y and Ag elements were unique to each specific alloy. The presence of Y in Mg-4Y-3RE screws was only observed in the former implant area, with no visible Y detected in the surrounding bone or soft tissue. In contrast, Turyanskaya *et al.* found a pronounced spreading and accumulation of Y in the surrounding bone when they studied the degradation of WZ21 implants after 1 month of implantation using the µXRF technique[263]. In an *in vitro* corrosion test of Mg-Y alloys, researchers noted that Y is oxidized into yttrium oxide (Y_2O_3) as it migrates to the metal surface of the alloy, suggesting a potential accumulation of Y in the degradation layer[264]. The accumulation of Gd was exclusively observed in the former implant area, with no indication of Gd in the surrounding bone or soft tissue due to the absence of Gd signal. The findings of the current study is consistent with that of Peruzzi *et al*. who used neutron µCT to show that Gd remains localized in the degradation layer following the degradation of Mg-5Gd and Mg-10Gd implants[173]. The

scenario is markedly distinct for the Ag maps of Mg-2Ag samples. While the Ag signal is exclusively detected in the degradation layer, its appearance seems disintegrated. This suggests the formation of soluble Ag-complexes during degradation, which subsequently migrated and were either expelled from the system or assimilated into the animal's metabolism. This inference is drawn from the absence of any Ag signal in the surrounding bone and soft tissue.

The decline of Mg in the degradation layer is counterbalanced by a simultaneous increase in Ca and P for all scew types, suggesting a progressive substitution of Mg by P and Ca in the degradation layer. P and Ca are the primary components of hydroxyapatite ($Ca_{10}PO_4OH_2$), which constitutes the inorganic part of bone. Under physiological conditions, the ions PO_4^{3-} and Ca^{2+} are known to precipitate on Mg-based implants through biomineralization processes[16]. Consequently, the presence of P and Ca in the degradation products of all implant types indicates the biocompatible effect of the investigated Mg-based screws. Furthermore, the µXRF maps (figure 4.4) validate the presence of S in the degradation layers of all screw types, as well as in the surrounding bone and soft tissue, indicating the presence of proteins. For instance, evidence suggests the formation of Y-protein complexes after intravenous administration of of Y^{177}. The signal intensity of S in Mg-2Ag appears more pronounced than that observed in Mg-10Gd and Mg-4Y-3RE degradation products, potentially indicating a higher binding of proteins to Ag due to its disintegration[259,260]. Helmholz *et al*. also reported the formation of Ag-S agglomerates in the degradation layer during an *in vivo* study involving Mg-2Ag[265]. Furthermore, from the histological slides (figure 4.3), it is evident that the formation of protein complexes in the degradation layer is consistent across all screw types. Both Mg-10Gd and Mg-4Y-3RE degradation layers exhibit a similar purplish appearance, suggesting the potential staining of proteins with toluidine blue. Additionally, the Y-precipitates observed in the SRµCT slides (figure 4.1) for Mg-4Y-3RE screws are also evident in the histological data (figure 4.3). In contrast, the degradation layer of Mg-2Ag screws appears brown in the histological data (figure 4.3), aligning with the high signal intensity of their corresponding S maps. This observation may support the idea of higher protein binding in the degradation layer of Mg-2Ag.

Effect of blood pre-incubation of Mg-based implants on osseointegration

Additionally, the impact of pre-incubating the three Mg alloys (Mg-10Gd, Mg-4Y-3RE, and Mg-2Ag) in blood on their *in vivo* biocompatibility compared to their respective control groups was probed. Table 1C in Appendix A displays lower mean BV/TV in the blood pre-incubated group compared to the control group for all screw types at both 6 and 9 months of implantation. Notably, at 6 months, the mean BV/TV of the blood pre-incubated Mg-2Ag group was significantly lower than that of the control group ($p < 0.05$). Additionally, at both 6 and 9 months, the blood pre-incubated group exhibited higher mean BIC compared to the control group for all screw types, except for Mg-4Y-3RE (Table 1C). Notably, the mean BIC of the Mg-2Ag blood pre-incubated group was significantly higher than that of the control group at 9 months ($p < 0.05$). As mentioned earlier, when biomaterials come into contact with blood, proteins are absorbed onto their surfaces, influencing the material's biological response and biocompatibility [140,141]. In the case of Mg alloys, these adsorbed proteins have been found to enhance their corrosion resistance and promote cell adhesion adhesion[266–268]. Moreover, research indicates that over time, the conformational structures of the adsorbed proteins on biomaterials can undergo changes, subsequently affecting the behavior of cells interacting with the biomaterials[269,270]. The dynamic changes experienced by adsorbed proteins over time has been confirmed by Romero-Givalan *et al*.[271]. Thus, it is reasonable to infer that the adsorbed protein layer on the screws similarly underwent structural modifications in the long-term. Additionally, the potential interaction between Mg ions and the protein layer should not be overlooked. It can be speculated that the reduction in Mg content over time, as the screws degraded, might have altered the adsorption kinetics in favor of enhanced cell attachment.

Proteins can be adsorbed onto a material using either a single protein like bovine serum albumin (BSA) or a multiprotein solution such as blood plasma. *In vitro* results typically rely on single proteins, which may not completely replicate the reactions observed in implanted biomaterials. Furthermore, it is essential to note that different surfaces exhibit varying selectivity in protein adsorption, and the biological activity of the adsorbed proteins can also differ among these surfaces. These variations contribute to the diverse results observed among the different types of screws. To gain understanding of protein conformation and its implications for Mg implants, further research is strongly recommended.

Study II: To characterize the microstructural adaptation of bone around Mg-10Gd using multiscale imaging

The content of this section has been restated from the publication here[19].

SRμCT investigation-assessing the impact of Mg-10Gd degradation on vascular and lacunar porosity

The distribution of the vascular porosity was mostly similar for Mg-10Gd and that of Ti (for both 2D and 3D analysis figures 4.7&4.8) except at 8 weeks where the vascular number density was significantly higher for Mg-10Gd compared to Ti within a distance of 200 μm from the implant screw resulting from the 3D quantification (figure 4.7C). One of the functions of the vascular porosity is to relax fluid pressure around the LCN for efficient transport and metabolic exchange[272]. The result may imply that pressure moderation around the LCN was mostly similar for both materials. However, at 8 weeks, there was an enhanced pressure moderation and increased metabolic need in the local vicinity of the Mg-10Gd screws (200 μm from the screw) compared to Ti. The reason for the enhanced metabolic need is not apparent but it may be conceived that there was a high demand to regulate Mg homeostasis thus the need for enhanced circulation. The assertion is not corroborated by the volume loss measurements of the samples used in this study, where Krüger *et al*. showed that the relative volume loss between the time of implantation and 4 weeks of healing is higher than that between 4 and 8 weeks[14]. Furthermore, Tartrate resistant acid phosphatase (TRAP)-positive area percentages (TRAP %) analysis by Krüger *et al*. showed a continuous decline in TRAP-positives regions for Ti from 4 to 12 weeks while that of Mg-10Gd decreased from 4 to 8 weeks and increased again slightly from 8 to 12 weeks[14]. Regions that show TRAP-positive staining is indicative of osteoclast activated for bone resorption. The hypothesis suggests that osteoclasts secrete osteopontin[273] or Metalloproteinase-9[274] to stimulate angiogenesis. Notably, blood vessels and osteoclasts are found in close proximity in each bone remodeling compartments to enhance efficient exchange of signals and molecules between these two entities[274]. Yet, the result of the TRAP-positive analysis reported by Krüger *et al.* was inadequate to fully explain the rise in vascular number density around Mg-10Gd at 8 weeks post-implantation. In view of this, future studies which focus on alternative markers or analytical methods (e.g. cytokine signaling or cellular interactions) are recommended to give further insights to deepen our knowledge. The modulation of pressure within the LCN by the vascular porosity is crucial for the efficient exchange of pore fluid between the two porosity levels[272]. So far, it is known that Mg accumulates around blood vessels and within the bone marrow when the degradation speed of Mg-based implants is moderate[174].

In both local and global intances (200 μm and 500 μm from the implanted screws respectively) significantly lower lacunar number density was recorded around Mg-10Gd compared to Ti from 4 to 12 weeks post-implantation resulting from the 3D analysis (figure 4.7A&B). Two ptentional factors could account for the observed results: either Mg-10Gd probably altered the bone

formation dynamics or the bone formation around Ti was reinforced. The latter could either be explained by enhanced osteoblastic activities prior to differentiation or higher incidence of microcracks within the interfacial bone of Ti since higher incidence of microcracks result in higher stimuli for bone remodelling[275]. The result may point to a lower bone turnover rate[276,277] and bone mass[278] around Mg-10Gd implants which implicates lower remodeling rate for Mg-10Gd implant screws in comparison to Ti . This may explain the significantly higher bone volume fraction for Ti implants in comparison to Mg-10Gd implants at 4 and 8 weeks observed by Krüger *et al*. in the same samples[14] used in **Study II**. Indicatively, Krüger *et al.* recorded BV/TV for Mg-10Gd to be 25.1 ± 8.5 %, 34.9 ± 5.0 % and 47.6 ± 6.2 % respectively while that of Ti were 48.8 ± 0.4 %, 51.3 ± 4.6 % and 49.1 ± 7.7 % at 4, 8 and 12 weeks respectively[14]. Thus, it is evident that the higher BV/TV observed for Ti could contribute to the greater number of osteocytes compared to Mg-10Gd since lower BV/TV implicates lower overall volume of bone tissue available for osteocyte occupancy. In the process of osteoblastic differentiation into osteocytes, conditions that disrupt osteoblasts activities may have an impact on the subsequent osteocyte population[279,280]. Disturbances in osteoblasts function such as decreased proliferation, compromised signaling pathways or changes in extracellular matrix stiffness can affect the quantity and viability of osteoblasts that transform to osteocytes[279,280] and consequently bone health and remodeling. There are conflicting reports on the impact of Mg degradation on osteoblasts. Some researchers have reported an upregulation of osteoblast markers, such as ALPL, BSPII, and osteocalcin, in cell lines when exposed to Mg ions[179,180]. Contractictory findings by subsequent researchers showed that Mg degradation exhibits an inhibitory effect on osteoblasts activities[111,181,183]. These discrepancies could be attributed to several factors, including variations in study models, experimental protocols, Mg concentrations, and the specific alloys used in the investigations. It could be hypothesized that the incorporation of Mg degradation products in the bone altered the bone matrix mineral content within the vicinity of Mg-10Gd implants. The lower remodelling rate of the bone around Mg-10Gd could explain why Zeller-Plumhoff *et al*. recorded a lower HAP spacing and size around Mg-10Gd in comparison to Ti[16]. It has been reported by several researchers that upon degradation of Mg-based implants, Mg is distributed within the lacunae network and alters the crystal structure of the bone[174,281]. The modification of the bone matrix mineral content is further corroborated by Peruzzi *et al*. who reported increased Ca and P levels around Mg-10Gd in comparison to Ti[173]. In figure 4.6, unmineralized interfacial bone regions could be observed from SRµCT analysis after 8 weeks of implantation possibly indicating the alteration of bone matrix mineral content due to the incorporation of Mg within the bone. Based on 2D technology, several studies have shown that peri-implant bone healing involving permanent implants are associated with higher osteocyte density[57–59]. In particular, Ti6Al4V implant surfaces have been reported by Shah *et al*. to retain a higher density of less aged osteocytes and enhanced bone maturation[59]. However, those studies lack direct comparison to degradable implants which is a limitation defeated by this thesis. The considerable decrease in vascular density around Ti implants at 8 weeks raises the need for additional research to understand the underlying mechanism responsible for this result.

At 20 weeks, the 2D porosity analysis revealed a significant difference only in the lacunar number density at 500 µm from the screw (figure 4.8B). The vascular number density was not significant at both 10 and 20 weeks (figure 4.8C&D). The differences in 2D and 3D analysis could be attributed to the use of different animal cohorts as well as the use of different image acquisition methods in both studies. It is known that the outcome of bone porosity measurements majorly depends on animal age[34,252]. Although the same rat specie, gender and similar anatomical location was used in both studies, the age of the rats was different which can significantly influence the bone porosity characterization in the different animal cohorts. In addition, tomographic techniques yield detailed information on samples in 3D in comparison to conventional methods[282]. Notably, the lacunar and vascular porosity distribution reported in

this study fall within the ranges found in literature[29,283], nonetheless variations may exist according to inter-animal variations as well as to the resolution of the modality used.

TXM investigation – assessing the impact of Mg-10Gd degradation on the LCN morphology

For both Mg-10Gd and Ti, the mean lacunar volume, surface area and LCN porosity were higher than that of the control bone specimens at 10 and 20 weeks (figure 4.10A-C). Though not significant, the trend may suggest differences in the maturity of the osteocytes within the interfacial bone of both implant materials in comparison to the control bone specimens. The nature of the interfacial bone of both implants is woven, which is known to be less mature compared to a pre-existing bone[52]. Evidently, osteocytes within the bone adjacent to Ti implants have been shown to be larger in size than those in mature bone which indicate a less aged morphology[59]. Lacunar shape, which is formed during osteoblastic differentiation[284], reflects the shape of the osteocyte within the lacunar[34] and affects the mechanosensation of the osteocyte[285]. There was no significant difference in the sphericity and anisotropy (a measure of the deviation from sphericity) of the lacunar within the interfacial bone of both implant materials as well as the control bone specimens (figure 4.10D), implying a similar round morphology of the osteocytes around both materials and the control bone specimens. Round osteocytes are known to be most mechanosensitive because they can exhibit higher volumetric deformations due to the elasticity of their exoskeleton differentiation[285]. The results may imply similar mechanosensation of the osteocytes of both materials as well as the control bone specimens.

The 3D rendering of the LCN architecture in figure 4.9 shows a direct attachment of the canaliculi to the implant screws of both materials at 10 weeks post-implantation while the lacunae were aligned parallel to the screw similar to the report of Shah *et al.*[59]. This might implicate that the surfaces of both implant materials presented a conducive environment for canaliculi attachment which is pivotal for successful osseointegration[52]. This further indicates enhanced interfacial stress transfer between the implants and osteocytes consequently enhancing fluid flow within the LCN[52]. A large canaliculi surface area is known to substantially contribute to the bone mineral homeostasis by directly interacting with the ECM[286]. From figure 4.9 and figure 4.11A&B, the surface area and volume of the canaliculi around Mg-10Gd presented an enlarged surface morphology in comparison to Ti and the control bone specimens at 10 weeks which might implicate a higher potential for mineral exchange. The canaliculi junction density, which signifies the branching of the osteocyte cell processes, was not significantly different for both materials and the control bone specimens. This suggests a similar pressure regulation within the canaliculi of the interfacial bone of both implant materials and the control since the branching of the canaliculi tends to reduce maximum pressure within the canaliculi to facilitate biotransport[224]. The significantly higher canaliculi per lacunar surface area for Mg-10Gd at 20 weeks implies higher connections[41] between the osteocytes which facilitates mechanotransduction and mass transport[287].

It has been hypothesized that, to regulated the mineral homeostasis within bone, the osteocytes and their cell processes directly interact with the ECM via the LCN[23,51,253]. In view of this, the distance distribution of the LCN was investigated revealing that for both implant materials as well as the control bone specimens, the bone matrix was in close proximity to the nearest lacunae or canaliculi. The result implies that the distance within which ions must diffuse through the bone matrix is lower for the control compared to Mg-10Gd and Ti. The drive for perilacunar remodeling has been hypothesized to be due to ion demand or stress[23]. Kerschnitzki *et al*. reported that 60 % and 80 % of the bone matrix reside within a distance of 1 µm and 1.4 µm respectively[253] from the cell network of ovine fibrolamellar bone, whereas Bortel *et al.* reported $Ca.Dist_{50}$ values ranging from 1.6 µm to 2.1 µm[224] in human femoral and

jaw bone[224]. Also, Dong *et al*. reported $Lc.Dist_{50}$ values between 12.6 µm to 16.8 µm in human femoral cortical bones[252].

Cortical and trabecular bone have been shown to be morphologically different thus they adapt differently during bone remodeling[288,289]. In this study, there was a significant difference in the lacunae size between cortical and trabecular bone of Mg-10Gd at 10 weeks (figure 4.12A&B). Since this significant difference was not recorded for the Ti group (figure 4.13), our result might indicate that the incorporation of Mg-10Gd in the bone impacts differently on the perilacunar adaptation of the two bone types. Akhter *et al.* also reported significantly larger lacunar volume in cortical bone in comparison to trabecular bone but in a different disease model[289].

The fluid flow within the LCN is dependent on the morphology and organization of the LCN[224,252]. The pressure and velocity distributions within the connecting canaliculi of the lacunae pairs did not significantly vary (figure 4.14) among the two implant material types as well as the bone specimens possibly because there was no significant morphological difference in their architecture. Branching of the osteocytes has been shown to reduce excessive pressure within the canaliculi for efficient transport[41] and higher canaliculi per lacunar surface area results in higher connectivity between the osteocytes which leads to efficient transport. The impact of the higher canaliculi per lacunar surface area for Mg-10Gd at 10 weeks on the pressure and velocity distribution could not be confirmed likely due to the use of lacunae pairs instead of the whole morphology of the LCN.

Establishing an intrinsic link between macroscale (Study I) and microscale (Study II) findings of Mg-10Gd

In this thesis, degradation rate of the investigated alloys (Mg-10Gd, Mg-4Y-3RE and Mg-2Ag) in **Study I** was not calculated as previously stated. Nonetheless, since these alloys (Mg-10Gd, Mg-4Y-3RE and Mg-2Ag) were prepared in the same way as those utilized in the short and mid-term study of Galli *et al.*[13], their microstructure are expected to be similar with a similar degradation profile. That of the Mg-10Gd screws used in **Study II** has previously been calculated by Krüger *et al*[14]. The result of the degradation analysis from Galli *et al.*[13] and Krüger *et al*.[14] as well that of Iskhakova *et al*.[15] have been compiled in figure 5A. Here the impact of the differences in the fabrication of Mg-10Gd alloys on their degradation performance is displayed for the same healing period in a rat model. The degradation rate of Mg-10Gd recorded by Galli *et al*.[13] was 58.43% and 40% higher than that recorded by Krüger *et al*.[14] at 4 and 12 weeks respectively. Notably, the microstructure of the Mg-10Gd used in both studies were different. Galli *et al.* reported relatively smaller Mg-10Gd grain sizes (21.9 ± 11µm)[13] and more Gd-rich intermetallic particles while Krüger and co-authors reported relatively larger grain sizes (26.67 ± 1.30 µm) and fewer agglomeration of Gd-rich particles[14]. It is firmly established that the degradation profile of Mg alloys are affected by the presence of phases, grain size, intermetallic particles[13] and the protective capacity of the formed surface layer during degradation[290]. Furthermore, it is widely recorgnized that the finer the grains and the fewer the intermemetallic particles are, the better the degradation resistance because in that case the degradation profile is homogenuous and localized[291]. However, grain size alone could not account for the differences in the degradation profile rather the number and distribution of the intermetallic particles seem to be a plausible reason. This highlights the need to optimize all factors that could potentially influence Mg alloys degradation during their fabrication process. By utilizing data from Krüger *et al*.[14] and Iskhakova *et al.*[15] the impact of degradation speed on bone formation has been assessed using regression analysis (figure 5B and table 6 in appendix A to establish a correlation between the two parameters from 4 to 32 weeks post-implantation. As shown in figure 5A and table 5 in appendix A, the relationship between BV/TV

and degradation is remarkably compelling. The data reveals a strong significant negative correlation with degradation indicating that as the degradation speed of Mg-10Gd declines, bone formation increases proportionally. Furthermore, for every 1 mm/yr increase in degradation rate, BV/TV decreases by 40.71. This further implies that bone formation is highest when degradation rate is kept to the barest minimum. The observation is not only peculiar to Mg-10Gd but also other Mg alloys such as Mg-2Ag and WE43, which has already achieved clinical application[292]. Jähn *et al*. reported continuous decline in *in vivo* degradation of Mg-2Ag from 1 weeks to 30 weeks with augmented callus formation over time[170]. Findings from Rendenbach *et al.* also suggest that lowest degradation rate of WE43 was associated with elevated bone formation[293]. Building on this observation, a generalization might be made that in order to achieve substantial bone formation when using Mg alloys for orthopedic applications, it is imperative that their degradation rate remains low.

From the macroscale analysis (**Study I**), the long-term osseointegration of Mg-10Gd and Mg-2Ag and Mg-4Y-3RE was shown to be optimum. To substantially augment comprehension of tissue level outcomes, it was imperative to embark on a comprehensive exploration of the bone microarchitecture, as investigated in **Study II.** Combing findings from **Study I** and **Study II**, it became apparent that the bone remodeling kinetics around Mg-10Gd was more comparable to that of Mg-4Y-3RE than permanent Ti implants due to the dynamic environment presented by Mg-10Gd degradation. The dynamic environment was probably similar for both Mg-4Y-3RE and Mg-10Gd due to the similar degradation rates (inferred from morphological evaluation of the residual screws in **Study I** and from Galli *et al*.[13] (figure 2.5) which might explain their comparable bone response. This point is highlighted in figure 5C where data from **Study I** as well as previous comparative *in vivo* investigations[14,15] of Mg-10Gd and Ti have been displayed. It is obvious that the bone formation around Ti was mostly more enhanced for Ti compared to Mg-10Gd over time. For both materials, BV/TV is initially high from 4 to 12 weeks, declines at 20 weeks then rises again between 20 to 30 weeks in a rat model. To buttress the findings of Krüger *et al*.[14], Bruns *et al*. has recently shown that Ti implants are more stable to withstand load and stimulates swift bone formation[294].

It is notably uncertain that the findings of **Study II** could explain that of **study I** due to some limitations. First, the use of different animal models is known to majorly impact *in vivo* experimental outcome due to differences in their bone metabolism and microarchitecture in comparison to humans[295–297]. Ideally, bone implants which are intended to be used in humans should be tested in animals models whose bone microarchitecture and metabolism closely resemble that of humans such as sheeps, goats, dogs, etc[295]. However, larger animals are difficult to handle and pose greater ethical issues. Therefore, they are mostly used for testing the final design of an implant prior to clinical applications[296]. Although, smaller animals such as rabbits and rats are largely dissimilar to humans, they are usually used to initially test bone implants during the initial development stages. By this, sufficient knowledge on implant behavior, tissue compatibility, toxicities, wound healing, tissue architecture, etc can be obtained for further implant refinement. Due to the healing times considered in this thesis, it was more reasonable to use rat and rabbit model who present faster bone turnover in comparison to humans[297]. The justification for the utilization of two different animal models in this thesis was to synthesize the bone characteristics of different animal specie's response to Mg-10Gd implants which can enable the acquisition of accurate data to facilitate its development for the clinic. As an example, in figure 5C, the bone response to Mg-10Gd in rat and rabbit models show different pattern of bone formation. While there seem to be a a rise in BV/TV at the latter healing times for rat model, the opposite is seen for rabbit model. It is unclear if the observed difference is due to specie-specific bone microarchitecture which presents different metabolic environments for Mg-10Gd degradation and/or differences in microstructure of Mg-10Gd utilized could potentially explain this behavior. For clarity, long-term

in vivo investigations of similar manufactured Mg-10Gd alloys should be performed concurrently in rats and rabbit models within the same time frame and compared. This way, impact of microstructurural differences in the alloy design on bone response could be eliminated enabling a direct assessment of species-specific bone response.

The finding highlights the promising potential of Mg-10Gd in promoting bone tissue formation and compels the alloy design to be further optimized. With continued research and refinement, Mg-10Gd holds great promise in revolutionizing bone regenerative therapies and addressing critical challenges in orthopedic and tissue engineering fields. Such optimization should be geared towards patient-specific designs that accurately incorporates their anatomic requirements/needs to promote successful osseointegration for individual cases. This will go a long way to improve bone regeneration and long-term clinical outcomes.

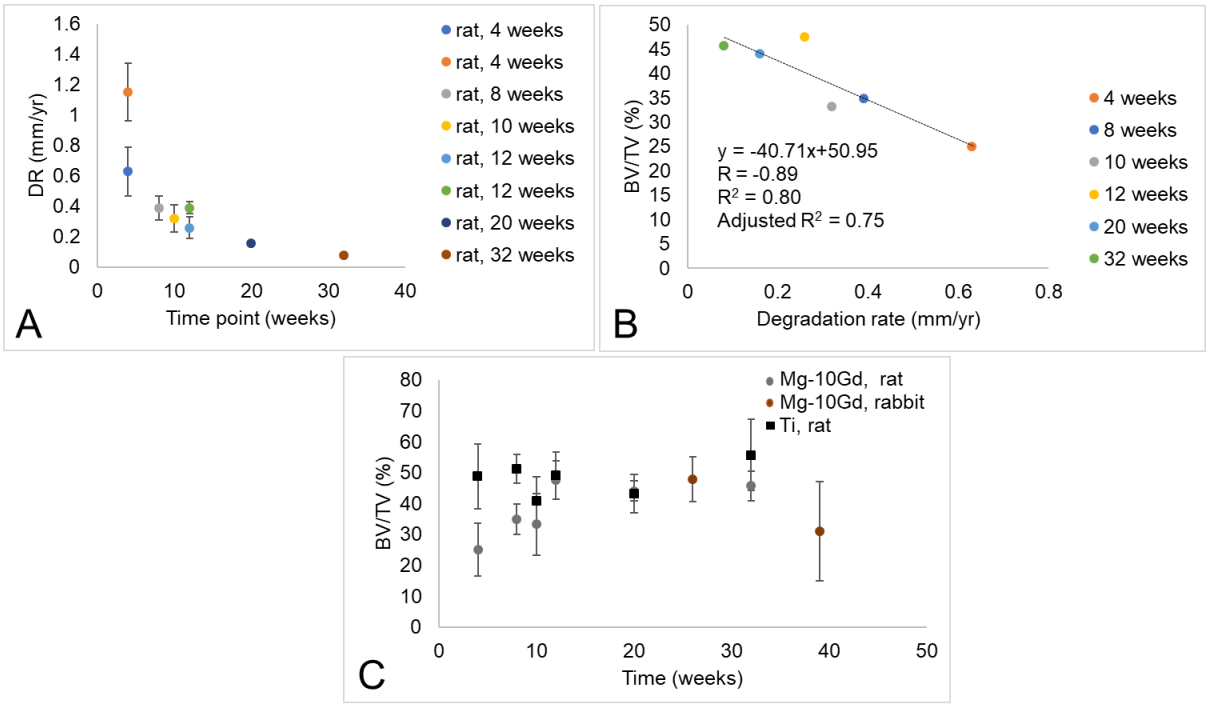

Figure 5: Summary of mean values with standard deviation of BV/TV and degradation rate parameters as well as a correlation between BV/TV and degradation. A) Correlation between BV/TV and degradation rate of Mg-10Gd data obtained from Krüger *et. al*.[14] (4,8 and 12 weeks post-implantation in rat) and Iskhakova *et al*.[15] (10, 20 and 32 weeks post-implantation in rat). B) Plot of degradation rate over time. Data was obtained from Krüger *et. al*.[14] (4,8 and 12 weeks post-implantation in rat), Galli *et al*.[13] (4 and 12 weeks post-implantation in rat) and Iskhakova *et al*.[15] (10, 20 and 32 weeks post-implantation in rat). C) Plot of BV/TV over time in different animal species. Data was obtained from Krüger *et. al*.[14] (4,8 and 12 weeks post-implantation in rat), Iskhakova *et al*.[15] and **Study I** (26 and 39 weeks post-implantation in rat).

Chapter 6

Conclusion and future outlook

In this thesis, the adaptation of the bone adjacent to Mg-10Gd, Mg-2Ag and Mg-4Y-3RE alloy implants was studied at two length scales i.e. the macro-and microscale scale in two e*x vivo* studies. On the macroscale, the long-term bone response of Mg-10Gd, Mg-2Ag and Mg-4Y-3RE were studied and compared in terms of bone formation, bone implant contact and the evolution of the degradation products at 6 and 9 months post-implantation. The micro-nanoscale study was focused on the impact of Mg-10Gd degradation on the vascular porosities and LCN morphology and functionality in comparison to Ti from 4 weeks to 20 weeks post-implantation. To this end, 3D synchrotron radiation micro- and nano-tomography complemented by histology, micro X-ray fluorescence and finite element analysis was utilized. The hierarchical multi-modality approach enabled the detailed assessment of the specific ways Mg degredation products affect the morphology of transport and communication pathways, enabling a deeper comprehension on tissue level outcomes.

The tissue level analysis revealed that in the long term, based on the quantified BV/TV and BIC, Mg-10Gd, Mg-2Ag and Mg-4Y-3RE exhibited a similar bone healing response despite the differences in their degradation dynamics. Notably, Gd and Y remained at the implantation site in their original threaded shape and did not show a deleterious effect on the bone, meanwhile Mg-2Ag appeared severely disintegrated with fewer degradation products implicating a less stable degradation layer. Comparing the results of the long-term investigation of this thesis with our previous short- and mid-term investigations[13], it is concluded that Mg alloys degrade in the long run into degradation products that are well tolerated in the body, hence they osseointegrate. However, short-term and mid-term *in vivo* investigations do not fully represent the complete degradation performance during the lifetime of such degradable implants because the dynamics of their osseintegration may differ, with some requiring more time than others (e.g. Mg-2Ag) since the differences in standard electrode potentials of the alloyants impact differently on Mg degradation. The degradation process of Mg-2Ag, is postulated to be accelerated by the presence of numerous microgalvanic couples because of the relatively higher standard electrode potential of Ag compared to that of Mg. The micro-nanoscale analysis showed that the degradation of Mg-10Gd is associated with a significantly lower lacunar density which implicates differences in remodeling kinetics and bone mass in comparison to standard Ti implants. On the other hand, the LCN morphology nor functionality did not significantly differ between Mg-10Gd and standard Ti implants. In conclusion, this study confirmed that the investigated alloys were well osseointegrated based on the quantified parameters in this thesis. In particular, Mg-10Gd degradation impacts the osteocyte population rather that their morphology.

The distribution of Gd and Y in the body is not clear. Whether they will remain indefinitely in the implantation site or will be disintegrated at a later time requires further investigation beyond the time scale considered in this thesis to enhance the understanding of the local and systemic effects of the degradation products. In addition, long-term impact of the degradation products on different tissues and organs physiology should be addressed. Since standard implants such as Ti and steel are widely used in the clinics, *in vivo* long-term performance Mg-10Gd, Mg-2Ag and Mg-4Y-3RE should be compared to such implants to enable a comprehesive assessment of the aforementioned alloys. As mechanical intergrity of implants is crucial for successful osseointegration and bone healing, failure analysis should be incorporated in in long-term *in vivo* studies. Information from such evaluations could be used to improve material design and fabrication of Mg-implants. Age is a key determinant of osteocyte morphology and functionality;

therefore, future studies should focus on understanding the influence of Mg degradation products on the LCN during the early phase of bone healing. Even better is to design future experiments such that influence of Mg-based implants on LCN is studied and compared among the various time points of bone healing. By this, the association between LCN adaptation and Mg degradation rate could be established. Furthermore, future studies should focus on the impact of different concentrations of Gd on the osteocyte morphology and population distribution at earlier implantation times. Also, is recommended that the combination of TXM and other microscopy techniques to confirm the presence of osteocytes within the LCN and enable multi-phase modelling of fluid flow within the LCN. It is also recommended that future studies should focus on understanding the influence of different Mg alloys on the vascular distribution and morphology.

Chapter 7

Publications, their content and own contribution

1. **Sandra Sefa**, D.C. Florian Wieland, Heike Helmholz, Berit Zeller-Plumhoff, Ann Wennerberg, Julian Moosmann, Regine Willumeit-Römer and Silvia Galli.
   "Assessing the long-term in vivo degradation behavior of magnesium alloys - a high resolution synchrotron radiation micro computed tomography study" in Frontiers Biomaterials Science. https://doi.org/10.3389/fbiom.2022.925471
   Abstract: Biodegradable magnesium (Mg) implants are emerging as a potential game changer in implant technology in situations where the implant temporarily supports the bone thereby avoiding secondary surgery for implant removal. However, the consequences of the alteration in the degradation rate to bone healing and the localization of degradation and alloying products in the long term remain unknown. In this study, we present the long-term osseointegration of three different biodegradable Mg alloys, Mg-10Gd, Mg-4Y-3RE and Mg-2Ag, which were implanted into rabbit femur for 6 and 9 months. In addition, we have investigated the effect of blood pre-incubation on the in vivo performance of the aforementioned alloys. Using high-resolution synchrotron radiation based micro computed tomography, the bone implant contact (BIC), bone volume fraction (BV/TV) and implant morphology were studied. The elemental traces have been characterized using micro X-ray fluorescence. Qualitative histological evaluation of the surrounding bone was also performed. Matured bone formed around all three implant types and Ca as well as P which represent parts of the degradation layer were in intimate contact with the bone. Blood pre-incubation prior to implantation significantly improved BIC in Mg-2Ag screws at 9 months. Despite different implant degradation morphologies pointing toward different degradation dynamics, Mg-10Gd, Mg-4Y-3RE and Mg-2Ag induced a similar long-term bone response based on our quantified parameters. Importantly, RE elements Gd and Y used in the alloys remained at the implantation site implying that they might be released later on or might persist in the implantation site forever. As the bone formation was not disturbed by their presence, it might be concluded that Gd and Y are non-deleterious. Consequently, we have shown that short and mid-term in vivo evaluations do not fully represent indicators for long-term osseointegration of Mg-based implants.
   Own contributions: Conceptualization, planning, data segmentation, workflow development, parameters evaluation, data analysis, data interpretation, writing of manuscript.

2. **Sandra Sefa**, Jonathan Espiritu, Hanna Ćwieka, Imke Greving, Silja Flenner, Olga Will, Susanne Beuer, D.C Florian Wieland, Regine Willumeit-Römer, Berit Zeller-Plumhoff.
   "Multiscale morphological analysis of bone microarchitecture around Mg-10Gd implants" in Bioactive Materials (2023). https://doi.org/10.1016/j.bioactmat.2023.07.017
   Abstract: The utilization of biodegradable magnesium (Mg)-based implants for restoration of bone function following trauma represents a transformative approach in orthopaedic application. One such alloy, magnesium-10wt.% gadolinium (Mg-10Gd), has been specifically developed to address the rapid degradation of Mg while enhancing its mechanical properties to promote bone healing. Previous studies have demonstrated that Mg-10Gd exhibits favorable osseointegration; however, it exhibits

distinct ultrastructural adaptation in comparison to conventional implants like titanium (Ti). A crucial aspect that remains unexplored is the impact of Mg-10Gd degradation on the bone microarchitecture. To address this, we employed hierarchical three-dimensional imaging using synchrotron radiation in conjunction with image-based finite element modelling. By using the methods outlined, the vascular porosity, lacunar porosity and the lacunar-canaliculi network (LCN) morphology of bone around Mg-10Gd in comparison to Ti in a rat model from 4 weeks to 20 weeks post-implantation was investigated. Our investigation revealed that within our observation period, the degradation of Mg-10Gd implants was associated with significantly lower ($p<0.05$) lacunar density in the surrounding bone, compared to Ti. Remarkably, the LCN morphology and the fluid flow analysis did not significantly differ for both implant types. In summary, a more pronounced lower lacunae distribution rather than their morphological changes was detected in the surrounding bone upon the degradation of Mg-10Gd implants. This implies potential disparities in bone remodelling rates when compared to Ti implants. Our findings shed light on the intricate relationship between Mg-10Gd degradation and bone microarchitecture, contributing to a deeper understanding of the implications for successful osseointegration.
Own contributions: Conceptual design of the experiments participation, planning, sample preparation, data acquisition (participation in beamtimes), data segmentation, writing scripts for parameter quantification, parameter analysis, evaluation of analysed parameters, interpretation of results, writing of manuscript.

3. Jonathan Espiritu, **Sandra Sefa**, Hanna Cwieka, Imke Greving, Silja Flenner, Regine Willumeit-Römer, Jan-Marten Seitz, Berit Zeller-Plumhoff.
“Detailing the influence of PEO-coated biodegradable Mg-based implants on the lacuno-canalicular network in sheep bone: A pilot study” in Bioactive Materials (2023). https://doi.org/10.1016/j.bioactmat.2023.02.018
Abstract: An increasing prevalence of bone-related injuries and aging geriatric populations continue to drive the orthopaedic implant market. A hierarchical analysis of bone remodelling after material implantation is necessary to better understand the relationship between implant and bone. Osteocytes, which are housed and communicate through the lacuno-canalicular network (LCN), are integral to bone health and remodelling processes. Therefore, it is essential to examine the framework of the LCN in response to implant materials or surface treatments. Biodegradable materials offer an alternative solution to permanent implants, which may require revision or removal surgeries. Magnesium alloys have resurfaced as promising materials due to their bone-like properties and safe degradation in vivo. To further tailor their degradation capabilities, surface treatments such as plasma electrolytic oxidation (PEO) have demonstrated to slow degradation. For the first time, the influence of a biodegradable material on the LCN is investigated by means of nondestructive 3D imaging. In this pilot study, we hypothesize noticeable variations in the LCN caused by altered chemical stimuli introduced by the PEO-coating. Utilising synchrotron-based transmission X-ray microscopy, we have characterised morphological LCN differences around uncoated and PEO-coated WE43 screws implanted into sheep bone. Bone specimens were explanted after 4, 8, and 12 weeks and regions near the implant surface were prepared for imaging. Findings from this investigation indicate that the slower degradation of PEO-coated WE43 induces healthier lacunar shapes within the LCN. However, the stimuli perceived by the uncoated material with higher degradation rates induces a greater connected LCN better prepared for bone disturbance.
Own contributions: Planning, conceptualization, sample preparation, data acquisition (participation in beamtimes), evaluation of analysis parameters, manuscript review.

4. Romy Marek, Hanna Cwieka, Nicholas Donohue, Patrick Holweg, Julian Moosmann, Felix Beckmann, Iva Brcic, Uwe Yacine Schwarze, Kamila Iskhakova, Marwa Chaabane, **Sandra Sefa**, Berit Zeller-Plumhoff, Annelie-Martina Weinberg, Regine Willumeit-Römer and Nicole Gabriele Sommer.
   "Degradation behavior and osseointegration of Mg–Zn–Ca screws in different bone regions of growing sheep: a pilot study" in Regenerative Biomaterials (2023). https://doi.org/10.1093/rb/rbac077
   Abstract: Magnesium (Mg)-based implants are highly attractive for the orthopedic field and may replace titanium (Ti) as support for fracture healing. To determine the implant–bone interaction in different bony regions, we implanted Mg-based alloy ZX00 (Mg < 0.5 Zn < 0.5 Ca, in wt%) and Ti-screws into the distal epiphysis and distal metaphysis of sheep tibiae. The implant degradation and osseointegration were assessed in vivo and ex vivo after 4, 6 and 12 weeks, using a combination of clinical computed tomography, medium-resolution micro computed tomography (mCT) and high-resolution synchrotron radiation mCT (SRmCT). Implant volume loss, gas formation and bone growth were evaluated for both implantation sites and each bone region independently. Additionally, histological analysis of bone growth was performed on embedded hard-tissue samples. We demonstrate that in all cases, the degradation rate of ZX00-implants ranges between 0.23 and 0.75mm/year. The highest degradation rates were found in the epiphysis. Bone-to-implant contact varied between the time points and bone types for both materials. Mostly, bone-volume-to-total-volume was higher around Ti-implants. However, we found an increased cortical thickness around the ZX00-screws when compared with the Ti-screws. Our results showed the suitability of ZX00-screws for implantation into the distal meta- and epiphysis.
   Own contributions: Data acquisition (participation in beamtimes), manuscript review.

5. Kamila Iskhakova, D.C. Florian Wieland, Romy Marek, Uwe Y. Schwarze, Hanna Cwieka, Tamadur AlBaraghtheh, Jan Reimers, Birte Hindenlang, **Sandra Sefa**, Annelie-Martina Weinberg, Regine Willumeit-Römer and Berit Zeller-Plumhoff.
   "Sheep bone ultrastructure analyses reveal differences in bone maturation around Mg-based and Ti implants" under review in Bioactive Materials.
   Abstract: Magnesium alloys among the biodegradable materials are one of the most convenient for bone fracture treatment due to their degradation rate as well as their biocompatibility and mechanical properties resembling the ones of bone. One of those alloys is ZX00 (Mg-0.45Zn-0.45Ca in wt.%), as the alloying elements Zn and Ca naturally appear in a body. The understanding of the influence of magnesium-based implants on the bone ultrastructure nevertheless still has blind spots. In this study, we present the first comparative analysis of the bone ultrastructure parameters around the ZX00 and Ti implants after 6, 12, and 24 weeks of healing depending on the distance from the implant surface. The mineralization was investigated revealing a significant decrease in the lattice spacing of the (002) Bragg's peak closer to the ZX00 implant in comparison to Ti, while no significant difference in the crystallite size was observed. The hydroxyapatite platelet thickness and osteon density demonstrated a decrease closer to the ZX00 implant interface. Thus, the results suggest the incorporation of Mg^{2+} ions into the bone ultrastructure, as well as, a lower degree of maturation of the bone in the presence of ZX00 implants than Ti.
   Own contributions: Data acquisition (participation in beamtimes), manuscript review.

6. Kamila Iskhakova, Hanna Cwieka, Svenja Meers, Heike Helmholz, Anton Davydok, Malte Storm, Ivo Matteo Baltruschat, Silvia Galli, Daniel Pröfrock, Olga Will, Mirko Gerle, Timo Damm, **Sandra Sefa,** Malte Soujon, Julian Moosmann, Florian Wieland, Berit Zeller-Plumhoff, Regine Willumeit-Römer.

“Effects of long-term implantation of Mg-xGd screws on bone micro- and ultrastructure, and element distribution” under review in Bioactive Materials (2023).

Abstract: Abstract Magnesium (Mg) – based alloys are becoming attractive materials for medical appplications as temporary bone implants for support of fracture healing. Due to their mechanical properties and biocompatibility they may replace titanium or stainless steel implants, commonly used in orthopedic field. Nevertheless, patient safety has to be assured by finding a long-term balance between metal degradation, osseointegration, bone ultrastructure adaptation and element distribution in organs. In order to determine the implant behavior and its influence on bone and tissues, we investigate two Mg alloys with gadolinium contents of 5 and 10 weight percent in comparison to permanent materials titanium and polyetheretherketone. The implants were present in rat tibia for 10, 20 and 32 weeks before sacrifice of the animal. Using X-ray-based micro and nanoscale imaging techniques, information about metal degradation and its influence on bone regeneration. Synchrotron radiation-based micro computed tomography enables the distinction of features like residual metal, degradation layer and bone structure. Additionally, X-ray diffraction and X-ray fluorescence yield information on parameters describing the bone ultrastructure and elemental composition at the bone-to-implant interface. Finally, with element specific mass spectrometry the elements and their accumulation in the main organs and tissues are traced. The results show the formation of a stable degradation layer, bone remodeling in the vicinity of an implant and no accumulation of Mg and Gd in selected organs. Thus, we confirm that Mg-xGd alloys are suitable choice of material for bone implants.

Own contribution: Data acquisition (participation in beamtimes), manuscript review.

Appendix A

Descriptive statistics

Table 1A: Summary of mean values with standard deviation of BIC and BV/TV within VOI 300 µm Mg-10Gd, Mg-4Y-3RE and Mg-2Ag explants after 6 and 9 months post-implantation as well as the volume of the remnant screws.

Parameter	Time point	Material	Mean ± std
BV/TV (%)	6	Mg-10Gd	47.92 ± 7.31
		Mg-4Y-3RE	46.81 ± 9.95
		Mg-2Ag	42.22 ± 18.08
	9	Mg-10Gd	31.12 ± 15.77
		Mg-4Y-3RE	43.57 ± 13.62
		Mg-2Ag	40.33 ± 11
BIC (%)	6	Mg-10Gd	57.60 ± 12.21
		Mg-4Y-3RE	44.49 ± 15.71
		Mg-2Ag	49.30 ± 13.55
	9	Mg-10Gd	54.75 ± 16.28
		Mg-4Y-3RE	51.73 ± 11.48
		Mg-2Ag	55.97 ± 15.93
Volume (mm^3)	6	Mg-10Gd	4.70 ± 0.20
		Mg-4Y-3RE	4.84 ± 0.33
		Mg-2Ag	2.33 ± 0.55
	9	Mg-10Gd	4.56 ± 0.46
		Mg-4Y-3RE	4.90 ± 0.28
		Mg-2Ag	1.40 ± 0.55

Table 1B: Summary of p values of BIC and BV/TV within VOI 300 µm Mg-10Gd, Mg-4Y-3RE and Mg-2Ag explants after 6 and 9 months post-implantation as well as the volume of the remnant screws.

Parameter	Time point (weeks)	Pairwise mean comparison among material type	p value
BV/TV (%)	6	Mg-4Y-3RE & Mg-10Gd	0.22
		Mg-2Ag & Mg-10Gd	0.72
		Mg-2Ag & Mg-4Y-3RE	0.81
	9	Mg-4Y-3RE & Mg-10Gd	0.28
		Mg-2Ag & Mg-10Gd	0.48
		Mg-2Ag & Mg-4Y-3RE	0.91
BIC (%)	6	Mg-4Y-3RE & Mg-10Gd	0.26
		Mg-2Ag & Mg-10Gd	0.57
		Mg-2Ag & Mg-4Y-3RE	0.82

	9	Mg-4Y-3RE & Mg-10Gd	0.93
		Mg-2Ag & Mg-10Gd	0.99
		Mg-2Ag & Mg-4Y-3RE	0.87
Volume (mm^3)	6	Mg-4Y-3RE & Mg-10Gd	0.72
		Mg-2Ag & Mg-10Gd	0*
		Mg-2Ag & Mg-4Y-3RE	0*
	9	Mg-4Y-3RE & Mg-10Gd	0.41
		Mg-2Ag & Mg-10Gd	0*
		Mg-2Ag & Mg-4Y-3RE	0*

Table 1C: Summary of mean values with their standard deviation as well as the p values of BIC and BV/TV of control and blood pre-incubated Mg-10Gd, Mg-4Y-3RE and Mg-2Ag obtained within VOI 300 μm^3 explants after 6 and 9 months post-implantation.

	Parameter	Time point	Treatment	Mean ± std	p value
Mg-10Gd	BV/TV (%)	6	Blood pre-incubated	44.54 ± 1.72	0.41
			Control	51.29 ± 9.83	
Mg-4Y-3RE			Blood pre-incubated	46.17 ± 5.15	0.92
			Control	47.44 ± 14.82	
Mg-2Ag			Blood pre-incubated	30.82 ± 7.39	0.04
			Control	53.62 ± 11.19	
Mg-10Gd		9	Blood pre-incubated	27.87 ± 5.53	0.21
			Control	29.28 ± 24.32	
Mg-4Y-3RE			Blood pre-incubated	42.41 ± 5.11	0.88
			Control	44.41 ± 5.11	
Mg-2Ag			Blood pre-incubated	33.34 ± 4.4	0.21
			Control	47.23 ± 10.34	
Mg-10Gd	BIC (%)	6	Blood pre-incubated	57.81 ± 19.03	0.97
			Control	57.39 ± 3.23	
Mg-4Y-3RE			Blood pre-incubated	44.66 ± 17.16	0.24
			Control	35.51 ± 15.49	
Mg-2Ag			Blood pre-incubated	53.90 ± 17.52	0.61
			Control	44.70 ± 9.41	
Mg-10Gd		9	Blood pre-incubated	52.76 ± 20.58	0.75
			Control	51.61 ±14.57	

Mg-4Y-3RE			Blood pre-incubated	51.86 ± 10.83	0.99
			Control	53.46 ± 11.64	
Mg-2Ag			Blood pre-incubated	69.53 ± 6.54	0.04
			Control	42.40 ± 6.28	

Table 2A. Vascular number density (N.Vs/BV) and lacunar number density (N.Lc/BV) parameters calculated for Mg-10Gd and Ti (200 µm from the screw) at 4, 8 and 12 weeks post-implantation (3D) and at 10 and 20 weeks post-implantation (2D). * means the group means are significantly different.

Parameter	Time point (Weeks)	Material	Mean ± std	p value
N.Lc /BV (mm^{-3})	4	Mg-10Gd	22,128 ± 4,298	
		Ti	49,636. 8 ± 14,697	0.004*
	8	Mg-10Gd	24,449.4 ± 6,938	
		Ti	52,385 ± 5,283	0.0001*
	12	Mg-10Gd	17,342.9 ± 11,652	
		Ti	71,433.8 ± 13,454	0.0001*
N.Vs/BV (mm^{-3})	4	Mg-10Gd	2,981 ± 716	
		Ti	3,235 ± 1,091	0.67
	8	Mg-10Gd	3,035 ± 839	
		Ti	2,021 ± 370	0.04*
	12	Mg-10Gd	1,906 ± 390	
		Ti	2,381 ± 395	0.09
N.Lc/BA	10	Mg-10Gd	606.2 ± 115.9	0.20
		Ti	490.6 ± 111.9	
	20	Mg-10Gd	450.2 ± 63.1	0.07
		Ti	627.7 ± 183.5	
N.Vs/BA	10	Mg-10Gd	32.4 ± 8.2	0.65
		Ti	36.3 ± 13.9	
	20	Mg-10Gd	26.0 ± 8.9	0.15
		Ti	35.10 ± 9.2	

Table 2B. Vascular number density (N.Vs/BV) and lacunar number density (N.Lc/BV) parameters calculated for Mg-10Gd and Ti (500 µm from the screw) at 4, 8 and 12 weeks post-implantation (3D) and at 10 and 20 weeks post-implantation (2D). * means the group means are significantly different.

Parameter	Time point (Weeks)	Material	Mean ± std	p value
N.Lc /BV (mm^{-3})	4	Mg-10Gd	24,494 ± 6,384	0.002*
		Ti	51,911 ± 12,142	
	8	Mg-10Gd	23,162 ± 6,470	0.00007*
		Ti	52,941 ± 6,143	
	12	Mg-10Gd	15, 795 ± 12,610	0.0004*
		Ti	68,180 ± 15,501	
N.Vs/BV (mm^{-3})	4	Mg-10Gd	2,636 ± 404	0.56
		Ti	2,873 ± 759	
	8	Mg-10Gd	2,427 ± 571	0.05
		Ti	1,785 ± 283	
	12	Mg-10Gd	1,570 ± 3,670	0.08
		Ti	1,964 ± 241	
N.Lc/BA	10	Mg-10Gd	637 ± 109	0.17
		Ti	486 ± 123	
	20	Mg-10Gd	446.78 ± 25.14	0.01*
		Ti	578.87 ± 85.99	
N.Vs/BA	10	Mg-10Gd	38.24 ± 4.82	0.75
		Ti	40.67 ± 13.97	
	20	Mg-10Gd	25.55 ± 9.13	0.34
		Ti	33.33 ± 5.12	

Table 3A. Lacunar morphometric parameters calculated for Mg-10Gd, Ti and control bone specimens at 10 and 20 weeks post-implantation. Calculated parameters include lacunar volume (Lc.V), lacunar surface area (Lc.SA) and LCN porosity (LCN.TV/BV).

Parameter	Time point (weeks)	Material	Mean ± std
		Mg-10Gd	310.6 ± 93.9

Lc.SA (μm^2)	10	Ti	289.1 ± 113.9
		Control	231.1 ± 24.0
	20	Mg-10Gd	237.0 ± 60.9
		Ti	270.8 ± 91.8
		Control	187.6 ± 48.0
Lc.V (μm^3)	10	Mg-10Gd	284.3 ± 118.1
		Ti	226.7 ± 75.5
		Control	198.1 ± 25.5
	20	Mg-10Gd	214.4 ± 88.2
		Ti	236.9 ± 88.8
		Control	146.4 ± 59.9
LCN.TV/BV (%)	10	Mg-10Gd	6.99 ± 2.43
		Ti	5.35 ± 2.08
		Control	5.44 ± 1.54
	20	Mg-10Gd	4.35 ± 2.29
		Ti	5.14 ± 1.81
		Control	3.10 ± 1.43

Table 3B: P values of lacunar morphometric parameters calculated for Mg-10Gd, Ti and control bone specimens at 10 and 20 weeks post-implantation. Calculated parameters include lacunar volume (Lc.V), lacunar surface area (Lc.SA), and LCN porosity (LCN. TV/BV).

Parameter	Time point (weeks)	Pairwise mean comparison among material type	p value
Lc.SA (μm^2)	10	Mg-10Gd & Ti	0.89
		Mg-10Gd & Control	0.38
		Control & Ti	0.59
	20	Mg-10Gd & Ti	0.56
		Mg-10Gd & Control	0.45
		Control & Ti	0.12
Lc.V (μm^3)	10	Mg-10Gd & Ti	0.43
		Mg-10Gd & Control	0.29
		Control & Ti	0.86

	20	Mg-10Gd & Ti	0.82
		Mg-10Gd & Control	0.32
		Control & Ti	0.14
LCN.TV/BV (%)	10	Mg-10Gd & Ti	0.3
		Mg-10Gd & Control	0.48
		Control & Ti	0.99
	20	Mg-10Gd & Ti	0.65
		Mg-10Gd & Control	0.48
		Control & Ti	0.16

Table 4A: Canaliculi morphological descriptors calculated for Mg-10Gd, Ti and control bone specimens at 10 and 20 weeks post-implantation. Calculated parameters were canaliculi surface area (Ca.SA), canaliculi volume (Ca.V), canaliculi junction density (Ca.Nodes / BV), canaliculi areal density (N.Ca / Lc.SA), pressure and velocity.

Parameter	Time point (weeks)	Material	Mean ± std
Ca.SA	10	Mg-10Gd	7.59 ± 2.61
		Ti	6.18 ± 3.54
		Control	5.69 ± 1.71
	20	Mg-10Gd	5.13 ± 2.91
		Ti	5.10 ± 2.71
		Control	4.38 ± 0.54
Ca.V	10	Mg-10Gd	0.76 ± 0.31
		Ti	0.63 ± 0.28
		Control	0.48 ± 0.15
	20	Mg-10Gd	0.42 ± 0.26
		Ti	0.47 ± 0.27
		Control	0.24 ± 0.12
Ca.Nodes/BV (μm^{-3})	10	Mg-10Gd	0.16 ± 0.09
		Ti	0.12 ± 0.08
		Control	0.15 ± 0.06

	20	Mg-10Gd	0.14 ± 0.04
		Ti	0.13 ± 0.06
		Control	0.09 ± 0.04
N.Ca/Lc.SA (μm^{-2})	10	Mg-10Gd	1.81 ± 0.96
		Ti	1.86 ± 1.49
		Control	2.96 ± 1.76
	20	Mg-10Gd	4.85 ± 3.80
		Ti	1.62 ± 1.30
		Control	3.49 ± 1.00
Pressure (Pa/ μm^3)	10	Mg-10Gd	54.53 ± 55.02
		Ti	36.07 ± 31.06
		Control	30.42 ± 45.52
	20	Mg-10Gd	22.10 ± 19.13
		Ti	25.05 ± 15.97
		Control	15.91 ± 6.97
Velocity (μm^{-3} /s/μm^3)	10	Mg-10Gd	2.4 ± 3.1
		Ti	5.6 ± 10.0
		Control	5.2 ± 10.0
	20	Mg-10Gd	0.96 ± 0.98
		Ti	3.2 ± 5.4
		Control	0.56 ± 0.43

Table 4B: P values of canaliculi morphological descriptors calculated for Mg-10Gd, Ti and control bone specimens at 10 and 20 weeks post-implantation. Calculated parameters were canaliculi surface area (Ca.SA), canaliculi volume (Ca.V), canaliculi junction density (Ca.Nodes/BV), canaliculi areal density (N.Ca/Lc.SA), pressure and velocity. * means the group means are significantly different.

Parameter	Time point (weeks)	Pairwise mean comparison among material type	p value
	10	Mg-10Gd & Ti	0.6
		Control & Mg-10Gd	0.55
		Control & Ti	0.96

Ca.SA	20	Mg-10Gd & Ti	0.99
		Control & Mg-10Gd	0.85
		Control & Ti	0.86
Ca.V	10	Mg-10Gd & Ti	0.58
		Control & Mg-10Gd	0.25
		Control & Ti	0.69
	20	Mg-10Gd & Ti	0.86
		Control & Mg-10Gd	0.40
		Control & Ti	0.21
Ca.Nodes/BV (μm^{-3})	10	Mg-10Gd & Ti	0.64
		Control & Mg-10Gd	0.99
		Control & Ti	0.85
	20	Mg-10Gd & Ti	0.82
		Control & Mg-10Gd	0.14
		Control & Ti	0.31
N.Ca/Lc.SA (μm^{-2})	10	Mg-10Gd & Ti	0.99
		Control & Mg-10Gd	0.40
		Control & Ti	0.40
	20	Mg-10Gd & Ti	0.03 *
		Control & Mg-10Gd	0.61
		Control & Ti	0.40
Pressure ($Pa/\mu m^3$)	10	Mg-10Gd & Ti	0.69
		Control & Mg-10Gd	0.66
		Control & Ti	0.98
	20	Mg-10Gd & Ti	0.92
		Control & Mg-10Gd	0.80
		Control & Ti	0.63
Velocity ($\mu m/s/\mu m^3$)	10	Mg-10Gd & Ti	0.70
		Control & Mg-10Gd	0.83
		Control & Ti	0.99

	20	Mg-10Gd & Ti	0.36
		Control & Mg-10Gd	0.98
		Control & Ti	0.44

Table 5: LCN morphological descriptors calculated for the trabecular and cortical interfacial bone of Mg-10Gd and Ti implants at 10 and 20 weeks post-implantation. Calculated parameters were lacunar volume (Lc.V), lacunar surface area (Lc.SA), canaliculi volume (Ca.V), canaliculi surface area (Ca.SA). * means the group means are significantly different.

Parameter	Time Point (Weeks)	material	Bone type	Mean ± std	P value
Lc.V (μm^3)	10	Mg-10Gd	Trabecular	195.6 ± 17.1	0.02*
			Cortical	372.9 ± 106.3	
		Ti	Trabecular	200.6 ± 79.2	0.37
			Cortical	252.4 ± 72.1	
	20	Mg-10Gd	Trabecular	200.6 ± 79.2	0.40
			Cortical	252.9 ± 72.1	
		Ti	Trabecular	241.2 ± 100.3	0.89
			Cortical	232.6± 87.5	
Lc.SA (μm^2)	10	Mg-10Gd	Trabecular	240.52 ± 19.98	0.02*
			Cortical	380.6 ± 84.4	
		Ti	Trabecular	279.3 ± 151.3	0.83
			Cortical	151.3 ± 83.0	
	20	Mg-10Gd	Trabecular	248.9 ± 81.0	0.70
			Cortical	225.0 ± 37.7	
		Ti	Trabecular	278.8 ± 111.7	0.80
			Cortical	262.9 ± 79.4	
Ca.V (μm^3)	10	Mg-10Gd	Trabecular	0.88 ± 0.41	0.37
			Cortical	0.66 ± 0.18	
		Ti	Trabecular	0.52 ± 0.30	0.33
			Cortical	0.73 ± 0.26	
	20	Mg-10Gd	Trabecular	0.40 ± 0.20	0.80
			Cortical	0.44 ± 0.32	

		Ti	Trabecular	0.56 ± 0.30	0.78
			Cortical	0.37 ± 0.29	
Ca.SA (μm^2)	10	Mg-10Gd	Trabecular	7.43 ± 2.47	0.87
			Cortical	7.76 ± 3.11	
		Ti	Trabecular	4.00 ± 2.86	0.08
			Cortical	8.35 ± 2.89	
	20	Mg-10Gd	Trabecular	4.96 ± 2.40	0.86
			Cortical	5.30 ± 3.60	
		Ti	Trabecular	5.95 ± 2.50	0.94
			Cortical	4.25 ± 2.89	

Table 6: Regression statistics on degradation rate and BV/TV of data obtained from Krüger *et al*.[14] (4,8 and 12 weeks post-implantation) and Iskhakova *et al*.[15] (10, 20 and 32 weeks post-implantation). * means significant

Correlation between BV/TV and degradation rate	R	Slope	P value (Slope)	Intercept	P value (Intercept)
Negative	0.89	-40.71	0.016*	50.95	0.0001*

Bibliography

1. Willbold, E., Gu, X., Albert, D., Kalla, K., Bobe, K., Brauneis, M., Janning, C., Nellesen, J., Czayka, W., Tillmann, W., et al. (2015). Effect of the addition of low rare earth elements (lanthanum, neodymium, cerium) on the biodegradation and biocompatibility of magnesium. Acta Biomaterialia *11*, 554–562. 10.1016/j.actbio.2014.09.041.

2. Witte, F. (2010). The history of biodegradable magnesium implants: A review☆. Acta Biomaterialia *6*, 1680–1692. 10.1016/j.actbio.2010.02.028.

3. Gu, X.-N., and Zheng, Y.-F. (2010). A review on magnesium alloys as biodegradable materials. Front. Mater. Sci. China *4*, 111–115. 10.1007/s11706-010-0024-1.

4. Persaud-Sharma, D., and McGoron, A. (2012). Biodegradable Magnesium Alloys: A Review of Material Development and Applications. JBBTE *12*, 25–39. 10.4028/www.scientific.net/JBBTE.12.25.

5. Seal, C.K., Vince, K., and Hodgson, M.A. (2009). Biodegradable surgical implants based on magnesium alloys – A review of current research. IOP Conf. Ser.: Mater. Sci. Eng. *4*, 012011. 10.1088/1757-899X/4/1/012011.

6. Staiger, M.P., Pietak, A.M., Huadmai, J., and Dias, G. (2006). Magnesium and its alloys as orthopedic biomaterials: A review. Biomaterials *27*, 1728–1734. 10.1016/j.biomaterials.2005.10.003.

7. KYOCERA SGS Precision Tools Europe Limited Titanium Properties. Titanium Properties.

8. Civil's Guide (2021). What is the Young's Modulus of Steel?

9. Agrawal, C.M. (1998). Reconstructing the human body using biomaterials. JOM *50*, 31–35. 10.1007/s11837-998-0064-5.

10. Nagels, J., Stokdijk, M., and Rozing, P.M. (2003). Stress shielding and bone resorption in shoulder arthroplasty. Journal of Shoulder and Elbow Surgery *12*, 35–39. 10.1067/mse.2003.22.

11. Jiao, J., Zhang, S., Qu, X., and Yue, B. (2021). Recent Advances in Research on Antibacterial Metals and Alloys as Implant Materials. Front. Cell. Infect. Microbiol. *11*, 693939. 10.3389/fcimb.2021.693939.

12. Li, H., Wang, P., Lin, G., and Huang, J. (2021). The role of rare earth elements in biodegradable metals: A review. Acta Biomaterialia *129*, 33–42. 10.1016/j.actbio.2021.05.014.

13. Galli Silvia (2016). On magnesium-containing implants for bone applications. Mälmo University, Faculty of Odontology.

14. Krüger, D., Galli, S., Zeller-Plumhoff, B., Wieland, D.C.F., Peruzzi, N., Wiese, B., Heuser, P., Moosmann, J., Wennerberg, A., and Willumeit-Römer, R. (2022). High-resolution ex vivo analysis of the degradation and osseointegration of Mg-xGd implant screws in 3D. Bioactive Materials *13*, 37–52. 10.1016/j.bioactmat.2021.10.041.

15. Iskhakova, Kamila, Cwieka, Hanna, Meers, Svenja, Helmholz, Heike, Davydok, Anton, Storm, Malte, Baltruschat, Ivo Matteo, Galli, Silvia, Profrock, Daniel, Will, Olga, et

al. Effects of long-term implantation of Mg-xGd screws on bone micro- and ultrastructure, and element distribution. Bioactive materials.

16. Zeller-Plumhoff, B., Malich, C., Krüger, D., Campbell, G., Wiese, B., Galli, S., Wennerberg, A., Willumeit-Römer, R., and Wieland, D.C.F. (2020). Analysis of the bone ultrastructure around biodegradable Mg–xGd implants using small angle X-ray scattering and X-ray diffraction. Acta Biomaterialia *101*, 637–645. 10.1016/j.actbio.2019.11.030.

17. Espiritu, J., Sefa, S., Ćwieka, H., Greving, I., Flenner, S., Willumeit-Römer, R., Seitz, J.-M., and Zeller-Plumhoff, B. (2023). Detailing the influence of PEO-coated biodegradable Mg-based implants on the lacuno-canalicular network in sheep bone: A pilot study. Bioactive Materials *26*, 14–23. 10.1016/j.bioactmat.2023.02.018.

18. Sefa, S., Wieland, D.C.F., Helmholz, H., Zeller-Plumhoff, B., Wennerberg, A., Moosmann, J., Willumeit-Römer, R., and Galli, S. (2022). Assessing the long-term in vivo degradation behavior of magnesium alloys - a high resolution synchrotron radiation micro computed tomography study. Front. Biomater. Sci. *1*, 925471. 10.3389/fbiom.2022.925471.

19. Sefa, S., Espiritu, J., Ćwieka, H., Greving, I., Flenner, S., Will, O., Beuer, S., Wieland, D.C.F., Willumeit-Römer, R., and Zeller-Plumhoff, B. (2023). Multiscale morphological analysis of bone microarchitecture around Mg-10Gd implants. Bioactive Materials *30*, 154–168. 10.1016/j.bioactmat.2023.07.017.

20. Donald Whedon and Proulx Robert (2023). Bone. Encyclopedia Britannica. https://www.britannica.com/science/bone-anatomy.

21. Biga Lindsay, Dawson Sierra, Harwell Amy, Hopkins Robin, Kaufmann Joel, LeMaster Mike, Matern Philip, Morrison-Graham Katie, Quick Devon, and Runyeon Jon (2023). Anatomy & Physiology (OpenStax/Oregon State University).

22. Ramachandran Ramnath (2006). Hierachy of bone structure.

23. Schaffler, M.B., Cheung, W.-Y., Majeska, R., and Kennedy, O. (2014). Osteocytes: Master Orchestrators of Bone. Calcif Tissue Int *94*, 5–24. 10.1007/s00223-013-9790-y.

24. Zimmermann, E.A., Schaible, E., Gludovatz, B., Schmidt, F.N., Riedel, C., Krause, M., Vettorazzi, E., Acevedo, C., Hahn, M., Püschel, K., et al. (2016). Intrinsic mechanical behavior of femoral cortical bone in young, osteoporotic and bisphosphonate-treated individuals in low- and high energy fracture conditions. Sci Rep *6*, 21072. 10.1038/srep21072.

25. Cardoso, L., Fritton, S.P., Gailani, G., Benalla, M., and Cowin, S.C. (2013). Advances in assessment of bone porosity, permeability and interstitial fluid flow. Journal of Biomechanics *46*, 253–265. 10.1016/j.jbiomech.2012.10.025.

26. Neuman, W.F., and Mulryan, B.J. (1952). The surface chemistry of bone. Journal of Biological Chemistry *195*, 843–848. 10.1016/S0021-9258(18)55795-1.

27. Cowin, S.C. (1999). Bone poroelasticity. Journal of Biomechanics *32*, 217–238. 10.1016/S0021-9290(98)00161-4.

28. Sharma, D., Ciani, C., Marin, P.A.R., Levy, J.D., Doty, S.B., and Fritton, S.P. (2012). Alterations in the osteocyte lacunar–canalicular microenvironment due to estrogen deficiency. Bone *51*, 488–497. 10.1016/j.bone.2012.05.014.

29. Tommasini, S.M., Trinward, A., Acerbo, A.S., De Carlo, F., Miller, L.M., and Judex, S. (2012). Changes in intracortical microporosities induced by pharmaceutical treatment of osteoporosis as detected by high resolution micro-CT. Bone *50*, 596–604. 10.1016/j.bone.2011.12.012.

30. Hannah, K.M., Thomas, C.D.L., Clement, J.G., De Carlo, F., and Peele, A.G. (2010). Bimodal distribution of osteocyte lacunar size in the human femoral cortex as revealed by micro-CT. Bone *47*, 866–871. 10.1016/j.bone.2010.07.025.

31. Carter, Y., Thomas, C.D.L., Clement, J.G., Peele, A.G., Hannah, K., and Cooper, D.M.L. (2013). Variation in osteocyte lacunar morphology and density in the human femur — a synchrotron radiation micro-CT study. Bone *52*, 126–132. 10.1016/j.bone.2012.09.010.

32. McCreadie, B.R., Hollister, S.J., Schaffler, M.B., and Goldstein, S.A. (2004). Osteocyte lacuna size and shape in women with and without osteoporotic fracture. Journal of Biomechanics *37*, 563–572. 10.1016/S0021-9290(03)00287-2.

33. Sugawara, Y., Kamioka, H., Honjo, T., Tezuka, K., and Takanoyamamoto, T. (2005). Three-dimensional reconstruction of chick calvarial osteocytes and their cell processes using confocal microscopy. Bone *36*, 877–883. 10.1016/j.bone.2004.10.008.

34. Vatsa, A., Breuls, R.G., Semeins, C.M., Salmon, P.L., Smit, T.H., and Klein-Nulend, J. (2008). Osteocyte morphology in fibula and calvaria — Is there a role for mechanosensing? Bone *43*, 452–458. 10.1016/j.bone.2008.01.030.

35. Lin, Y., and Xu, S. (2011). AFM analysis of the lacunar-canalicular network in demineralized compact bone: AFM for 3d tissue nanostructure. Journal of Microscopy *241*, 291–302. 10.1111/j.1365-2818.2010.03431.x.

36. Marotti, G., Ferretti, M., Remaggi, F., and Palumbo, C. (1995). Quantitative evaluation on osteocyte canalicular density in human secondary osteons. Bone *16*, 125–128. 10.1016/8756-3282(95)80022-I.

37. Schneider, P., Meier, M., Wepf, R., and Müller, R. (2011). Serial FIB/SEM imaging for quantitative 3D assessment of the osteocyte lacuno-canalicular network. Bone *49*, 304–311. 10.1016/j.bone.2011.04.005.

38. Carriero, A., Doube, M., Vogt, M., Busse, B., Zustin, J., Levchuk, A., Schneider, P., Müller, R., and Shefelbine, S.J. (2014). Altered lacunar and vascular porosity in osteogenesis imperfecta mouse bone as revealed by synchrotron tomography contributes to bone fragility. Bone *61*, 116–124. 10.1016/j.bone.2013.12.020.

39. Weinbaum, S., Cowin, S.C., and Zeng, Y. (1994). A model for the excitation of osteocytes by mechanical loading-induced bone fluid shear stresses. Journal of Biomechanics *27*, 339–360. 10.1016/0021-9290(94)90010-8.

40. Palacio-Mancheno, P.E., Larriera, A.I., Doty, S.B., Cardoso, L., and Fritton, S.P. (2014). 3D Assessment of Cortical Bone Porosity and Tissue Mineral Density Using High-Resolution µCT: Effects of Resolution and Threshold Method: 3D assessment of cortical bone porosity and tmd using high-resolution µCT. J Bone Miner Res *29*, 142–150. 10.1002/jbmr.2012.

41. Mishra, S., and Knothe Tate, M.L. (2003). Effect of lacunocanalicular architecture on hydraulic conductance in bone tissue: Implications for bone health and evolution. Anat. Rec. *273A*, 752–762. 10.1002/ar.a.10079.

42. Osborn JF and Newesely H (1980). Dynamic aspects of the implant-bone interface. In: Heimke G, ed. Dental implants: materials and systems. München: Carl Hanser Verlag, 111–123.

43. Roberts, W. (1988). Bone tissue interface. Journal of Dental Education *52*, 804–809. 10.1002/j.0022-0337.1988.52.12.tb02283.x.

44. Davies, J.E. (2003). Understanding Peri-Implant Endosseous Healing. Journal of Dental Education *67*, 932–949. 10.1002/j.0022-0337.2003.67.8.tb03681.x.

45. Puleo, D. (1999). Understanding and controlling the bone–implant interface. Biomaterials *20*, 2311–2321. 10.1016/S0142-9612(99)00160-X.

46. Listgarten, M.A. (1996). Soft and hard tissue response to endosseous dental implants. Anat. Rec. *245*, 410–425. 10.1002/(SICI)1097-0185(199606)245:2<410::AID-AR20>3.0.CO;2-R.

47. Linder, L., Obrant, K., and Boivin, G. (1989). Osseointegration of metallic implants: II. Transmission electron microscopy in the rabbit. Acta Orthopaedica Scandinavica *60*, 135–139. 10.3109/17453678909149240.

48. Meyer, U., Joos, U., Mythili, J., Stamm, T., Hohoff, A., Fillies, T., Stratmann, U., and Wiesmann, H.P. (2004). Ultrastructural characterization of the implant/bone interface of immediately loaded dental implants. Biomaterials *25*, 1959–1967. 10.1016/j.biomaterials.2003.08.070.

49. Shah, F.A., Thomsen, P., and Palmquist, A. (2018). A Review of the Impact of Implant Biomaterials on Osteocytes. J Dent Res *97*, 977–986. 10.1177/0022034518778033.

50. Brunski, J.B. (1999). In Vivo Bone Response to Biomechanical Loading at the Bone/Dental-Implant Interface. Adv Dent Res. *13*, 99–119. 10.1177/08959374990130012301.

51. Qing, H., and Bonewald, L.F. (2009). Osteocyte Remodeling of the Perilacunar and Pericanalicular Matrix. Int J Oral Sci *1*, 59–65. 10.4248/ijos.09019.

52. Shah, F.A. (2017). Osteocytes as indicators of bone quality - multiscale structure-composition characterisation of the bone-implant interface.

53. Klein-Nulend, J., Bakker, A.D., Bacabac, R.G., Vatsa, A., and Weinbaum, S. (2013). Mechanosensation and transduction in osteocytes. Bone *54*, 182–190. 10.1016/j.bone.2012.10.013.

54. Zhang, D., Weinbaum, S., and Cowin, S.C. (1998). Electrical Signal Transmission in a Bone Cell Network: The Influence of a Discrete Gap Junction. Annals of Biomedical Engineering *26*, 644–659. 10.1114/1.123.

55. Gardinier, J.D., Townend, C.W., Jen, K.-P., Wu, Q., Duncan, R.L., and Wang, L. (2010). In situ permeability measurement of the mammalian lacunar–canalicular system. Bone *46*, 1075–1081. 10.1016/j.bone.2010.01.371.

56. Klein-Nulend, J., Van Der Plas, A., Semeins, C.M., Ajubi, N.E., Erangos, J.A., Nijweide, P.J., and Burger, E.H. (1995). Sensitivity of osteocytes to biomechanical stress in vitro. FASEB j. *9*, 441–445. 10.1096/fasebj.9.5.7896017.

57. Du, Z., Ivanovski, S., Hamlet, S.M., Feng, J.Q., and Xiao, Y. (2016). The Ultrastructural Relationship Between Osteocytes and Dental Implants Following Osseointegration: Osteocytes and Dental Implants. Clinical Implant Dentistry and Related Research *18*, 270–280. 10.1111/cid.12257.

58. Du, Z., Xiao, Y., Hashimi, S., Hamlet, S.M., and Ivanovski, S. (2016). The effects of implant topography on osseointegration under estrogen deficiency induced osteoporotic conditions: Histomorphometric, transcriptional and ultrastructural analysis. Acta Biomaterialia *42*, 351–363. 10.1016/j.actbio.2016.06.035.

59. Shah, F.A., Snis, A., Matic, A., Thomsen, P., and Palmquist, A. (2016). 3D printed Ti6Al4V implant surface promotes bone maturation and retains a higher density of less aged osteocytes at the bone-implant interface. Acta Biomaterialia *30*, 357–367. 10.1016/j.actbio.2015.11.013.

60. Glasdam, S.-M., Glasdam, S., and Peters, G.H. (2016). The Importance of Magnesium in the Human Body:A systematic literature review. In Advances in Clinical Chemistry (Elsevier), pp. 169–193. 10.1016/bs.acc.2015.10.002.

61. Gröber, U., Schmidt, J., and Kisters, K. (2015). Magnesium in Prevention and Therapy. Nutrients *7*, 8199–8226. 10.3390/nu7095388.

62. Ross Catherine, Caballero Benjamin, Cousins Robert, Tucker Katherine, and Ziegler Thomas Modern nutrition in health and disease: Eleventh edition 11th ed. (Wolters Kluwer Health Adis (ESP)).

63. Tibbetts, D.M., and Aub, J.C. (1937). Magnesium Metabolism in health and disease. III. in exophthalmic goiter, basophilic adenoma, Addisons's disease and steatorrhea. J. Clin. Invest. *16*, 511–515. 10.1172/JCI100876.

64. Zamboni, C.B., Oliveira, L.C., Kovacs, L., and Metairon, S. (2012). Ca and Mg determination from inhabitants of Brazil using neutron activation analysis. J Radioanal Nucl Chem *291*, 389–393. 10.1007/s10967-011-1263-z.

65. Yang, S.J., Hwang, S.Y., Baik, S.H., Lee, K.W., Nam, M.S., Park, Y.S., Woo, J.T., Kim, Y.S., Park, S., Park, S.-Y., et al. (2014). Serum Magnesium Level Is Associated with Type 2 Diabetes in Women with a History of Gestational Diabetes Mellitus: The Korea National Diabetes Program Study. J Korean Med Sci *29*, 84. 10.3346/jkms.2014.29.1.84.

66. Barbagallo, M., and Dominguez, L.J. (2007). Magnesium metabolism in type 2 diabetes mellitus, metabolic syndrome and insulin resistance. Archives of Biochemistry and Biophysics *458*, 40–47. 10.1016/j.abb.2006.05.007.

67. Huse EC (1878). A new ligature? The Chigago Medical Journal and Examiner *37*, 172–2.

68. Payr Edward (1900). Beiträge zur Technik der Blutgefäss- und Nervennaht nebst Mittheilungen über die Verwendung eines resorbirbaren Metalles in der Chirugie. Arch Klin Chir *62*, 67–93.

69. Payr Edward (1901). Blutgefäß- und Nervennaht (nebst Mittheilung über die Verwendung eines resorbirbaren Metalles in der Chirurgie). Centralblatt für Chirurgie *28(Beilage: Bericht über die verhandlungen der deutschen Gesellschaft für Chirurgie, XXIX Kongress, abgehalten vom 18.-21. April 1900 im Langenbeck-Hause)*, 31–37.

70. Lambotte A (1909). Technique et indications de la prothèse perdue dans la traitement des fractures. Presse Med Belge *17*, 321–322.

71. Stone P and Lord J.W (1951). An experimental study of the thrombogenic properties of magnesium and magnesium-aluminum wire in the dog's aorta. Surgery *30*, 987–993.

72. Verbrugge J (1934). Le matériel métallique résorbable en chirurgie osseuse. Presse Med *23*, 460–465.

73. Kuehn, K.-D., Ege, W., and Gopp, U. (2005). Acrylic bone cements: mechanical and physical properties. Orthopedic Clinics of North America *36*, 29–39. 10.1016/j.ocl.2004.06.011.

74. Rostami Niloufar (2014). Development of novel magnesium phosphate bone cement.

75. Biel, A., Chaudhry, M., Gustafsson, S., and Nygren, H. (2016). The Use of MgO-paste as a Biodegradeable Bone Cement. Materials Today: Proceedings *3*, 556–561. 10.1016/j.matpr.2016.01.090.

76. Sehlke, B.M., Wilson, T.G., Jones, A.A., Yamashita, M., and Cochran, D.L. (2013). The Use of a Magnesium-Based Bone Cement to Secure Immediate Dental Implants. Int J Oral Maxillofac Implants *28*, e357–e367. 10.11607/jomi.te16.

77. Gulotta, L.V., Kovacevic, D., Ying, L., Ehteshami, J.R., Montgomery, S., and Rodeo, S.A. (2008). Augmentation of Tendon-to-Bone Healing with a Magnesium-Based Bone Adhesive. Am J Sports Med *36*, 1290–1297. 10.1177/0363546508314396.

78. Thomopoulos, S., Zampiakis, E., Das, R., Kim, H.M., Silva, M.J., Havlioglu, N., and Gelberman, R.H. (2009). Use of a Magnesium-Based Bone Adhesive for Flexor Tendon-to-Bone Healing. The Journal of Hand Surgery *34*, 1066–1073. 10.1016/j.jhsa.2009.04.018.

79. Schendel, S.A., and Peauroi, J. (2009). Magnesium-Based Bone Cement and Bone Void Filler: Preliminary Experimental Studies. Journal of Craniofacial Surgery *20*, 461–464. 10.1097/SCS.0b013e31819b9819.

80. Cheng, M., Wahafu, T., Jiang, G., Liu, W., Qiao, Y., Peng, X., Cheng, T., Zhang, X., He, G., and Liu, X. (2016). A novel open-porous magnesium scaffold with controllable microstructures and properties for bone regeneration. Sci Rep *6*, 24134. 10.1038/srep24134.

81. Witte, F., Ulrich, H., Rudert, M., and Willbold, E. (2007). Biodegradable magnesium scaffolds: Part 1: Appropriate inflammatory response. J. Biomed. Mater. Res. *81A*, 748–756. 10.1002/jbm.a.31170.

82. Witte, F., Ulrich, H., Palm, C., and Willbold, E. (2007). Biodegradable magnesium scaffolds: Part II: Peri-implant bone remodeling. J. Biomed. Mater. Res. *81A*, 757–765. 10.1002/jbm.a.31293.

83. Böstman, O. (1994). Economic Considerations on Avoiding Implant Removals after Fracture Fixation by Using Absorbable Devices. Scandinavian Journal of Social Medicine *22*, 41–45. 10.1177/140349489402200107.

84. Kose Ozkan (2019). Magnesium (MgYREZr) bioabsorbable screws in orthopedic surgery. Military Medicine Worldwide.

85. Lee, J.-W., Han, H.-S., Han, K.-J., Park, J., Jeon, H., Ok, M.-R., Seok, H.-K., Ahn, J.-P., Lee, K.E., Lee, D.-H., et al. (2016). Long-term clinical study and multiscale analysis of in vivo biodegradation mechanism of Mg alloy. Proc. Natl. Acad. Sci. U.S.A. *113*, 716–721. 10.1073/pnas.1518238113.

86. Windhagen, H., Radtke, K., Weizbauer, A., Diekmann, J., Noll, Y., Kreimeyer, U., Schavan, R., Stukenborg-Colsman, C., and Waizy, H. (2013). Biodegradable magnesium-based screw clinically equivalent to titanium screw in hallux valgus surgery: short term results of the first prospective, randomized, controlled clinical pilot study. BioMed Eng OnLine *12*, 62. 10.1186/1475-925X-12-62.

87. Waizy, H., Seitz, J.-M., Reifenrath, J., Weizbauer, A., Bach, F.-W., Meyer-Lindenberg, A., Denkena, B., and Windhagen, H. (2013). Biodegradable magnesium implants for orthopedic applications. J Mater Sci *48*, 39–50. 10.1007/s10853-012-6572-2.

88. Daentzer, D., Willbold, E., Kalla, K., Bartsch, I., Masalha, W., Hallbaum, M., Hurschler, C., Kauth, T., Kaltbeitzel, D., Hopmann, C., et al. (2014). Bioabsorbable Interbody Magnesium-Polymer Cage: Degradation Kinetics, Biomechanical Stiffness, and Histological Findings From an Ovine Cervical Spine Fusion Model. Spine *39*, E1220–E1227. 10.1097/BRS.0000000000000507.

89. Farraro, K.F., Sasaki, N., Woo, S.L.-Y., Kim, K.E., Tei, M.M., Speziali, A., and McMahon, P.J. (2016). Magnesium ring device to restore function of a transected anterior cruciate ligament in the goat stifle joint: Mg RING FOR ACL REPAIR. J. Orthop. Res. *34*, 2001–2008. 10.1002/jor.23210.

90. nanoMAG https://www.nanomag.us/.

91. Syntellix GmbH https://www.syntellix.de/home.html.

92. Leonhardt, H., Franke, A., McLeod, N.M.H., Lauer, G., and Nowak, A. (2017). Fixation of fractures of the condylar head of the mandible with a new magnesium-alloy biodegradable cannulated headless bone screw. British Journal of Oral and Maxillofacial Surgery *55*, 623–625. 10.1016/j.bjoms.2017.04.007.

93. Leonhardt, H., Ziegler, A., Lauer, G., and Franke, A. (2021). Osteosynthesis of the Mandibular Condyle With Magnesium-Based Biodegradable Headless Compression Screws Show Good Clinical Results During a 1-Year Follow-Up Period. Journal of Oral and Maxillofacial Surgery *79*, 637–643. 10.1016/j.joms.2020.02.025.

94. Acar, B., Kose, O., Unal, M., Turan, A., Kati, Y.A., and Guler, F. (2020). Comparison of magnesium versus titanium screw fixation for biplane chevron medial malleolar osteotomy in the treatment of osteochondral lesions of the talus. Eur J Orthop Surg Traumatol *30*, 163–173. 10.1007/s00590-019-02524-1.

95. May, H., Alper Kati, Y., Gumussuyu, G., Yunus Emre, T., Unal, M., and Kose, O. (2020). Bioabsorbable magnesium screw versus conventional titanium screw fixation for medial malleolar fractures. J Orthop Traumatol *21*, 9. 10.1186/s10195-020-00547-7.

96. Biber, R., Pauser, J., Geßlein, M., and Bail, H.J. (2016). Magnesium-Based Absorbable Metal Screws for Intra-Articular Fracture Fixation. Case Reports in Orthopedics *2016*, 1–4. 10.1155/2016/9673174.

97. Aktan, C., Ertan, M.B., Turan, A., and Kose, O. (2018). Fixation of Small Osteochondral Fragments in a Comminuted Distal Humerus Fracture with Magnesium Bioabsorbable Screws: A Case Report. Cureus. 10.7759/cureus.3752.

98. Meier, R., and Panzica, M. (2017). Erste Ergebnisse mit einer resorbierbaren MgYREZr-Kompressionsschraube bei der instabilen Kahnbeinfraktur zeigen eine massive Zystenbildung. Handchir Mikrochir plast Chir *49*, 37–41. 10.1055/s-0042-121416.

99. Grieve, P., O'Carroll, S., and Albastaki, O. (2017). Six cas de série de patients de Magnezix ® . Une vis métallique absorbable pour la fixation de la fracture du carpe et des fusions entre les carpes. Hand Surgery and Rehabilitation *36*, 488–489. 10.1016/j.hansur.2017.10.184.

100. Gigante, A., Setaro, N., Rotini, M., Finzi, S.S., and Marinelli, M. (2018). Intercondylar eminence fracture treated by resorbable magnesium screws osteosynthesis: A case series. Injury *49*, S48–S53. 10.1016/j.injury.2018.09.055.

101. Luthringer, B.J.C., Feyerabend, F., and Willumeit-Römer, R. (2014). Magnesium-based implants: a mini-review. Magnesium Research *27*, 142–154. 10.1684/mrh.2015.0375.

102. Zartner, P., Cesnjevar, R., Singer, H., and Weyand, M. (2005). First successful implantation of a biodegradable metal stent into the left pulmonary artery of a preterm baby. Cathet. Cardiovasc. Intervent. *66*, 590–594. 10.1002/ccd.20520.

103. Haude, M., Ince, H., Toelg, R., Lemos, P.A., von Birgelen, C., Christiansen, E.H., Wijns, W., Neumann, F.-J., Eeckhout, E., Garcia-Garcia, H.M., et al. (2020). Safety and performance of the second-generation drug-eluting absorbable metal scaffold (DREAMS 2G) in patients with de novo coronary lesions: three-year clinical results and angiographic findings of the BIOSOLVE-II first-in-man trial. EuroIntervention *15*, e1375–e1382. 10.4244/EIJ-D-18-01000.

104. Vennemeyer, J., Hopkins, T., Hershcovitch, M., Little, K., Hagen, M., Minteer, D., Hom, D., Marra, K., and Pixley, S. (2015). Initial observations on using magnesium metal in peripheral nerve repair. J Biomater Appl *29*, 1145–1154. 10.1177/0885328214553135.

105. Hänzi, A.C., Metlar, A., Schinhammer, M., Aguib, H., Lüth, T.C., Löffler, J.F., and Uggowitzer, P.J. (2011). Biodegradable wound-closing devices for gastrointestinal interventions: Degradation performance of the magnesium tip. Materials Science and Engineering: C *31*, 1098–1103. 10.1016/j.msec.2011.03.012.

106. Velox CD <http://transluminal.net/aboutvelox.html>.

107. Chng, C.B., Lau, D.P., Choo, J.Q., and Chui, C.K. (2012). A bioabsorbable microclip for laryngeal microsurgery: Design and evaluation. Acta Biomaterialia *8*, 2835–2844. 10.1016/j.actbio.2012.03.051.

108. Luffy, S.A., Chou, D.-T., Waterman, J., Wearden, P.D., Kumta, P.N., and Gilbert, T.W. (2014). Evaluation of magnesium-yttrium alloy as an extraluminal tracheal stent: Evaluation of magnesium-yttrium alloy. J. Biomed. Mater. Res. *102*, 611–620. 10.1002/jbm.a.34731.

109. Albaraghtheh, T., Willumeit-Römer, R., and Zeller-Plumhoff, B. (2022). In silico studies of magnesium-based implants: A review of the current stage and challenges. Journal of Magnesium and Alloys *10*, 2968–2996. 10.1016/j.jma.2022.09.029.

110. Department of Materials Engineering, KU Leuven, Kasteelpark Arenberg 44-bus 2450, 3001 Leuven, Belgium, Marco, I., Myrissa, A., Martinelli, E., Feyerabend, F., Willumeit-Römer, R., Weinberg, A., and Van der Biest, O. (2017). In vivo and in vitro

degradation comparison of pure Mg, Mg-10Gd and Mg-2Ag: a short term study. eCM *33*, 90–104. 10.22203/eCM.v033a07.

111. Chu, W., Li, T., Jia, G., Chang, Y., Liu, Z., Pei, J., Yu, D., and Zhai, Z. (2020). Exposure to high levels of magnesium disrupts bone mineralization in vitro and in vivo. Ann Transl Med *8*, 1419–1419. 10.21037/atm-20-1921.

112. Gonzalez, J., Hou, R.Q., Nidadavolu, E.P.S., Willumeit-Römer, R., and Feyerabend, F. (2018). Magnesium degradation under physiological conditions – Best practice. Bioactive Materials *3*, 174–185. 10.1016/j.bioactmat.2018.01.003.

113. Rettig, R., and Virtanen, S. (2009). Composition of corrosion layers on a magnesium rare-earth alloy in simulated body fluids. J. Biomed. Mater. Res. *88A*, 359–369. 10.1002/jbm.a.31887.

114. Erne, P., Schier, M., and Resink, T.J. (2006). The Road to Bioabsorbable Stents: Reaching Clinical Reality? Cardiovasc Intervent Radiol *29*, 11–16. 10.1007/s00270-004-0341-9.

115. Waksman, R., Erbel, R., Di Mario, C., Bartunek, J., De Bruyne, B., Eberli, F.R., Erne, P., Haude, M., Horrigan, M., Ilsley, C., et al. (2009). Early- and Long-Term Intravascular Ultrasound and Angiographic Findings After Bioabsorbable Magnesium Stent Implantation in Human Coronary Arteries. JACC: Cardiovascular Interventions *2*, 312–320. 10.1016/j.jcin.2008.09.015.

116. Peng, H., Wang, W., Jiang, H., Zan, R., Sun, Y., Yu, S., Ni, J., Wang, W., Wang, T., Wang, J., et al. (2021). Effect of Galvanic Corrosion on the Degradability of Biomedical Magnesium. Front. Mater. *8*, 767179. 10.3389/fmats.2021.767179.

117. Hou, P., Han, P., Zhao, C., Wu, H., Ni, J., Zhang, S., Liu, J., Zhang, Y., Xu, H., Cheng, P., et al. (2017). Accelerating Corrosion of Pure Magnesium Co-implanted with Titanium in Vivo. Sci Rep *7*, 41924. 10.1038/srep41924.

118. Lambotte A (1932). L'utilisation du magnésium comme matériel perdu dans l'ostéo synthèse. Bull Mém Soc Nat Cir *26*, 1325–1334.

119. Witte, F., Kaese, V., Haferkamp, H., Switzer, E., Meyer-Lindenberg, A., Wirth, C.J., and Windhagen, H. (2005). In vivo corrosion of four magnesium alloys and the associated bone response. Biomaterials *26*, 3557–3563. 10.1016/j.biomaterials.2004.09.049.

120. Liu, M., Uggowitzer, P.J., Nagasekhar, A.V., Schmutz, P., Easton, M., Song, G.-L., and Atrens, A. (2009). Calculated phase diagrams and the corrosion of die-cast Mg–Al alloys. Corrosion Science *51*, 602–619. 10.1016/j.corsci.2008.12.015.

121. Hofstetter, J., Martinelli, E., Pogatscher, S., Schmutz, P., Povoden-Karadeniz, E., Weinberg, A.M., Uggowitzer, P.J., and Löffler, J.F. (2015). Influence of trace impurities on the in vitro and in vivo degradation of biodegradable Mg–5Zn–0.3Ca alloys. Acta Biomaterialia *23*, 347–353. 10.1016/j.actbio.2015.05.004.

122. Zheng, Y.F., Gu, X.N., and Witte, F. (2014). Biodegradable metals. Materials Science and Engineering: R: Reports *77*, 1–34. 10.1016/j.mser.2014.01.001.

123. Ding, Y., Wen, C., Hodgson, P., and Li, Y. (2014). Effects of alloying elements on the corrosion behavior and biocompatibility of biodegradable magnesium alloys: a review. J. Mater. Chem. B *2*, 1912–1933. 10.1039/C3TB21746A.

124. Ovri, H., Markmann, J., Barthel, J., Kruth, M., Dieringa, H., and Lilleodden, E.T. (2023). Mechanistic origin of the enhanced strength and ductility in Mg-rare earth alloys. Acta Materialia *244*, 118550. 10.1016/j.actamat.2022.118550.

125. Zhang, X., Wu, Y., Xue, Y., Wang, Z., and Yang, L. (2012). Biocorrosion behavior and cytotoxicity of a Mg–Gd–Zn–Zr alloy with long period stacking ordered structure. Materials Letters *86*, 42–45. 10.1016/j.matlet.2012.07.030.

126. Peng, Q., Guo, J., Fu, H., Cai, X., Wang, Y., Liu, B., and Xu, Z. (2014). Degradation behavior of Mg-based biomaterials containing different long-period stacking ordered phases. Sci Rep *4*, 3620. 10.1038/srep03620.

127. Alaneme, K.K., and Okotete, E.A. (2017). Enhancing plastic deformability of Mg and its alloys—A review of traditional and nascent developments. Journal of Magnesium and Alloys *5*, 460–475. 10.1016/j.jma.2017.11.001.

128. Sandlöbes, S., Zaefferer, S., Schestakow, I., Yi, S., and Gonzalez-Martinez, R. (2011). On the role of non-basal deformation mechanisms for the ductility of Mg and Mg–Y alloys. Acta Materialia *59*, 429–439. 10.1016/j.actamat.2010.08.031.

129. Wu, J., Si, S., Takagi, K., Li, T., Mine, Y., Takashima, K., and Chiu, Y.L. (2020). Study of basal < a > and pyramidal < c + a > slips in Mg-Y alloys using micro-pillar compression. Philosophical Magazine *100*, 1454–1475. 10.1080/14786435.2020.1725250.

130. Buey, D., Hector, L.G., and Ghazisaeidi, M. (2018). Core structure and solute strengthening of second-order pyramidal 〈 c + a 〉 dislocations in Mg-Y alloys. Acta Materialia *147*, 1–9. 10.1016/j.actamat.2017.12.066.

131. Tehranchi, A., Yin, B., and Curtin, W.A. (2018). Solute strengthening of basal slip in Mg alloys. Acta Materialia *151*, 56–66. 10.1016/j.actamat.2018.02.056.

132. Tang, L., Liu, W., Ding, Z., Zhang, D., Zhao, Y., Lavernia, E.J., and Zhu, Y. (2016). Alloying Mg with Gd and Y: Increasing both plasticity and strength. Computational Materials Science *115*, 85–91. 10.1016/j.commatsci.2016.01.003.

133. Li, H., Wang, P., Lin, G., and Huang, J. (2021). The role of rare earth elements in biodegradable metals: A review. Acta Biomaterialia *129*, 33–42. 10.1016/j.actbio.2021.05.014.

134. Rahmati, M., Stötzel, S., Khassawna, T.E., Iskhahova, K., Florian Wieland, D., Zeller Plumhoff, B., and Haugen, H.J. (2021). Early osteoimmunomodulatory effects of magnesium–calcium–zinc alloys. J Tissue Eng *12*, 204173142110471. 10.1177/20417314211047100.

135. Rahman, M., Li, Y., and Wen, C. (2020). HA coating on Mg alloys for biomedical applications: A review. Journal of Magnesium and Alloys *8*, 929–943. 10.1016/j.jma.2020.05.003.

136. Serkan Baslayici, Mahmut Ercan Acma, and Mehmet Bugdayci (2021). Corrosion behaviour of hydroxyapatite coatings on AZ31 and AZ91 magnesium alloys by plasma spray. Journal of Ceramic Processing Research *22*, 98–105. 10.36410/JCPR.2021.22.1.98.

137. Al-Amin, M., Abdul-Rani, A.M., Danish, M., Rubaiee, S., Mahfouz, A. bin, Thompson, H.M., Ali, S., Unune, D.R., and Sulaiman, M.H. (2021). Investigation of Coatings,

Corrosion and Wear Characteristics of Machined Biomaterials through Hydroxyapatite Mixed-EDM Process: A Review. Materials *14*, 3597. 10.3390/ma14133597.

138. Chen, J., Yang, Y., Etim, I.P., Tan, L., Yang, K., Misra, R.D.K., Wang, J., and Su, X. (2021). Recent Advances on Development of Hydroxyapatite Coating on Biodegradable Magnesium Alloys: A Review. Materials *14*, 5550. 10.3390/ma14195550.

139. Nuñez-Nava, M., Vazquez, E., Ortega-Lara, W., Rodriguez, C.A., and García-López, E. (2021). An assessment of magnesium AZ31 coronary stents manufacture. Mater. Res. Express *8*, 075403. 10.1088/2053-1591/ac16f2.

140. Kim, J. (2020). Systematic approach to characterize the dynamics of protein adsorption on the surface of biomaterials using proteomics. Colloids and Surfaces B: Biointerfaces *188*, 110756. 10.1016/j.colsurfb.2019.110756.

141. Romero-Gavilan, F., Sánchez-Pérez, A.M., Araújo-Gomes, N., Azkargorta, M., Iloro, I., Elortza, F., Gurruchaga, M., Goñi, I., and Suay, J. (2017). Proteomic analysis of silica hybrid sol-gel coatings: a potential tool for predicting the biocompatibility of implants *in vivo*. Biofouling *33*, 676–689. 10.1080/08927014.2017.1356289.

142. Hiraguchi, Y., Nagahashi, K., Shibayama, T., Hayashi, T., Yano, T., Kushiro, K., and Takai, M. (2014). Effect of the distribution of adsorbed proteins on cellular adhesion behaviors using surfaces of nanoscale phase-reversed amphiphilic block copolymers. Acta Biomaterialia *10*, 2988–2995. 10.1016/j.actbio.2014.03.019.

143. Zhang, Z.-Q., Wang, H.-Y., Wang, L., Chen, X.-B., Guan, S.-K., Lin, C.-G., and Zeng, R.-C. (2022). Protein conformation and electric attraction adsorption mechanisms on anodized magnesium alloy by molecular dynamics simulations. Journal of Magnesium and Alloys *10*, 3143–3155. 10.1016/j.jma.2021.04.005.

144. Kaya, A.A. (2020). A Review on Developments in Magnesium Alloys. Front. Mater. *7*, 198. 10.3389/fmats.2020.00198.

145. Castellani, C., Lindtner, R.A., Hausbrandt, P., Tschegg, E., Stanzl-Tschegg, S.E., Zanoni, G., Beck, S., and Weinberg, A.-M. (2011). Bone–implant interface strength and osseointegration: Biodegradable magnesium alloy versus standard titanium control. Acta Biomaterialia *7*, 432–440. 10.1016/j.actbio.2010.08.020.

146. Yamamoto, A., and Hiromoto, S. (2009). Effect of inorganic salts, amino acids and proteins on the degradation of pure magnesium in vitro. Materials Science and Engineering: C *29*, 1559–1568. 10.1016/j.msec.2008.12.015.

147. Chen, J., Xu, Y., Kolawole, S.K., Wang, J., Su, X., Tan, L., and Yang, K. (2022). Systems, Properties, Surface Modification and Applications of Biodegradable Magnesium-Based Alloys: A Review. Materials *15*, 5031. 10.3390/ma15145031.

148. Jessen, L.K., Zamponi, C., and Quandt, E. (2019). Mechanical Properties of Magnetron Sputtered Free Standing Mg-Ag Alloy Films. Front. Mater. *6*, 236. 10.3389/fmats.2019.00236.

149. Jiao, J., Zhang, S., Qu, X., and Yue, B. (2021). Recent Advances in Research on Antibacterial Metals and Alloys as Implant Materials. Front. Cell. Infect. Microbiol. *11*, 693939. 10.3389/fcimb.2021.693939.

150. Geng, Z., Wang, R., Zhuo, X., Li, Z., Huang, Y., Ma, L., Cui, Z., Zhu, S., Liang, Y., Liu, Y., et al. (2017). Incorporation of silver and strontium in hydroxyapatite coating on titanium

surface for enhanced antibacterial and biological properties. Materials Science and Engineering: C *71*, 852–861. 10.1016/j.msec.2016.10.079.

151. Surmeneva, M.A., Sharonova, A.A., Chernousova, S., Prymak, O., Loza, K., Tkachev, M.S., Shulepov, I.A., Epple, M., and Surmenev, R.A. (2017). Incorporation of silver nanoparticles into magnetron-sputtered calcium phosphate layers on titanium as an antibacterial coating. Colloids and Surfaces B: Biointerfaces *156*, 104–113. 10.1016/j.colsurfb.2017.05.016.

152. Shivaram, A., Bose, S., and Bandyopadhyay, A. (2017). Understanding long-term silver release from surface modified porous titanium implants. Acta Biomaterialia *58*, 550–560. 10.1016/j.actbio.2017.05.048.

153. Tie, D., Feyerabend, F., Müller, W.-D., Schade, R., Liefeith, K., Kainer, K., and Willumeit, R. (2013). Antibacterial biodegradable Mg-Ag alloys. eCM *25*, 284–298. 10.22203/eCM.v025a20.

154. Costantino, M.D., Schuster, A., Helmholz, H., Meyer-Rachner, A., Willumeit-Römer, R., and Luthringer-Feyerabend, B.J.C. (2020). Inflammatory response to magnesium-based biodegradable implant materials. Acta Biomaterialia *101*, 598–608. 10.1016/j.actbio.2019.10.014.

155. Mei, D., Lamaka, S.V., Lu, X., and Zheludkevich, M.L. (2020). Selecting medium for corrosion testing of bioabsorbable magnesium and other metals – A critical review. Corrosion Science *171*, 108722. 10.1016/j.corsci.2020.108722.

156. Hort, N., Huang, Y., Fechner, D., Störmer, M., Blawert, C., Witte, F., Vogt, C., Drücker, H., Willumeit, R., and Kainer, K.U. (2010). Magnesium alloys as implant materials – Principles of property design for Mg–RE alloys☆. Acta Biomaterialia *6*, 1714–1725. 10.1016/j.actbio.2009.09.010.

157. Krüger, D., Zeller-Plumhoff, B., Wiese, B., Yi, S., Zuber, M., Wieland, D.C.F., Moosmann, J., and Willumeit-Römer, R. (2021). Assessing the microstructure and in vitro degradation behavior of Mg-xGd screw implants using µCT. Journal of Magnesium and Alloys *9*, 2207–2222. 10.1016/j.jma.2021.07.029.

158. Sabbaghian, M., Mahmudi, R., and Shin, K.S. (2021). Microstructural Evolution, Mechanical Properties, and Biodegradability of a Gd-Containing Mg-Zn Alloy. Metall Mater Trans A *52*, 1269–1281. 10.1007/s11661-021-06160-5.

159. Galli S, Hammel J, Agha N, Szakács G, Marco I, and Lukac F (2016). Degradation behaviour and bone response of 3 magnesium alloys in comparison with titanium : An in vivo investigation. Materials *4*, 2197–2218.

160. Myrissa, A., Braeuer, S., Martinelli, E., Willumeit-Römer, R., Goessler, W., and Weinberg, A.M. (2017). Gadolinium accumulation in organs of Sprague–Dawley® rats after implantation of a biodegradable magnesium-gadolinium alloy. Acta Biomaterialia *48*, 521–529. 10.1016/j.actbio.2016.11.024.

161. Eddy Jai Poinern, G., Brundavanam, S., and Fawcett, D. (2013). Biomedical Magnesium Alloys: A Review of Material Properties, Surface Modifications and Potential as a Biodegradable Orthopaedic Implant. AJBE *2*, 218–240. 10.5923/j.ajbe.20120206.02.

162. Wang, Z., Wang, J.-G., Chen, Z.-Y., Zha, M., Wang, C., Liu, S., and Yan, R.-F. (2018). Effect of Ce Addition on Modifying the Microstructure and Achieving a High

Elongation with a Relatively High Strength of As-Extruded AZ80 Magnesium Alloy. Materials *12*, 76. 10.3390/ma12010076.

163. Feng, L., Dong, X., Cai, Q., Wang, B., and Ji, S. (2023). Effect of Nd on the Microstructure and Mechanical Properties of Mg-La-Ce Alloys at Ambient and Elevated Temperatures. J. of Materi Eng and Perform *32*, 2598–2606. 10.1007/s11665-022-06853-x.

164. Agarwal, S., Curtin, J., Duffy, B., and Jaiswal, S. (2016). Biodegradable magnesium alloys for orthopaedic applications: A review on corrosion, biocompatibility and surface modifications. Materials Science and Engineering: C *68*, 948–963. 10.1016/j.msec.2016.06.020.

165. Rokhlin, L.L. (2003). Magnesium Alloys Containing Rare Earth Metals: Structure and Properties 0 ed. (CRC Press) 10.1201/9781482265163.

166. Liu, D., Yang, D., Li, X., and Hu, S. (2019). Mechanical properties, corrosion resistance and biocompatibilities of degradable Mg-RE alloys: A review. Journal of Materials Research and Technology *8*, 1538–1549. 10.1016/j.jmrt.2018.08.003.

167. Calado, L.M., Carmezim, M.J., and Montemor, M.F. (2022). Rare Earth Based Magnesium Alloys—A Review on WE Series. Front. Mater. *8*, 804906. 10.3389/fmats.2021.804906.

168. Hanzi, A., Gunde, P., Schinhammer, M., and Uggowitzer, P. (2009). On the biodegradation performance of an Mg–Y–RE alloy with various surface conditions in simulated body fluid. Acta Biomaterialia *5*, 162–171. 10.1016/j.actbio.2008.07.034.

169. Chu, P.-W., and Marquis, E.A. (2015). Linking the microstructure of a heat-treated WE43 Mg alloy with its corrosion behavior. Corrosion Science *101*, 94–104. 10.1016/j.corsci.2015.09.005.

170. Jähn, K., Saito, H., Taipaleenmäki, H., Gasser, A., Hort, N., Feyerabend, F., Schlüter, H., Rueger, J.M., Lehmann, W., Willumeit-Römer, R., et al. (2016). Intramedullary Mg2Ag nails augment callus formation during fracture healing in mice. Acta Biomaterialia *36*, 350–360. 10.1016/j.actbio.2016.03.041.

171. Broome, D.R., Girguis, M.S., Baron, P.W., Cottrell, A.C., Kjellin, I., and Kirk, G.A. (2007). Gadodiamide-Associated Nephrogenic Systemic Fibrosis: Why Radiologists Should Be Concerned. American Journal of Roentgenology *188*, 586–592. 10.2214/AJR.06.1094.

172. Ramalho, M., Ramalho, J., Burke, L.M., and Semelka, R.C. (2017). Gadolinium Retention and Toxicity—An Update. Advances in Chronic Kidney Disease *24*, 138–146. 10.1053/j.ackd.2017.03.004.

173. Peruzzi, N., Galli, S., Helmholz, H., Kardjilov, N., Krüger, D., Markötter, H., Moosmann, J., Orlov, D., Prgomet, Z., Willumeit-Römer, R., et al. (2021). Multimodal ex vivo methods reveal that Gd-rich corrosion byproducts remain at the implant site of biodegradable Mg-Gd screws. Acta Biomaterialia *136*, 582–591. 10.1016/j.actbio.2021.09.047.

174. Grünewald, T.A., Rennhofer, H., Hesse, B., Burghammer, M., Stanzl-Tschegg, S.E., Cotte, M., Löffler, J.F., Weinberg, A.M., and Lichtenegger, H.C. (2016). Magnesium from bioresorbable implants: Distribution and impact on the nano- and mineral structure of bone. Biomaterials *76*, 250–260. 10.1016/j.biomaterials.2015.10.054.

175. Meischel, M., Hörmann, D., Draxler, J., Tschegg, E.K., Eichler, J., Prohaska, T., and Stanzl-Tschegg, S.E. (2017). Bone-implant degradation and mechanical response of bone surrounding Mg-alloy implants. Journal of the Mechanical Behavior of Biomedical Materials *71*, 307–313. 10.1016/j.jmbbm.2017.03.025.

176. Grünewald, T.A., Ogier, A., Akbarzadeh, J., Meischel, M., Peterlik, H., Stanzl-Tschegg, S., Löffler, J.F., Weinberg, A.M., and Lichtenegger, H.C. (2016). Reaction of bone nanostructure to a biodegrading Magnesium WZ21 implant – A scanning small-angle X-ray scattering time study. Acta Biomaterialia *31*, 448–457. 10.1016/j.actbio.2015.11.049.

177. Seitz, J.-M., Eifler, R., Bach, Fr.-W., and Maier, H.J. (2014). Magnesium degradation products: Effects on tissue and human metabolism: Effects on Tissue and Human Metabolism. J. Biomed. Mater. Res. *102*, 3744–3753. 10.1002/jbm.a.35023.

178. Wang, J., Witte, F., Xi, T., Zheng, Y., Yang, K., Yang, Y., Zhao, D., Meng, J., Li, Y., Li, W., et al. (2015). Recommendation for modifying current cytotoxicity testing standards for biodegradable magnesium-based materials. Acta Biomaterialia *21*, 237–249. 10.1016/j.actbio.2015.04.011.

179. Burmester, A., Luthringer, B., Willumeit, R., and Feyerabend, F. (2014). Comparison of the reaction of bone-derived cells to enhanced $MgCl_2$ -salt concentrations. Biomatter *4*, e967616. 10.4161/21592527.2014.967616.

180. He, L.Y., Zhang, X.M., Liu, B., Tian, Y., and Ma, W.H. (2016). Effect of magnesium ion on human osteoblast activity. Braz J Med Biol Res *49*, e5257. 10.1590/1414-431x20165257.

181. Zhang, L., Yang, C., Li, J., Zhu, Y., and Zhang, X. (2014). High extracellular magnesium inhibits mineralized matrix deposition and modulates intracellular calcium signaling in human bone marrow-derived mesenchymal stem cells. Biochemical and Biophysical Research Communications *450*, 1390–1395. 10.1016/j.bbrc.2014.07.004.

182. Zhang, J., Tang, L., Qi, H., Zhao, Q., Liu, Y., and Zhang, Y. (2019). Dual Function of Magnesium in Bone Biomineralization. Adv. Healthcare Mater. *8*, 1901030. 10.1002/adhm.201901030.

183. Mammoli, F., Castiglioni, S., Parenti, S., Cappadone, C., Farruggia, G., Iotti, S., Davalli, P., Maier, J., Grande, A., and Frassineti, C. (2019). Magnesium Is a Key Regulator of the Balance between Osteoclast and Osteoblast Differentiation in the Presence of Vitamin D3. IJMS *20*, 385. 10.3390/ijms20020385.

184. Leidi, M., Dellera, F., Mariotti, M., and Maier, J.A.M. (2011). High magnesium inhibits human osteoblast differentiation in vitro. Magnesium Research *24*, 1–6. 10.1684/mrh.2011.0271.

185. Wu, L., Luthringer, B.J.C., Feyerabend, F., Schilling, A.F., and Willumeit, R. (2014). Effects of extracellular magnesium on the differentiation and function of human osteoclasts. Acta Biomaterialia *10*, 2843–2854. 10.1016/j.actbio.2014.02.010.

186. Wu, L., Feyerabend, F., Schilling, A.F., Willumeit-Römer, R., and Luthringer, B.J.C. (2015). Effects of extracellular magnesium extract on the proliferation and differentiation of human osteoblasts and osteoclasts in coculture. Acta Biomaterialia *27*, 294–304. 10.1016/j.actbio.2015.08.042.

187. Bernhardt, A., Helmholz, H., Kilian, D., Willumeit-Römer, R., and Gelinsky, M. (2022). Impact of degradable magnesium implants on osteocytes in single and triple cultures. Biomaterials Advances *134*, 112692. 10.1016/j.msec.2022.112692.

188. Clarke R (2005). Incoherent sources: Synchrotrons. Encyclopedia of Modern Optics, 217–224.

189. Willmott Philip (2011). An Introduction to Synchrotron Radiation, Techniques and Applications (John Wiley & Sons Ltd.).

190. Winick, H. (1995). Synchrotron Radiation Sources — A Primer (WORLD SCIENTIFIC) 10.1142/2444.

191. Kinney, J.H., and Nichols, M.C. (1992). X-Ray Tomographic Microscopy (XTM) Using Synchrotron Radiation. Annu. Rev. Mater. Sci. *22*, 121–152. 10.1146/annurev.ms.22.080192.001005.

192. Kak, A.C., and Slaney, M. (2001). Principles of Computerized Tomographic Imaging (Society for Industrial and Applied Mathematics) 10.1137/1.9780898719277.

193. Zeller-Plumhoff, B., Tolnai, D., Wolff, M., Greving, I., Hort, N., and Willumeit-Römer, R. (2021). Utilizing Synchrotron Radiation for the Characterization of Biodegradable Magnesium Alloys—From Alloy Development to the Application as Implant Material. Adv Eng Mater *23*, 2100197. 10.1002/adem.202100197.

194. Radon, J. (1986). On the determination of functions from their integral values along certain manifolds. IEEE Trans. Med. Imaging *5*, 170–176. 10.1109/TMI.1986.4307775.

195. Wilde, F., Ogurreck, M., Greving, I., Hammel, J.U., Beckmann, F., Hipp, A., Lottermoser, L., Khokhriakov, I., Lytaev, P., Dose, T., et al. (2016). Micro-CT at the imaging beamline P05 at PETRA III. In, p. 030035. 10.1063/1.4952858.

196. Longo, E., Sancey, L., Flenner, S., Kubec, A., Bonnin, A., David, C., Müller, M., and Greving, I. (2020). X-ray Zernike phase contrast tomography: 3D ROI visualization of mm-sized mice organ tissues down to sub-cellular components. Biomed. Opt. Express *11*, 5506. 10.1364/BOE.396695.

197. Hémonnot, C.Y.J., and Köster, S. (2017). Imaging of Biological Materials and Cells by X-ray Scattering and Diffraction. ACS Nano *11*, 8542–8559. 10.1021/acsnano.7b03447.

198. Andrews, J.C., Almeida, E., van der Meulen, M.C.H., Alwood, J.S., Lee, C., Liu, Y., Chen, J., Meirer, F., Feser, M., Gelb, J., et al. (2010). Nanoscale X-Ray Microscopic Imaging of Mammalian Mineralized Tissue. Microsc Microanal *16*, 327–336. 10.1017/S1431927610000231.

199. Gureyev, T.E., Mayo, S., Wilkins, S.W., Paganin, D., and Stevenson, A.W. (2001). Quantitative In-Line Phase-Contrast Imaging with Multienergy X Rays. Phys. Rev. Lett. *86*, 5827–5830. 10.1103/PhysRevLett.86.5827.

200. Weitkamp, T., Diaz, A., David, C., Pfeiffer, F., Stampanoni, M., Cloetens, P., and Ziegler, E. (2005). X-ray phase imaging with a grating interferometer. Opt. Express *13*, 6296. 10.1364/OPEX.13.006296.

201. Cloetens, P., Ludwig, W., Baruchel, J., Van Dyck, D., Van Landuyt, J., Guigay, J.P., and Schlenker, M. (1999). Holotomography: Quantitative phase tomography with

micrometer resolution using hard synchrotron radiation x rays. Appl. Phys. Lett. *75*, 2912–2914. 10.1063/1.125225.

202. Lohse, L.M., Robisch, A.-L., Töpperwien, M., Maretzke, S., Krenkel, M., Hagemann, J., and Salditt, T. (2020). A phase-retrieval toolbox for X-ray holography and tomography. J Synchrotron Rad *27*, 852–859. 10.1107/S1600577520002398.

203. Hagemann, J., Töpperwien, M., and Salditt, T. (2018). Phase retrieval for near-field X-ray imaging beyond linearisation or compact support. Appl. Phys. Lett. *113*, 041109. 10.1063/1.5029927.

204. Flenner, S., Storm, M., Kubec, A., Longo, E., Döring, F., Pelt, D.M., David, C., Müller, M., and Greving, I. (2020). Pushing the temporal resolution in absorption and Zernike phase contrast nanotomography: enabling fast *in situ* experiments. J Synchrotron Rad *27*, 1339–1346. 10.1107/S1600577520007407.

205. Andrews, J.C., Brennan, S., Patty, C., Luening, K., Pianetta, P., Almeida, E., van der Meulen, M.C.H., Feser, M., Gelb, J., Rudati, J., et al. (2008). A High Resolution, Hard X-ray Bio-imaging Facility at SSRL. Synchrotron Radiation News *21*, 17–26. 10.1080/08940880802123043.

206. Töpperwien, M., Markus, A., Alves, F., and Salditt, T. (2019). Contrast enhancement for visualizing neuronal cytoarchitecture by propagation-based x-ray phase-contrast tomography. NeuroImage *199*, 70–80. 10.1016/j.neuroimage.2019.05.043.

207. Liu, Y., Nelson, J., Holzner, C., Andrews, J.C., and Pianetta, P. (2013). Recent advances in synchrotron-based hard x-ray phase contrast imaging. J. Phys. D: Appl. Phys. *46*, 494001. 10.1088/0022-3727/46/49/494001.

208. Holzner, C., Feser, M., Vogt, S., Hornberger, B., Baines, S.B., and Jacobsen, C. (2010). Zernike phase contrast in scanning microscopy with X-rays. Nature Phys *6*, 883–887. 10.1038/nphys1765.

209. Flenner, S., Hagemann, J., Storm, M., Kubec, A., Qi, P., David, C., Longo, E., Niese, S., Gawlitza, P., Zeller-Plumhoff, B., et al. (2022). Hard x-ray nanotomography at the P05 imaging beamline at PETRA III. In Developments in X-Ray Tomography XIV, B. Müller and G. Wang, eds. (SPIE), p. 19. 10.1117/12.2632706.

210. Pushie, M.J., Pickering, I.J., Korbas, M., Hackett, M.J., and George, G.N. (2014). Elemental and Chemically Specific X-ray Fluorescence Imaging of Biological Systems. Chem. Rev. *114*, 8499–8541. 10.1021/cr4007297.

211. Witte, F., Fischer, J., Nellesen, J., Crostack, H.-A., Kaese, V., Pisch, A., Beckmann, F., and Windhagen, H. (2006). In vitro and in vivo corrosion measurements of magnesium alloys. Biomaterials *27*, 1013–1018. 10.1016/j.biomaterials.2005.07.037.

212. Witte, F., Fischer, J., Nellesen, J., Vogt, C., Vogt, J., Donath, T., and Beckmann, F. (2010). In vivo corrosion and corrosion protection of magnesium alloy LAE442☆. Acta Biomaterialia *6*, 1792–1799. 10.1016/j.actbio.2009.10.012.

213. Zeller-Plumhoff, B., Laipple, D., Slominska, H., Iskhakova, K., Longo, E., Hermann, A., Flenner, S., Greving, I., Storm, M., and Willumeit-Römer, R. (2021). Evaluating the morphology of the degradation layer of pure magnesium via 3D imaging at resolutions below 40 nm. Bioactive Materials *6*, 4368–4376. 10.1016/j.bioactmat.2021.04.009.

214. Helmholz, H., Luthringer-Feyerabend, B.J.C., and Willumeit-Römer, R. (2019). Elemental mapping of biodegradable magnesium-based implants in bone and soft tissue by means of μ X-ray fluorescence analysis. J. Anal. At. Spectrom. *34*, 356–365. 10.1039/C8JA00377G.

215. Turyanskaya, A., Rauwolf, M., Grünewald, T., Meischel, M., Stanzl-Tschegg, S., Löffler, J., Wobrauschek, P., Weinberg, A., Lichtenegger, H., and Streli, C. (2016). μXRF Elemental Mapping of Bioresorbable Magnesium-Based Implants in Bone. Materials *9*, 811. 10.3390/ma9100811.

216. Bonewald, L.F. (2011). The amazing osteocyte. J Bone Miner Res *26*, 229–238. 10.1002/jbmr.320.

217. Burger, E.H., and Klein-Nulend, J. (1999). Mechanotransduction in bone—role of the lacunocanalicular network. FASEB j. *13*. 10.1096/fasebj.13.9001.s101.

218. Dierolf, M., Menzel, A., Thibault, P., Schneider, P., Kewish, C.M., Wepf, R., Bunk, O., and Pfeiffer, F. (2010). Ptychographic X-ray computed tomography at the nanoscale. Nature *467*, 436–439. 10.1038/nature09419.

219. Ciani, A., Toumi, H., Pallu, S., Tsai, E.H.R., Diaz, A., Guizar-Sicairos, M., Holler, M., Lespessailles, E., and Kewish, C.M. (2018). Ptychographic X-ray CT characterization of the osteocyte lacuno-canalicular network in a male rat's glucocorticoid induced osteoporosis model. Bone Reports *9*, 122–131. 10.1016/j.bonr.2018.07.005.

220. Langer, M., Pacureanu, A., Suhonen, H., Grimal, Q., Cloetens, P., and Peyrin, F. (2012). X-Ray Phase Nanotomography Resolves the 3D Human Bone Ultrastructure. PLoS ONE *7*, e35691. 10.1371/journal.pone.0035691.

221. Peyrin, F., Dong, P., Pacureanu, A., and Langer, M. (2014). Micro- and Nano-CT for the Study of Bone Ultrastructure. Curr Osteoporos Rep *12*, 465–474. 10.1007/s11914-014-0233-0.

222. Hesse, B., Varga, P., Langer, M., Pacureanu, A., Schrof, S., Männicke, N., Suhonen, H., Maurer, P., Cloetens, P., Peyrin, F., et al. (2015). Canalicular Network Morphology Is the Major Determinant of the Spatial Distribution of Mass Density in Human Bone Tissue: Evidence by Means of Synchrotron Radiation Phase-Contrast nano-CT: canalicular network morphology and bone mass density spatial distribution. J Bone Miner Res *30*, 346–356. 10.1002/jbmr.2324.

223. Varga, P., Hesse, B., Langer, M., Schrof, S., Männicke, N., Suhonen, H., Pacureanu, A., Pahr, D., Peyrin, F., and Raum, K. (2015). Synchrotron X-ray phase nano-tomography-based analysis of the lacunar–canalicular network morphology and its relation to the strains experienced by osteocytes in situ as predicted by case-specific finite element analysis. Biomech Model Mechanobiol *14*, 267–282. 10.1007/s10237-014-0601-9.

224. Bortel, E., Grover, L.M., Eisenstein, N., Seim, C., Suhonen, H., Pacureanu, A., Westenberger, P., Raum, K., Langer, M., Peyrin, F., et al. (2022). Interconnectivity Explains High Canalicular Network Robustness between Neighboring Osteocyte Lacunae in Human Bone. Advanced NanoBiomed Research *2*, 2100090. 10.1002/anbr.202100090.

225. Yu, B., Pacureanu, A., Olivier, C., Cloetens, P., and Peyrin, F. (2021). Quantification of the bone lacunocanalicular network from 3D X-ray phase nanotomography images. Journal of Microscopy *282*, 30–44. 10.1111/jmi.12973.

226. Smit, T.H., Huyghe, J.M., and Cowin, S.C. (2002). Estimation of the poroelastic parameters of cortical bone. Journal of Biomechanics *35*, 829–835. 10.1016/S0021-9290(02)00021-0.

227. Nguyen, V.-H., Lemaire, T., and Naili, S. (2010). Poroelastic behaviour of cortical bone under harmonic axial loading: A finite element study at the osteonal scale. Medical Engineering & Physics *32*, 384–390. 10.1016/j.medengphy.2010.02.001.

228. Yu, W., Wu, X., Cen, H., Guo, Y., Li, C., Wang, Y., Qin, Y., and Chen, W. (2019). Study on the biomechanical responses of the loaded bone in macroscale and mesoscale by multiscale poroelastic FE analysis. BioMed Eng OnLine *18*, 122. 10.1186/s12938-019-0741-3.

229. Smit, T.H. (2022). Finite Element Models of Osteocytes and Their Load-Induced Activation. Curr Osteoporos Rep *20*, 127–140. 10.1007/s11914-022-00728-9.

230. Verbruggen, S.W., Vaughan, T.J., and McNamara, L.M. (2014). Fluid flow in the osteocyte mechanical environment: a fluid–structure interaction approach. Biomech Model Mechanobiol *13*, 85–97. 10.1007/s10237-013-0487-y.

231. Joukar, A., Niroomand-Oscuii, H., and Ghalichi, F. (2016). Numerical simulation of osteocyte cell in response to directional mechanical loadings and mechanotransduction analysis: Considering lacunar–canalicular interstitial fluid flow. Computer Methods and Programs in Biomedicine *133*, 133–141. 10.1016/j.cmpb.2016.05.019.

232. Ganesh, T., Laughrey, L.E., Niroobakhsh, M., and Lara-Castillo, N. (2020). Multiscale finite element modeling of mechanical strains and fluid flow in osteocyte lacunocanalicular system. Bone *137*, 115328. 10.1016/j.bone.2020.115328.

233. Qiu, J., and Li, F.-F. (2017). Mechanical behavior of an individual adherent MLO-Y4 osteocyte under shear flow. Biomech Model Mechanobiol *16*, 63–74. 10.1007/s10237-016-0802-5.

234. Elsayed, F.R., Hort, N., Salgado Ordorica, M.A., and Kainer, K.U. (2011). Magnesium Permanent Mold Castings Optimization. MSF *690*, 65–68. 10.4028/www.scientific.net/MSF.690.65.

235. Schindelin, J., Arganda-Carreras, I., Frise, E., Kaynig, V., Longair, M., Pietzsch, T., Preibisch, S., Rueden, C., Saalfeld, S., Schmid, B., et al. (2012). Fiji: an open-source platform for biological-image analysis. Nat Methods *9*, 676–682. 10.1038/nmeth.2019.

236. Rueden, C.T., Schindelin, J., Hiner, M.C., DeZonia, B.E., Walter, A.E., Arena, E.T., and Eliceiri, K.W. (2017). ImageJ2: ImageJ for the next generation of scientific image data. BMC Bioinformatics *18*, 529. 10.1186/s12859-017-1934-z.

237. Hall, D.J., Skerrett, E.J., and Thomas, W.D.E. (1978). Critical point drying for scanning electron microscopy: a semi-automatic method of preparing biological specimens. Journal of Microscopy *113*, 277–290. 10.1111/j.1365-2818.1978.tb00106.x.

238. Donath K (1993). Preparation of histologic sections by cutting-grinding technique for hard tissue and other materials not suitable to be sectioned by routine methods. EXAKT-Kulzer,Norderstedt, 1:16.

239. Ogurreck, M., Wilde, F., Herzen, J., Beckmann, F., Nazmov, V., Mohr, J., Haibel, A., Müller, M., and Schreyer, A. (2013). The nanotomography endstation at the PETRA III Imaging Beamline. J. Phys.: Conf. Ser. *425*, 182002. 10.1088/1742-6596/425/18/182002.

240. Haibel, A., Ogurreck, M., Beckmann, F., Dose, T., Wilde, F., Herzen, J., Müller, M., Schreyer, A., Nazmov, V., Simon, M., et al. (2010). Micro- and nano-tomography at the GKSS Imaging Beamline at PETRA III. In, S. R. Stock, ed., p. 78040B. 10.1117/12.860852.

241. Haibel, A., Beckmann, F., Dose, T., Herzen, J., Ogurreck, M., Müller, M., and Schreyer, A. (2010). Latest developments in microtomography and nanotomography at PETRA III. Powder Diffr. *25*, 161–164. 10.1154/1.3428364.

242. Moosmann, J., Ershov, A., Weinhardt, V., Baumbach, T., Prasad, M.S., LaBonne, C., Xiao, X., Kashef, J., and Hofmann, R. (2014). Time-lapse X-ray phase-contrast microtomography for in vivo imaging and analysis of morphogenesis. Nat Protoc *9*, 294–304. 10.1038/nprot.2014.033.

243. Bruns, S., Stipp, S.L.S., and Sørensen, H.O. (2017). Looking for the Signal: A guide to iterative noise and artefact removal in X-ray tomographic reconstructions of porous geomaterials. Advances in Water Resources *105*, 96–107. 10.1016/j.advwatres.2017.04.020.

244. Krüger Diana (2022). Ex vivo and In vitro Investigation of Biodegradable Magnesium-Gadolinium Implants. Christian-Albrechts University of Kiel, Faculty of Engineering.

245. Lang, A., Schulz, A., Ellinghaus, A., and Schmidt-Bleek, K. (2016). Osteotomy models – the current status on pain scoring and management in small rodents. Lab Anim *50*, 433–441. 10.1177/0023677216675007.

246. Palenstijn, W.J., Batenburg, K.J., and Sijbers, J. (2011). Performance improvements for iterative electron tomography reconstruction using graphics processing units (GPUs). Journal of Structural Biology *176*, 250–253. 10.1016/j.jsb.2011.07.017.

247. van Aarle, W., Palenstijn, W.J., De Beenhouwer, J., Altantzis, T., Bals, S., Batenburg, K.J., and Sijbers, J. (2015). The ASTRA Toolbox: A platform for advanced algorithm development in electron tomography. Ultramicroscopy *157*, 35–47. 10.1016/j.ultramic.2015.05.002.

248. Moosmann, J., Wieland, D.C.F., Zeller-Plumhoff, B., Galli, S., Krüger, D., Ershov, A., Lautner, S., Sartori, J., Dean, M., Köhring, S., et al. (2019). A load frame for in situ tomography at PETRA III. In Developments in X-Ray Tomography XII, B. Müller and G. Wang, eds. (SPIE), p. 41. 10.1117/12.2530445.

249. Núñez, J.A., Goring, A., Hesse, E., Thurner, P.J., Schneider, P., and Clarkin, C.E. (2017). Simultaneous visualisation of calcified bone microstructure and intracortical vasculature using synchrotron X-ray phase contrast-enhanced tomography. Sci Rep *7*, 13289. 10.1038/s41598-017-13632-5.

250. Fouard, C., Malandain, G., Prohaska, S., and Westerhoff, M. (2006). Blockwise processing applied to brain microvascular network study. IEEE Trans. Med. Imaging *25*, 1319–1328. 10.1109/TMI.2006.880670.

251. Gürsoy, D., De Carlo, F., Xiao, X., and Jacobsen, C. (2014). TomoPy: a framework for the analysis of synchrotron tomographic data. J Synchrotron Rad *21*, 1188–1193. 10.1107/S1600577514013939.

252. Dong, P., Haupert, S., Hesse, B., Langer, M., Gouttenoire, P.-J., Bousson, V., and Peyrin, F. (2014). 3D osteocyte lacunar morphometric properties and distributions in

human femoral cortical bone using synchrotron radiation micro-CT images. Bone *60*, 172–185. 10.1016/j.bone.2013.12.008.

253. Kerschnitzki, M., Kollmannsberger, P., Burghammer, M., Duda, G.N., Weinkamer, R., Wagermaier, W., and Fratzl, P. (2013). Architecture of the osteocyte network correlates with bone material quality: osteocyte network architecture correlates with bone material quality. J Bone Miner Res *28*, 1837–1845. 10.1002/jbmr.1927.

254. Gatti, V., Azoulay, E.M., and Fritton, S.P. (2018). Microstructural changes associated with osteoporosis negatively affect loading-induced fluid flow around osteocytes in cortical bone. Journal of Biomechanics *66*, 127–136. 10.1016/j.jbiomech.2017.11.011.

255. Knothe Tate, M.L. (2003). “Whither flows the fluid in bone?” An osteocyte’s perspective. Journal of Biomechanics *36*, 1409–1424. 10.1016/S0021-9290(03)00123-4.

256. Knothe Tate, M.L., Niederer, P., and Knothe, U. (1998). In Vivo Tracer Transport Through the Lacunocanalicular System of Rat Bone in an Environment Devoid of Mechanical Loading. Bone *22*, 107–117. 10.1016/S8756-3282(97)00234-2.

257. Manfredini, P., Cocchetti, G., Maier, G., Redaelli, A., and Montevecchi, F.M. (1999). Poroelastic finite element analysis of a bone specimen under cyclic loading. Journal of Biomechanics *32*, 135–144. 10.1016/S0021-9290(98)00162-6.

258. Anderson, E.J., Kaliyamoorthy, S., Alexander, J.I.D., and Tate, M.L.K. (2005). Nano-Microscale Models of Periosteocytic Flow Show Differences in Stresses Imparted to Cell Body and Processes. Ann Biomed Eng *33*, 52–62. 10.1007/s10439-005-8962-y.

259. Wang, X., Herting, G., Odnevall Wallinder, I., and Blomberg, E. (2015). Adsorption of bovine serum albumin on silver surfaces enhances the release of silver at pH neutral conditions. Phys. Chem. Chem. Phys. *17*, 18524–18534. 10.1039/C5CP02306H.

260. Wang, C., Zanna, S., Frateur, I., Despax, B., Raynaud, P., Mercier-Bonin, M., and Marcus, P. (2016). BSA adsorption on a plasma-deposited silver nanocomposite film controls silver release: A QCM and XPS-based modelling. Surface and Coatings Technology *307*, 1–8. 10.1016/j.surfcoat.2016.07.063.

261. Zeller-Plumhoff, B., Gile, M., Priebe, M., Slominska, H., Boll, B., Wiese, B., Würger, T., Willumeit-Römer, R., and Meißner, R.H. (2021). Exploring key ionic interactions for magnesium degradation in simulated body fluid – A data-driven approach. Corrosion Science *182*, 109272. 10.1016/j.corsci.2021.109272.

262. Myrissa, A., Agha, N.A., Lu, Y., Martinelli, E., Eichler, J., Szakács, G., Kleinhans, C., Willumeit-Römer, R., Schäfer, U., and Weinberg, A.-M. (2016). In vitro and in vivo comparison of binary Mg alloys and pure Mg. Materials Science and Engineering: C *61*, 865–874. 10.1016/j.msec.2015.12.064.

263. Turyanskaya, A., Rauwolf, M., Grünewald, T., Meischel, M., Stanzl-Tschegg, S., Löffler, J., Wobrauschek, P., Weinberg, A., Lichtenegger, H., and Streli, C. (2016). µXRF Elemental Mapping of Bioresorbable Magnesium-Based Implants in Bone. Materials *9*, 811. 10.3390/ma9100811.

264. Johnson, I., and Liu, H. (2013). A Study on Factors Affecting the Degradation of Magnesium and a Magnesium-Yttrium Alloy for Biomedical Applications. PLoS ONE *8*, e65603. 10.1371/journal.pone.0065603.

265. Helmholz, H., Luthringer-Feyerabend, B.J.C., and Willumeit-Römer, R. (2019). Elemental mapping of biodegradable magnesium-based implants in bone and soft tissue by means of μ X-ray fluorescence analysis. J. Anal. At. Spectrom. *34*, 356–365. 10.1039/C8JA00377G.

266. Willumeit, R., Möhring, A., and Feyerabend, F. (2014). Optimization of Cell Adhesion on Mg Based Implant Materials by Pre-Incubation under Cell Culture Conditions. IJMS *15*, 7639–7650. 10.3390/ijms15057639.

267. Rettig, R., and Virtanen, S. (2008). Time-dependent electrochemical characterization of the corrosion of a magnesium rare-earth alloy in simulated body fluids. J. Biomed. Mater. Res. *85A*, 167–175. 10.1002/jbm.a.31550.

268. Willumeit R, Wendel HP, Mihailova B, and Feyerabend F How does blood contact change Magnesium degradation? *28*, 29.

269. Faulón Marruecos, D., Schwartz, D.K., and Kaar, J.L. (2018). Impact of surface interactions on protein conformation. Current Opinion in Colloid & Interface Science *38*, 45–55. 10.1016/j.cocis.2018.08.002.

270. Satzer, P., Svec, F., Sekot, G., and Jungbauer, A. (2016). Protein adsorption onto nanoparticles induces conformational changes: Particle size dependency, kinetics, and mechanisms. Eng. Life Sci. *16*, 238–246. 10.1002/elsc.201500059.

271. Romero-Gavilán, F., Cerqueira, A., Anitua, E., Tejero, R., García-Arnáez, I., Martinez-Ramos, C., Ozturan, S., Izquierdo, R., Azkargorta, M., Elortza, F., et al. (2021). Protein adsorption/desorption dynamics on Ca-enriched titanium surfaces: biological implications. J Biol Inorg Chem *26*, 715–726. 10.1007/s00775-021-01886-4.

272. Cowin, S.C., and Cardoso, L. (2015). Blood and interstitial flow in the hierarchical pore space architecture of bone tissue. Journal of Biomechanics *48*, 842–854. 10.1016/j.jbiomech.2014.12.013.

273. Kiesel, J., Miller, C., Abu-Amer, Y., and Aurora, R. (2007). Systems level analysis of osteoclastogenesis reveals intrinsic and extrinsic regulatory interactions. Dev. Dyn. *236*, 2181–2197. 10.1002/dvdy.21206.

274. Cackowski, F.C., Anderson, J.L., Patrene, K.D., Choksi, R.J., Shapiro, S.D., Windle, J.J., Blair, H.C., and Roodman, G.D. (2010). Osteoclasts are important for bone angiogenesis. Blood *115*, 140–149. 10.1182/blood-2009-08-237628.

275. Iezzi, G., Mangano, C., Barone, A., Tirone, F., Baggi, L., Tromba, G., Piattelli, A., and Giuliani, A. (2020). Jawbone remodeling: a conceptual study based on Synchrotron High-resolution Tomography. Sci Rep *10*, 3777. 10.1038/s41598-020-60718-8.

276. Qiu, S., Rao, D.S., Palnitkar, S., and Parfitt, A.M. (2002). Relationships between osteocyte density and bone formation rate in human cancellous bone. Bone *31*, 709–711. 10.1016/S8756-3282(02)00907-9.

277. Canè, V., Marotti, G., Volpi, G., Zaffe, D., Palazzini, S., Remaggi, F., and Muglia, M.A. (1982). Size and density of osteocyte lacunae in different regions of long bones. Calcif Tissue Int *34*, 558–563. 10.1007/BF02411304.

278. Vashishth, D., Gibson, G., Kimura, J., Schaffler, M.B., and Fyhrie, D.P. (2002). Determination of bone volume by osteocyte population. Anat. Rec. *267*, 292–295. 10.1002/ar.10114.

279. Dallas, S.L., and Bonewald, L.F. (2010). Dynamics of the transition from osteoblast to osteocyte: Dallas & Bonewald. Annals of the New York Academy of Sciences *1192*, 437–443. 10.1111/j.1749-6632.2009.05246.x.

280. Mullen, C.A., Haugh, M.G., Schaffler, M.B., Majeska, R.J., and McNamara, L.M. (2013). Osteocyte differentiation is regulated by extracellular matrix stiffness and intercellular separation. Journal of the Mechanical Behavior of Biomedical Materials *28*, 183–194. 10.1016/j.jmbbm.2013.06.013.

281. Liebi, M., Lutz-Bueno, V., Guizar-Sicairos, M., Schönbauer, B.M., Eichler, J., Martinelli, E., Löffler, J.F., Weinberg, A., Lichtenegger, H., and Grünewald, T.A. (2021). 3D nanoscale analysis of bone healing around degrading Mg implants evaluated by X-ray scattering tensor tomography. Acta Biomaterialia *134*, 804–817. 10.1016/j.actbio.2021.07.060.

282. Sarve, H., Lindblad, J., Borgefors, G., and Johansson, C.B. (2011). Extracting 3D information on bone remodeling in the proximity of titanium implants in SRμCT image volumes. Computer Methods and Programs in Biomedicine *102*, 25–34. 10.1016/j.cmpb.2010.12.011.

283. Hemmatian, H., Laurent, M.R., Ghazanfari, S., Vanderschueren, D., Bakker, A.D., Klein-Nulend, J., and van Lenthe, G.H. (2017). Accuracy and reproducibility of mouse cortical bone microporosity as quantified by desktop microcomputed tomography. PLoS ONE *12*, e0182996. 10.1371/journal.pone.0182996.

284. Jones, S.J., Boyde, A., and Pawley, J.B. (1975). Osteoblasts and collagen orientation. Cell Tissue Res. *159*. 10.1007/BF00231996.

285. Bacabac, R.G., Mizuno, D., Schmidt, C.F., MacKintosh, F.C., Van Loon, J.J.W.A., Klein-Nulend, J., and Smit, T.H. (2008). Round versus flat: Bone cell morphology, elasticity, and mechanosensing. Journal of Biomechanics *41*, 1590–1598. 10.1016/j.jbiomech.2008.01.031.

286. Kerschnitzki, M., Wagermaier, W., Roschger, P., Seto, J., Shahar, R., Duda, G.N., Mundlos, S., and Fratzl, P. (2011). The organization of the osteocyte network mirrors the extracellular matrix orientation in bone. Journal of Structural Biology *173*, 303–311. 10.1016/j.jsb.2010.11.014.

287. Wittig, N.K., Laugesen, M., Birkbak, M.E., Bach-Gansmo, F.L., Pacureanu, A., Bruns, S., Wendelboe, M.H., Brüel, A., Sørensen, H.O., Thomsen, J.S., et al. (2019). Canalicular Junctions in the Osteocyte Lacuno-Canalicular Network of Cortical Bone. ACS Nano *13*, 6421–6430. 10.1021/acsnano.8b08478.

288. Dunstan, C.R., Somers, N.M., and Evans, R.A. (1993). Osteocyte death and hip fracture. Calcif Tissue Int *53*, S113–S117. 10.1007/BF01673417.

289. Akhter, M.P., Kimmel, D.B., Lappe, J.M., and Recker, R.R. (2017). Effect of Macroanatomic Bone Type and Estrogen Loss on Osteocyte Lacunar Properties in Healthy Adult Women. Calcif Tissue Int *100*, 619–630. 10.1007/s00223-017-0247-6.

290. Walker, J., Shadanbaz, S., Kirkland, N.T., Stace, E., Woodfield, T., Staiger, M.P., and Dias, G.J. (2012). Magnesium alloys: Predicting in vivo corrosion with in vitro immersion testing. J. Biomed. Mater. Res. *100B*, 1134–1141. 10.1002/jbm.b.32680.

291. Liu, Y., Liu, D., You, C., and Chen, M. (2015). Effects of grain size on the corrosion resistance of pure magnesium by cooling rate-controlled solidification. Front. Mater. Sci. *9*, 247–253. 10.1007/s11706-015-0299-3.

292. Plaass, C., Von Falck, C., Ettinger, S., Sonnow, L., Calderone, F., Weizbauer, A., Reifenrath, J., Claassen, L., Waizy, H., Daniilidis, K., et al. (2018). Bioabsorbable magnesium versus standard titanium compression screws for fixation of distal metatarsal osteotomies – 3 year results of a randomized clinical trial. Journal of Orthopaedic Science *23*, 321–327. 10.1016/j.jos.2017.11.005.

293. Rendenbach, C., Fischer, H., Kopp, A., Schmidt-Bleek, K., Kreiker, H., Stumpp, S., Thiele, M., Duda, G., Hanken, H., Beck-Broichsitter, B., et al. (2021). Improved in vivo osseointegration and degradation behavior of PEO surface-modified WE43 magnesium plates and screws after 6 and 12 months. Materials Science and Engineering: C *129*, 112380. 10.1016/j.msec.2021.112380.

294. Bruns, S., Krüger, D., Galli, S., Wieland, D.C.F., Hammel, J.U., Beckmann, F., Wennerberg, A., Willumeit-Römer, R., Zeller-Plumhoff, B., and Moosmann, J. (2023). On the material dependency of peri-implant morphology and stability in healing bone. Bioactive Materials *28*, 155–166. 10.1016/j.bioactmat.2023.05.006.

295. Ancuţa, D.L., Coman, C., Alexandru, D.M., and Crivineanu, M. (2020). Animal Models Used in Testing the Biocompatibility of the Dental Implant – A Review. BUASVMCN-VM *77*, 1. 10.15835/buasvmcn-vm:2020.0020.

296. AO Research Institute, AO Foundation, Clavadelerstrasse 8, Davos, Switzerland, Pearce, A., Richards, R., Milz, S., Schneider, E., and Pearce, S. (2007). Animal models for implant biomaterial research in bone: A review. eCM *13*, 1–10. 10.22203/eCM.v013a01.

297. Jowsey, Jenifer (1996). Studies of Haversian systems in man and some animals. Journal of Anatomy *100*, 857–864.